



HAL
open science

Assistance to laparoscopic surgery through comanipulation

Lin Dong

► **To cite this version:**

Lin Dong. Assistance to laparoscopic surgery through comanipulation. Automatic. Université Pierre et Marie Curie - Paris VI, 2017. English. NNT : 2017PA066305 . tel-01721464

HAL Id: tel-01721464

<https://theses.hal.science/tel-01721464>

Submitted on 2 Mar 2018

HAL is a multi-disciplinary open access archive for the deposit and dissemination of scientific research documents, whether they are published or not. The documents may come from teaching and research institutions in France or abroad, or from public or private research centers.

L'archive ouverte pluridisciplinaire **HAL**, est destinée au dépôt et à la diffusion de documents scientifiques de niveau recherche, publiés ou non, émanant des établissements d'enseignement et de recherche français ou étrangers, des laboratoires publics ou privés.

UNIVERSITÉ PIERRE & MARIE CURIE

INSTITUT DES SYSTÈMES INTELLIGENTS ET DE
ROBOTIQUE

École Doctorale Sciences Mécanique, Acoustique, Électronique et Robotique de Paris

Spécialité: Robotique

THÈSE DE DOCTORAT

présentée par

Lin Dong

Assistance to laparoscopic surgery through comanipulation

Paris, December 2017

JURY

Rapporteur	BAYLE Bernard	Professeur, Université de Strasbourg
Rapporteur	POIGNET Philippe	Professeur, Université Montpellier
Examineur	PADOIS Vincent	Maître de Conférences, Université Pierre & Marie Curie
Directeur de thèse	MOREL Guillaume	Professeur, Université Pierre & Marie Curie



A dissertation submitted in fulfilment
of the requirements for the degree of
Doctor of Philosophy
(Robotics Engineering)
in Université Pierre et Marie Curie - Sorbonne Universités
ISIR - Institut des Systèmes Intelligents et de Robotique
École doctorale Sciences Mécaniques, Acoustique, Électronique & Robotique

lin.dong.upmc@gmail.com

To my dearest parents and myself.

Declaration

I, Lin Dong, hereby declare that except where specific reference is made to the work of others, the contents of this dissertation entitled "Assistance to laparoscopic surgery through comanipulation" are original and have not been submitted in whole or in part for consideration for any other degree or qualification in this, or any other University. This dissertation is the result of my own work and has not been written for me, in whole or in part, by any other person.

Lin Dong
December 2017

Acknowledgements

Firstly, I would like to express my sincere gratitude to my advisor Prof. Guillaume Morel for the continuous support of my Ph.D study and related research, for his patience, motivation, and immense knowledge. His guidance helped me in all the time of research and writing of this thesis. I could not have imagined having a better advisor for my Ph.D study.

Besides my advisor, I would like to thank the rest of my thesis committee: Prof. Bernard BAYLE , Prof. Philippe POIGNET, and Dr. Vincent PADOIS, for their insightful comments, encouragement, also for the hard questions which incited me to widen my research from various perspectives.

My sincere thanks also goes to all my experiment participants for their participation which supported my work.

I would like to thank my fellow labmates in ISIR Agathe team and the engineers working in the team for their cooperation, stimulating discussions, and for all the fun we have had in the last three years. In particular, I am grateful to my colleges who have greatly consoled me and helped me get out of the tough period: Sheng, Manelle, Tomasso, David, Florian, Rémi, Mario, Xavier, Caspar, Wenhao, Wenqian and Fériel.

Last but not the least, I would like to thank my family: my parents Huaguo Dong and Na Lin, for supporting me spiritually throughout writing this thesis and my life in general.

Résumé

La chirurgie laparoscopique conventionnelle apporte d'excellents avantages aux patients, mais pose de nombreux défis aux chirurgiens. L'introduction de robots dans les procédures chirurgicales permet de surmonter certaines des difficultés. Dans ce travail, nous utilisons le concept de comanipulation, où un bras robotique à 7 articulations en série sert de comanipulateur et génère des champs de force pour aider les chirurgiens.

Pour implémenter des fonctions telles que la compensation de la gravité de l'instrument ou le filtrage du tremblement de la main, il est utile de connaître la position du trocart en temps réel par rapport à la base du robot. Au lieu d'obtenir les informations du trocart à partir de l'étape de recalage, nous proposons dans ce travail un algorithme robuste de détection et de localisation de trocarts, basé sur la méthode du moins carré. Des expériences *in vitro* et *in vivo* valident son efficacité.

En tenant compte des caractéristiques de la chirurgie laparoscopique, *i.e.*, de l'espace de travail relativement grand et de la difficulté de planifier géométriquement le geste, des champs visqueux sont utilisés. Afin de mieux s'adapter aux mouvements différents, nous utilisons une loi de commande de viscosité variable. Cependant, cette loi de commande rencontre un problème d'instabilité, qui est analysé à la fois théoriquement et expérimentalement. Une solution d'ajout d'un filtre passe-bas de premier ordre est proposée pour ralentir la variation du coefficient de viscosité variable, dont l'efficacité est mise en évidence par une simple expérience de ciblage point à point.

Avec la position du trocart en temps réel connue, nous pouvons établir «le modèle de levier», une formule décrivant la relation entre les vitesses et les forces appliquées à différents points de l'instrument. Ceci permet de mettre en œuvre une loi de commande de viscosité sans utiliser de signaux bruités, aux points potentiellement intéressants, c'est-à-dire, le centre de la poignée ou la pointe de l'instrument. Une autre expérience de mouvement point à point est également menée pour comparer les caractéristiques de l'influence de la loi de commande sur les comportements de mouvement humain.

Mots clés: Robotique Comanipulée, Chirurgie Laparoscopique, Loi de Commande de la Viscosité, Effet Fulcrum, Enregistrement de trocar.

Abstract

Traditional laparoscopic surgery brings great advantages to patients but poses many challenges to surgeons. The introduction of robots into surgical procedures overcomes some of the difficulties. In this work, we use the concept of comanipulation, where a 7-joint serial robotic arm serves as a comanipulator and generates different force fields to assist surgeons.

In order to implement functions like instrument gravity compensation or hand tremor filtering, identifying real-time trocar position with respect to the robot base is a prerequisite. Instead of obtaining the trocar information from the registration step, we propose in this work a robust trocar detection and localization algorithm based on the least square method. Both in-vitro and in-vivo experiments validate its efficiency.

Taking into consideration the characteristics of laparoscopic surgery, *i.e.*, relatively large workspace and flexible operating objects, viscous fields are employed. In order to better adapt to different motion level, we use a variable viscosity controller. However, this controller encounters an instability problem, which is analyzed both theoretically and experimentally. A solution of adding a first order low pass filter is proposed to slow down the variation of the variable viscosity coefficient, whose efficiency is evidenced by a simple point-to-point targeting experiment.

With the real-time trocar position known, the “lever model”, a formula describing the relationship of the velocities and forces of different instrument points, can be established. This allows the possibility of implementing viscosity controller without using noisy signals at the potentially interesting points, namely, the centers of the instrument handle and tip. Another point-to-point movement experiment is further conducted to compare the features of the controller influence on human motion behaviors.

Keywords: Comanipulated Robotics, Laparoscopic Surgery, Viscosity Control, Fulcrum Effect, Trocar Registration.

Table of contents

List of figures	xix
List of tables	xxi
1 Introduction	3
1.1 Laparoscopic surgery	3
1.2 Robot-assisted surgery	4
1.2.1 Telemanipulation	4
1.2.2 Comanipulation	5
1.3 The Achilles surgical system	6
1.4 Questions to be solved	7
1.5 Objective of the thesis	10
1.5.1 Instrument gravity compensation	10
1.5.2 Detecting trocars	10
1.5.3 Smooth guidance of motion - variable viscosity control	12
1.5.4 Lever effect	13
1.6 Content of the work	14
2 A laparoscopic comanipulator	17
2.1 Introduction	17
2.2 Achilles' characteristics	17
2.2.1 Mechanics	17
2.2.2 Kinematics	19
2.2.3 Actuation	23
2.2.4 General idea of the comanipulated system	24
2.3 Gravity compensation for laparoscopic instrument	26
2.3.1 Implementation	26
2.3.2 Evaluation	29

2.4	Robust trocar detection and localization	31
2.4.1	Specific aims	31
2.4.2	Least square algorithm	33
2.4.3	Trocar detection and localization	34
2.4.4	Experimental validation	39
2.5	Conclusions	46
3	Variable viscosity control	47
3.1	Introduction	47
3.2	Variable viscosity control	47
3.2.1	Basic control law	47
3.2.2	Theoretical analysis of instability	49
3.2.3	Experimental evidence of instability	51
3.3	Adding a dynamics to slow down viscosity variation	55
3.3.1	Viscosity control with filtered coefficient	55
3.3.2	Theoretical investigation of stability	56
3.3.3	Experimental evaluation of stability	58
3.4	Point-to-point experiment	60
3.4.1	Materials and methods	60
3.4.2	Experimental results	65
3.4.3	Discussion	70
3.5	Conclusions	71
4	Lever model effect	73
4.1	Introduction	73
4.2	Establishment of lever model	73
4.2.1	Kinematic part	74
4.2.2	Dynamic part	76
4.2.3	The computation of lever model matrix	77
4.2.4	Verification of lever model	78
4.2.5	Discussion about lever model	79
4.3	Viscosity control with lever model	80
4.4	Materials and methods	81
4.4.1	Experiment setup	81
4.4.2	Experiment protocol	83
4.4.3	Performance indicators	85
4.4.4	Data analysis	86

4.5	Experimental results	87
4.6	Discussion	92
4.7	Conclusions	94
5	Conclusions and perspectives	95
5.1	Conclusions	95
5.2	Perspectives	96
	References	99
	Appendix A Questionnaire of the point-to-point experiment for lever model effect	107

List of figures

1.1	Traditional laparoscopic surgery scene	4
1.2	Illustration of laparoscopic surgery with concept of comanipulation	8
2.1	The sketch of the comanipulator Achilles	18
2.2	The comparison of joint noise level of Achilles	19
2.3	Achilles' kinematics	20
2.4	Norms of positions of point P and T	21
2.5	Norms of the unfiltered and filtered velocities at point P	23
2.6	Illustration of the comanipulated system	25
2.7	Illustration of gravity compensation	26
2.8	A typical instrument configuration for gravity compensation experiment	30
2.9	The experimental results for instrument gravity compensation	31
2.10	Principle of trocar detection.	32
2.11	Projection of F into the instrument axis	33
2.12	Trocar detection and localization experiment setup	39
2.13	Central positions of all trocars in 3D view for the lab experiments	41
2.14	Experimentally obtained trocar positions in 3D view after transformation for the lab experiments.	42
2.15	Central positions of all trocars in 3D view after transformation for the lab experiments.	43
2.16	Pig experiment scenario	44
2.17	Experimentally obtained trocar positions and centroids before transformation for the pig experiments.	45
2.18	Trocar positions and centroids after transformation for the pig experiments.	45
3.1	Variation of the viscosity coefficient with respect to the norm of the velocity	48
3.2	Variation of the norm of the resistive force with respect to the norm of the velocity	49

3.3	Illustration of theoretical analysis of instability	50
3.4	A scene of the controller stability experiment	52
3.5	Gauge providing a visual feedback to the user of the current velocity	53
3.6	Three designs of $\lambda(\ \mathbf{v}\)$ used for the experiments	53
3.7	Experimentally observed velocity for a given subject under Conditions $C_1 - C_3$	54
3.8	Errors averaged across ten subjects under Conditions $C_1 - C_3$	55
3.9	Experimentally observed velocity for a given subject under conditions $C_4 - C_7$	59
3.10	Errors averaged across ten subjects under Conditions $C_1 - C_7$	59
3.11	The point-to-point movement experimental setup	61
3.12	Illustration of correction time	64
3.13	A typical velocity profile of trajectory AB under controllers 1-5	65
3.14	A typical velocity profile of trajectory BD under controllers 1-5.	66
3.15	Mean values and SEM of peak velocity of 28 subjects	66
3.16	Mean values and SEM of total task time of 28 subjects	67
3.17	Graph showing mean values of correction time ratio of 28 subjects	67
3.18	Mean values and SEM of trajectory curvature of 28 subjects	68
3.19	Mean values and SEM of jerk metrics of 28 subjects	68
3.20	Mean values and SEM of energy of 28 subjects	69
4.1	Illustration of lever model	74
4.2	Comparison of noise level of the instrument tip velocity with and without using trocar information	78
4.3	Experimental setup	82
4.4	Three sessions of different insertion depths	84
4.5	Synchronization illustration	86
4.6	Graph showing mean values of jerk of 17 subjects	87
4.7	Mean values and SEM of trajectory curvature of 17 subjects	88
4.8	Mean values and SEM of peak velocity of 17 subjects	88
4.9	Mean values and SEM of total task time of 17 subjects	89
4.10	Mean values and SEM of energy of 17 subjects	89
4.11	Mean values and SEM of correction time ratio of 17 subjects	90
4.12	Mean values and SEM of synchronization of 17 subjects	90

List of tables

2.1	Denavit-Hartenberg parameters of Achilles	21
2.2	Experimental results for instrument gravity compensation	30
2.3	Experimental results of robustness verification for trocar detection	40
2.4	Experimental results of rapidness verification for trocar detection	40
2.5	Distances between trocar centroids in the lab experiments	42
2.6	Distances and angles between trocar centroids in the animal experiment	44
3.1	The seven conditions for controller stability experiment	58
3.2	The five controllers for point-to-point movement experiment	63
A.1	Deep Insertion	107
A.2	Middle Insertion	108
A.3	Small Insertion	108

Notations

In this work, we will use the following notations:

- for scalars: lowercase italics, a .
- for vectors, without projection of the components into a particular base: lowercase bold, \mathbf{a} .
- for 3D points: uppercase italics, A .
- for frames: $\mathcal{F}_A = (O_A, (\mathbf{x}_A, \mathbf{y}_A, \mathbf{z}_A))$.
- for vectors, with projection of the components into a particular base $(\mathbf{x}_A, \mathbf{y}_A, \mathbf{z}_A)$: lowercase bold and left superscript uppercase, ${}^A\mathbf{a}$.
- for the coordinates of a point M in a frame \mathcal{F}_A : ${}^A\mathbf{p}_M$.
- for a vector joining A to B : \mathbf{d}_{AB} .
- for a rotation matrix from base $(\mathbf{x}_A, \mathbf{y}_A, \mathbf{z}_A)$ to base $(\mathbf{x}_B, \mathbf{y}_B, \mathbf{z}_B)$: $\mathbf{R}_{A \rightarrow B}$.
- for a homogeneous transform from \mathcal{F}_A to \mathcal{F}_B :

$$\mathbf{T}_{A \rightarrow B} = \begin{pmatrix} \mathbf{R}_{A \rightarrow B} & {}^A\mathbf{d}_{O_A O_B} \\ 0 & 0 & 0 & 1 \end{pmatrix}.$$

- for the velocity of a point A with respect to a frame \mathcal{F}_B : $\mathbf{v}_{A/\mathcal{F}_B}$. For convenience, when the observation frame is \mathcal{F}_0 , it is omitted (default value). In other words, \mathbf{v}_A is by convention identical to $\mathbf{v}_{A/\mathcal{F}_0}$.
- for the rotation velocity of a frame \mathcal{F}_A with respect to a frame \mathcal{F}_B : $\boldsymbol{\omega}_{A/B}$. For convenience, when the observation frame is \mathcal{F}_0 , it is omitted (default value). In other words, $\boldsymbol{\omega}_A$ is by convention identical to $\boldsymbol{\omega}_{A/0}$.

- for a twist describing the velocity of frame \mathcal{F}_A with respect to a frame \mathcal{F}_B at a point C which is attached to frame \mathcal{F}_A :

$$\{\mathcal{T}_{A/B}\}_C = \left\{ \begin{array}{c} \mathbf{v}_{C/B} \\ \boldsymbol{\omega}_{A/B} \end{array} \right\}.$$

- for a wrench at point A :

$$\{\mathcal{W}\}_A = \left\{ \begin{array}{c} \mathbf{f} \\ \mathbf{m}_A \end{array} \right\},$$

where \mathbf{f} is a force and \mathbf{m}_A a moment at point A .

- for the x component of a vector \mathbf{v}_F : $\mathbf{v}_{F,x}$.

Chapter 1

Introduction

1.1 Laparoscopic surgery

Laparoscopic surgery, a specific type of “minimally invasive surgery” (MIS), is considered as one of the biggest success in the modern surgery history [1]. In this procedure, instead of a single large incision needed in the traditional open surgery, generally 3-5 small incisions of around ten millimeters are made. Small cannulas called trocars are then installed on the patient through which surgical instruments and a laparoscope are inserted into the abdomen. The abdominal cavity is inflated by carbon dioxide gas so as to open a workspace for operation. The surgeon maneuvers elongated straight instruments outside of the abdomen by watching magnified surgical site displayed on a screen provided by a laparoscopic video camera. Fig. 1.1 presents a typical laparoscopic surgery scene.

Compared with conventional open surgery, laparoscopic surgery has many benefits such as less collateral damages to healthy tissue, decreased post-operative pain, lower risk of infection, shorter hospital stay, faster recovery, better cosmesis, etc. [2, 3]. However, the advantages are mainly for patients. As to surgeons, this technique induces substantial difficulties and prominent limitations. For example, the presence of trocars causes kinematic restrictions and the lever effect [4–6]. The fact that the operating site displayed on a video monitor is not spatially aligned with the surgeon’s hand compromises the visuo-motor coordination [7]. Besides, the laparoscopic procedure results in poor ergonomics for surgeons, leading to fatigue and physiologic tremor [8].

These difficulties largely limit the spread of laparoscopic surgery. The advent of robot-assisted surgery brings the possibilities to eliminate more of these impediments by enhancing the capabilities of surgeons. Taking the best both from robots and from humans, surgical robots are considered to be able to extend human sensations. Some even suggested that



Fig. 1.1 Traditional laparoscopic surgery scene.

laparoscopic surgery is a “transitional” technology leading to robotic surgery in the history of surgical evolution [9–11].

1.2 Robot-assisted surgery

Robot-assisted surgery, also known as robotic surgery, requires the use of a surgical robot to aid in surgical procedures. A surgical robot is a computerized system with motorized mechanism (one or more surgical arms) capable of interacting with the environment, *i.e.*, the surgical site.

1.2.1 Telemanipulation

The most widely accepted commercialized robotic system is the da Vinci surgical system (Intuitive Surgical, Mountain View, CA, USA) [12]. It is a telemanipulated device placed between the surgeon and the patient which converts physical motion into electrical signals [13]. Through the comprehensive master-slave mechanism, the surgeon can operate remotely from a master console physically separated from the patient. Other surgical systems using the concept of telemanipulation include the AESOP robot (Computer Motion, Santa Barbara, CA, USA), a voice-activated robotic arm that functions as an endoscopic camera holder and the ZEUS system (Computer Motion, Santa Barbara, CA, USA), which, similarly to the da

Vinci system, is also a master-slave robotic surgical system. ZEUS system was discontinued in 2003, following the merger of Computer Motion with its rival Intuitive Surgical [14].

The introduction of telemanipulated surgical robots overcomes many obstacles existing in laparoscopic surgery [15–17]. Preserving most of the benefits for patients in conventional laparoscopic surgery, the improvements that telemanipulated robotic systems have brought to surgeons are obvious, namely: by translating the surgeon's hand motions into identical instrument motions, the system is able to avoid the reverse-fulcrum-induced movements, to filter out hand tremors as well as to increase dexterity. The surgeon can intuitively manipulate the instruments with a proper visuo-motor coordination and improved visualization. Moreover, better postural comfort is achieved thanks to the ergonomically designed control console. Even though the use of the telemanipulation greatly enhances the surgeons' performance, at the same time, it has raised new problems [18]. Telemanipulated electromechanical systems have large footprint, not easy to fit into the current operating theater. The installation and calibration procedures are fastidious and time-consuming. Lack of communication is another drawback since the surgeon operating on the master console is isolated from the patient. The high price tag, of course, limits the widespread use of telemanipulated systems within most healthcare organizations and points to inadequate training for certification requirements [19].

1.2.2 Comanipulation

Apart from the telemanipulated robots, there exists another different concept: comanipulation. It is a paradigm involving a robot and a user simultaneously manipulating a load or a tool, [20, 21]. Instead of functioning as the interface between the surgeon and the patient in teleoperation, the robot is employed as a comanipulated device, in the sense that the gesture control of the instrument is shared by the robot and the surgeon.

The currently existing commercialized comanipulated robotic systems are basically designed for specific types of surgical tasks. Acrobot (The Acrobot Company, Ltd., London, UK) is a semi-active hands-on orthopedic robotic system for total knee replacement (TKR) surgery, which allows the surgeon to safely cut the knee bones to fit a TKR prosthesis with high precision [22]. MAKOpasty (Stryker Corp, Kalamazoo, MI, USA) is a surgical robot proposed for unicompartmental knee arthroplasty (UKA) [23]. The semi-active robotic arm controlled by the surgeon can ensure implantation within acceptable limits of target specification. Robotized Surgical Assistant (ROSA, MedTech, Montpellier, France) is a robot based navigation system used for planning and implantation guidance in stereotactic placement of intracranial depth electrodes in neurosurgery [24, 25].

Apart from the commercialized systems, a number of research institutes have also exploited the idea for precise surgical tasks. Johns Hopkins University implemented the

Steady Hand microsurgical robot, a specially designed cooperatively controlled robot arm for microsurgical manipulation [26]. Micron system is a hand-held actively stabilized comanipulator developed at Carnegie Mellon University [27], able to increase accuracy during eye microsurgical procedures by removing involuntary motion. Researchers in University of Paris 6 designed a compact robot named MC^2E for minimally invasive surgery (MIS), which can measure the distal organ-instrument interaction with a sensor placed outside the patient [28]. A Robotic manipulator was developed in University of Leuven to assist vitreoretinal surgeons in the procedure of retinal vein cannulation [29]. This device features a new Remote Center of Motion mechanism and specially suits for highly confined working space around a fixed incision point.

Some preliminary experiments with comanipulated surgical robots showed that this control form is natural and convenient for surgeons. Indeed, the comanipulation reserves the superb manual dexterity, rapid learning ability, great adaptation skills of human operators, and the same time, it combines the benefits of the robot such as the capability to enhance manipulation precision and to perform repetitive tasks without getting tired. Therefore, comanipulation can be applied to tasks that require both precise manipulation and human judgment so as to enhance gesture quality [26]. Comanipulation outperforms telemanipulation in the aspects of easy installation, small volume, low expense and the ability to give surgeons control sensation, even though the ergonomic comfort it offers is not comparable to the telemanipulation.

1.3 The Achilles surgical system

Nowadays, comanipulated surgical systems are principally used for high precision surgeries such as microsurgery and bone surgery. For microsurgery with a highly confined space, *i.e.*, eye surgery, high damping is generated by comanipulators to help slow down the intended movements, maintain a stable instrument position and attenuate the surgeon's hand tremor. For orthopedic surgery such as hip and knee surgery, predefined boundaries are usually used as geometrical guidance so that the comanipulated robots could provide motion constraint to improve surgical accuracy.

In this work, we aim at using the concept of comanipulation in the field of laparoscopic surgery. Compared with the current existing telemanipulated setups such as the da Vinci system, this system might offer the following benefits:

- **High modularity.** The whole system is highly modularized. Standard surgical instruments are able to be integrated into the system effortlessly.

- **Easy installation and deinstallation.** Since the robot is compact, the procedures of installation, deinstallation and integration into the application environment are easy to implement. Fastidious registration and reconfiguration of the device before or during the procedure are not required, thus shortening the operation time. In case of system failure, the surgeon can immediately change to conventional laparoscopic surgery and continue the operation.
- **Better technique transferability.** It does not create many troubles for surgeons to learn the robot-assisted laparoscopic surgery as long as they have mastered the conventional surgeries. Therefore, skill transferability problems are prevented [30].
- **Better control sensation.** Since the comanipulated system requires the surgeon standing beside the patient, he or she has the feeling of being involved in the surgical control loop, which is naturally preferable. Furthermore, even though the robot can provide force on the instrument, it does not totally deprive the surgeon of the feeling of force feedback, making the operation much more reliable.
- **Low expense.** The cost of the comanipulated system is potentially more affordable thanks to its cheaper implementations.

A robot-comanipulated laparoscopic surgery is similar to the conventional one. During the operation, surgeons stand beside of the patient bed and maneuver the instruments. Being controlled by commands from the computer system, the robot can apply forces to the instrument so as to provide guidance to surgeon's gestures. Fig. 1.2 is a simplified illustration of the scene of a comanipulated laparoscopic surgery. The two blue devices holding surgical instruments represent comanipulators, which we name as "Achilles". This work mainly focuses on the research of the control of Achilles.

1.4 Questions to be solved

Lack of geometrical guidance

In a comanipulative task where the human and the robot have physical interaction, impedance control is a classical framework to use. Virtual fixtures is a common approach for motion guidance, widely used in comanipulated surgeries [2, 31–33]. The robot actively provides stiffness on the guided mechanism to limit movement into restricted region and/or guide motion along desired paths or surfaces in the workspace so that safer and faster operation can be achieved [34]. The implementation of virtual fixtures is based on a kinematic or

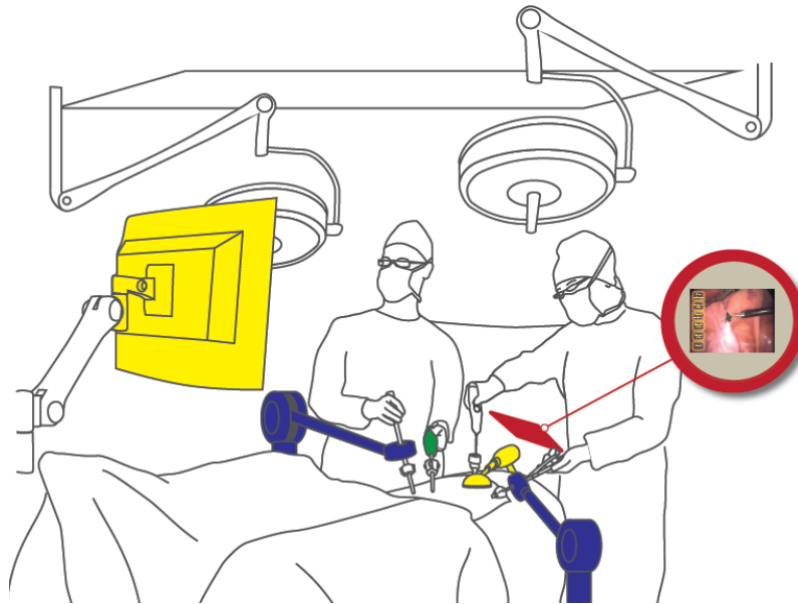


Fig. 1.2 Illustration of laparoscopic surgery with concept of comanipulation.

dynamic analysis of the manipulated task, for which a precise model needs to be established. Laparoscopic surgery, unlike bone surgery, deals with soft and flexible tissues which move and deform easily during surgical procedures. Breath also leads to the motion of the organs, which forces the surgeon to aim at a dynamic target. This constant movement makes the specific geometrical and physical representation of tasks quite complex, even impossible. Therefore, although virtual fixtures is widely employed in comanipulation, for laparoscopic procedures it is not practical to apply elastic force fields (stiffness). In this work, we shift to the viscous fields, which can provide damping for the intervention of instrument dynamics [35].

Large range of motion

Literature shows that viscous force has a good performance on maintaining motions stable and precise in microsurgery [26, 27, 36]. The workspace for operating microsurgery, however, generally requires a very limited area where large motions are not allowed. Examples includes eye surgery, ear, nose and throat (ENT) surgery, dental surgery, neurosurgery, etc [37]. Slow and yet stable, accurate motions are preferred in this situation for the reason of safety. Relatively large viscous damping is thus required for higher motion resistance [38]. In laparoscopic surgery, however, the operating workspace is much larger and the range of motion varies. For precise procedures such as cutting and suturing, the principle necessity is to ensure safety and precision, thus, slow but accurate motions are necessary. On the

other hand, for tasks with a relatively long distance to cover, *e.g.*, moving the instrument tip from one position to another, high damping slows down the intended movements, leading to fatigue and more operative time consumption. Therefore, where there is no special precision requirement, large motions without external resistance are preferred. To summarize, in order to provide a level of assistance adapted to variable operating conditions (high movability or high stability), a comanipulator should be able to modify its impedance during manipulation tasks.

In this work, we propose to utilize a variable viscosity to satisfy both requirements of instrument motions, which is supposed to have the following effect: when the instrument velocity is low, the robot generates large viscous force to slow down the motion so as to stabilize the hand movement. When the instrument moves fast, no force or small force is exerted in such a way that the surgeon could manipulate the instrument easily.

Lever effect

A typical laparoscopic instrument is a long shaft with its tip inserted into the abdomen and its handle held by the surgeon outside of the patient. The trocar and the instrument form a lever, with the entry point as its fulcrum. The motion of points lying on the instrument is under the constraint of a specific relationship, which is called the lever effect (or fulcrum effect). The movement of the instrument tip and that of the handle are inverted, and their amplitude ratio for the rotational motions depends on the insertion depth of the instrument into the trocar. This might contribute to the amplification of the involuntary physical hand tremor, which would decrease surgeons' performance, more likely to result in the increased rate of operative injuries as compared with open surgery [5]. Besides, viscosity control implemented at a certain point will lead to anisotropy for the other points on the instrument.

The position of the robot force physically imposed on the instrument, namely the connection point where the robot holds the instrument, is fixed. Equivalent virtual forces are generated in the instrument tip and handle, respectively, which can be computed thanks to a lever model [39]. The instrument tip directly contacts with the tissues or organs of the patient. Moreover, it influences the visual feedback information that the surgeon gains from the projected images. The handle, on the other hand, has an effect on the surgeon's sensorimotor control system. In other words, the virtual controller implementing position may lead to different performance in terms of motion guidance. An important question is hence worthwhile to ask: which is the preferred point for the implementation of the viscosity controller to bring a desired outcome? The study of this question constitutes an important topic.

1.5 Objective of the thesis

The general objective of the work is to employ Achilles as a comanipulator to provide guidance to different surgical gestures so as to enhance the performance of surgeons during laparoscopic surgery.

1.5.1 Instrument gravity compensation

In a laparoscopic procedure, the surgeon does the surgery by maneuvering different types of surgical instruments rigidly inserted into the patient's abdomen. The gravity of different instruments varies a lot. Traditional laparoscopic instruments include forceps, scissors, probes, dissectors, hooks, etc. [40]. Robotic articulated instruments are also designed and commercialized, such as JAI MY from Endocontrol and the VeSPA instruments from Intuitive Surgical Inc. Even though these motorized instruments provide more dexterity, they are much heavier (as heavy as half a kilogram) than the traditional ones due to the presence of motors and drive cables. This makes them energy-consuming to manipulate and easily leads to fatigue. More importantly, in the case of accidental instrument drop, the risk of unintentional deep insertion into the patient's abdomen largely increases, posing grave safety hazard of tissue or organ damage during surgery. Adding gravity compensation, for both motorized instruments and for traditional ones, is hence of importance to counterbalance the instrument weight in such a way that the surgeon does not feel resistance due to instrument gravity. Therefore, in this work, the first way to achieve the objective of comanipulation gesture guidance is to compensate instrument gravity so that the surgeon would not have to carry the instrument weight.

We could add a constant value in the opposite direction of instrument gravity, as done in [41]. However, in practice, the gravity torque changes with instrument positions and orientations. Namely, when the depth of instrument insertion into the abdomen changes, its gravity generates different torques at the entry point. The angle between the instrument axis and the abdomen plane also has an influence to the gravity torque. Therefore, in this work, we use a real-time method for gravity compensation, described in detail in Chapter. 2.

1.5.2 Detecting trocars

The existence of trocars creates a kinematic constraint which limits the surgical instrument motion to four dofs: three independent rotations around the insertion point and one translation along the instrument longitudinal axis. When a robot is used to manipulate instruments, it

is crucial to know the trocar position information with respect to the robot base body. The question of identifying this location has been the object of dense research in the past decades.

An option consists in using an external localizer. For example, in [42], a registration procedure consists, for the surgeon, in moving the endoscope around the fulcrum, while an external stereo camera pair watches the scene. The lines corresponding to the endoscope axis are extracted from several images and, thanks to a Hough transform, their intersection is computed to form a 3D trocar position estimation.

In order to avoid the use of external equipment, direct registration/installation of the robot is more often used. This is the case when using a robot exhibiting a Remote Center of Motion (RCM). Using such a mechanism requires a precise installation of the robot base body in the workspace prior to the operation, in such a way that its RCM precisely fits with patient's entry point in order to avoid tissue damage. An example is the da Vinci robot, which is made up of four interdependent arms mounted on a single base. Each of its arms has a RCM in order to respect the constraint formed by the trocar, [30]. The robot installation procedure requires a passive arm to position the base body of each active arm. A simpler option consists in directly placing the robot on the patient, as proposed in [43] (endoscope holder) or [44] (instrument holder). Here, there is no need for an extra passive arm to position the robot base as the holder is automatically centered on the trocar. However, for all the RCM-based solutions, in the event of robot relocation during the procedure, the realignment of the robot arms to trocars requires a complete new installation process.

If the robot is to be used at several trocar locations during the same operation, a preferable approach is to use a 6-dof robot without RCM to avoid re-installation. As a price for versatility, extra work is to be done in order to guarantee that the fulcrum constraint is respected. In [45], a fully actuated 6-dof robot equipped with a force sensor is proposed. The force sensor is used both to control the movements while minimizing forces at the trocar and to estimate the fulcrum location in real time.

Exploiting a force sensor raises concerns in terms of cost, robustness, and compatibility with operating room (OR) constraints. To avoid using such an equipment, the 6-dof robot can be partially actuated and equipped with two passive joints at the wrist. The instrument can thus naturally rotate around the fulcrum point while limiting forces exerted to that point, see *e.g.* [46]. The AESOP robot, used in [47], makes use of such joints. To compute the online trocar point position, joint position data is collected. An algorithm that computes the best intersection between instrument axes at successive locations is used. This method does not require precise positioning of the robot, thus the setup procedure is facilitated. However, the algorithm proposed in [47] is suboptimal as it uses an average filter of a series of two-point

estimates. Moreover, this solution is built on the assumption that i) the instrument is indeed inserted into a trocar; ii) the entry point does not move.

In the context of comanipulated endoscopic surgery these hypotheses do not hold: The problem is not only to localize the trocar but also to detect the trocar presence. An adapted mathematical approach, pertaining to Least Square (LS) optimization, is proposed in this work. Its practical implementation is based on rules for selecting appropriate data to feed the LS algorithm and criteria to robustly and rapidly detect the trocar presence. Chapter. 2 depicts the detailed work.

1.5.3 Smooth guidance of motion - variable viscosity control

Human hand tremor is an involuntary hand movement, which is approximately rhythmic and roughly sinusoidal [48]. These intrinsic limitations impede the manual positioning accuracy, even making many delicate surgical procedures impossible. The degradation of surgical performance due to noise is even greater for tasks with high level of difficulty, such as mesh alignment and suture tying [49]. The robot controller could provide smooth, tremor-free, precise positional control by sensing forces exerted by the operator on the tool. Research in the area of hand tremor suppression follows mainly two lines: teleoperated systems and cooperated system. Tremor filtering is dealt with the telerobotic technology in [50], where the motions of unstable human hands operating in the master subsystem are transferred into stable robotic arm movements. The authors in [51] designed an active hand-held microsurgical instrument named Micron for comanipulation, which implements tremor cancellation via the weighted-frequency Fourier linear combiner algorithm. In [26], an approach named steady-hand micromanipulation is developed, in which the tool is held simultaneously by the operator's hand and a specially designed actively controlled robot arm. In this work, we expose the small motions of the surgical instrument to resistive viscous fields to filter out the hand tremor. Outside the delicate, precision-required operations such as cutting, laparoscopic procedures include also movements with large speed, *i.e.*, transporting the instrument tip from one position to another. Damping at this stage are not desirable since it results in large force and consumes more energy whereas precision requirement is not strictly demanded. Therefore, viscosity coefficient is adjusted to be a small value in order to achieve comfortable displacement of the instrument. To conclude, the viscous controller is supposed to have the ability to adapt to different levels of motion range.

This approach of variable viscosity control was first proposed in [52] for assisting carrying objects. It is based on the experimental observation that the viscosity of a human operator's arm drops at high velocity when collaborating with an other human operator to carry a load along a linear path. From this observation, a robot controller is designed to

mimic this behavior: at low velocities, the viscosity is set high. When a velocity threshold is reached, a lower viscosity is programmed. As a result, human-robot comanipulation tasks are shown to exhibit trajectories that resemble those of human-human comanipulation tasks. However, this approach of abrupt change of viscosity results in degraded velocity control during point-to-point experiments conducted in [53]. This robot controller is then modified to be made “optimal” in [53], according to the authors. Namely, instead of abrupt changes, the viscosity coefficient follows an exponential function of time once the threshold has been reached. Resulting velocity profiles of collaborative human-robot point-to-point movements exhibit the typical bell shape of minimum jerk trajectories, which qualifies the collaborative movements as “natural”, [54]. The experimental results are appealing, however, unfortunately, this method can not be widely applied since the damping coefficient is the function of a limited time segment, not in real-time.

The variable viscosity approach was also used for more complex tasks. In a human-robot cooperative calligraphic task, [55], the viscosity coefficient is settled in proportion to the stiffness of the human operator’s arm, which is estimated in real-time. This approach requires an on-line estimator of the arm stiffness, which suffers from noise and robustness issues. In a robot assisted manual welding task, [56], the damping coefficient is a piecewise linear function of the norm of the robot velocity. The same method is employed in [57] for a task where the robot is manually guided to describe a square in the vertical plane. However, depending on the robot control parameters, this approach may lead to instability, due to the large force generated according to the linearly dropped damping coefficient.

In all these papers, the benefits of variable damping coefficient are clearly demonstrated. However, the influence of different variable viscosity coefficients on human’s hand motion profiles is not sufficiently analyzed. In the work, through theoretical analysis and practical experiments, we show that the viscosity coefficient drop creates an unstable dynamics and distorts the human natural motions. We thus introduce a second linear dynamics to slow down the viscosity coefficient variations. Namely, a first order low pass filter is used. This dynamics is experimentally shown able to stabilize the interaction and to restore the natural movements in Chapter. 3.

1.5.4 Lever effect

The lever effect poses the cognitive and perceptual difficulties to surgeons and is considered as the greatest ergonomic problem of the skill acquisition in laparoscopic surgery [58]. Many researchers have been focusing on the lever effect topic [4, 5, 58–61]. Some authors show interest in studying how the presence of the trocar affects the operators’ motor and cognitive sensations, such as the influence of the kinematic and dynamic transformations to

the learning [60], the test of distal-shift hypotheses of extending hand movement schema to tool movement characteristics [4, 62].

Other authors focus on developing robotic devices with different kinematic designs with the aim of aiding surgeons' manipulation through a fulcrum [39]. Some robots, such as the da Vinci surgical system, feature a remote center of motion (RCM), which serves as an invariant point fitting the fulcrum point so as to prevent damage to the patient's tissues. A four-DOF robot exhibiting RCM is also described in [63]. This specialized kinematic design requires the robot base carefully placed in the workspace prior to instrument manipulation. A second mechanism may even be necessary for precise positioning, leading to a large system footprint. Serial robots with six-DOF are also exploited. This kind of robots possesses no "in built" invariant point and thus allows placing the robot base independently from the entry point. In the case of fully actuated robots, the kinematic constraint, *i.e.*, the fulcrum point position, needs to be obtained in real time since this information is included in the robot's inverse kinematics. This can be solved either through the knowledge on the fulcrum location, as proposed in [64–66], or with an additional end-effector force sensor for its estimation, as done in [67]. In the situation of partially actuated robots, which is the case of Achilles, the two passive joints at the wrist frees the orientation of the instrument around the robot end-effector point. Such mechanism allows any motion of the robot end-effector point when the instrument is inserted into the trocar and rotates around the fulcrum point, thus respecting the kinematic constraint using only four actuators.

In this work, with the knowledge of the real-time trocar location known [68], the fulcrum effect is able to be expressed as lever model in the form of formulas. According to this model, the force physically applied at the robot wrist point could be computed to evaluate equivalent forces at any point of the instrument. The kinematic and dynamic features of Achilles make easy the implementation of viscosity force at the robot wrist point given that its velocity is precisely known and the robot force is directly exerted to the instrument at this point. Therefore, we have different options to apply viscosity control developed in Chapter. 3, mainly the handle point and the tip point of the instrument.

1.6 Content of the work

The coming chapters are organized in the following way: Chapter 2 describes Achilles' physical characteristics, its kinematics and dynamics, based on which a real-time gravity compensation for the laparoscopic instrument is implemented. Since the gravity compensation relies on the insertion depth of the instrument, it is essential to know in real time the trocar position. The algorithm of a robust real-time trocar detection and localization is also

presented in Chapter 2. Chapter 3 describes and resolves the instability problem of variable viscosity control through theoretical analysis as well as practical experiment, followed by a simple human-robot point-to-point movement experiment to verify the efficiency of the solution. In Chapter 4, the proposed lever model extends the possibility of adding viscosity control at not only the robot wrist point, but also at the hand and the tip of the instrument. The designed experiment aims to compare the characteristics of different controller positions. Finally, Chapter 5 summarizes the whole thesis work and presents some perspectives on the future work.

Chapter 2

A laparoscopic comanipulator

2.1 Introduction

In many comanipulation applications, the robotic devices are specially designed robotized arms. Here in this work, we also employ a serial robotic arm to serve as a laparoscopic comanipulator for the advantage of small footprint and flexible workspace. Its characteristics are detailed from the aspects of mechanics, kinematics and dynamics.

In order to further exploit the possibilities that the robot could bring, some fundamental functions are developed in this chapter. First of all, a function named instrument gravity compensation is described and experimentally verified. It is used to improve surgeons' ergonomics by relieving them of the fatigue of holding a heavy instrument. The real-time trocar position expressed in the robot base frame is another essential information, based on which advanced functionalities could be implemented. A robust real-time trocar detection and localization algorithm using least square method is presented.

2.2 Achilles' characteristics

2.2.1 Mechanics

The comanipulator Achilles is a robotic arm designed at ISIR on a technological basis from Haption. It is composed of seven pivot joints serially assembled according to a conventional anthropomorphic geometry, depicted in Fig. 2.1. The first three are active joints driven by electric motors and they form the shoulder and the elbow. The last four joints are passive, with no motors. Joint 4 is an indexed joint able to adjust robot configuration to suit the actual workspace constraints. Its value is determined at the initial setup stage and kept constant unless the configuration changes. Joints 5, 6 and 7 constitute a spherical wrist,

whose rotational axes together with the instrument axis, intersect at point P , illustrated as a red dot in Fig. 2.1, which is hence called wrist center. This mechanism, similar to the structure of AESOP robotic arm, allows the instrument to naturally rotate around the insertion point while guaranteeing that no forces are exerted to the abdomen. Thanks to a magnet, the instrument can be detached from the robot.

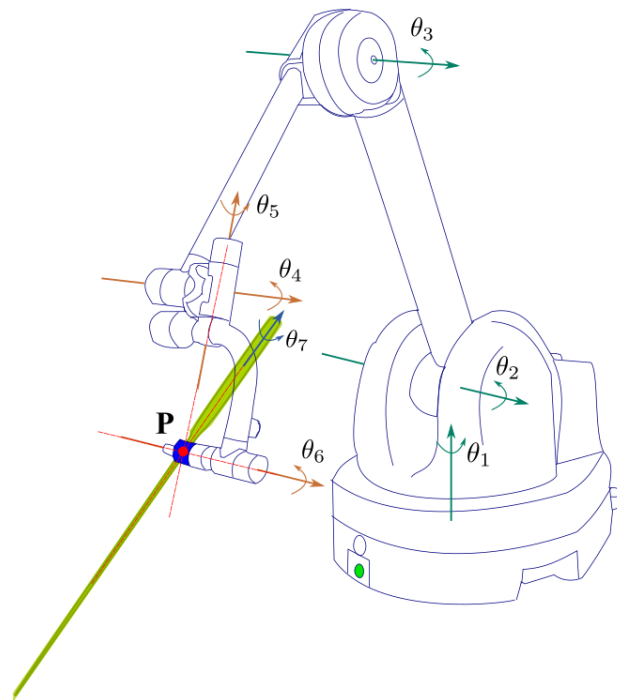


Fig. 2.1 The sketch of the comanipulator Achilles.

The first three joints are equipped with electromagnetic brakes while the last three joints have no brakes. The control of brakes is binary: when the robot is unpowered, the brakes are blocked, exhibiting a high resistive torque; when the robot is powered on, the brakes are closed, providing a null torque. Therefore, the robot can be locked to ensure safety in case of power failure.

All joints are equipped with position sensors except for joint 7. For joints 1, 2 and 3, the sensors are precise optical encoders with very small noise. Sensors of joints 4, 5 and 6 are potentiometers with more noise. Fig. 2.2 shows the comparison of noise level between optical encoders and potentiometers when the robot keeps still. As joint 7 is not sensed, the joint sensors can be used only to compute the position of any point belonging to the joint 7 axis.

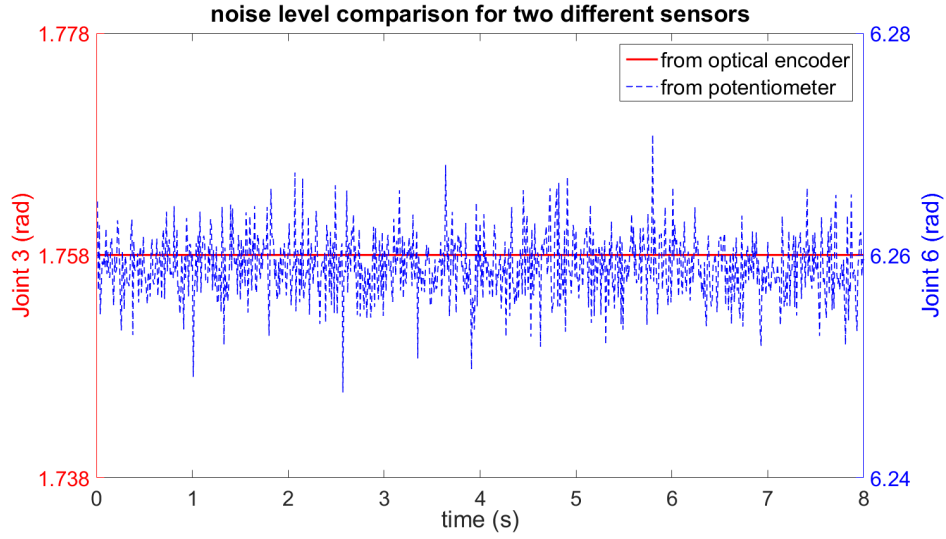


Fig. 2.2 **The comparison of joint noise level of Achilles.** The red solid line shows the noise level of joint 3, obtained from an optical encoder on the order of 10^{-14} while the blue dashed line illustrates the noise level of joint 6, obtained from a potentiometer on the order of 10^{-3} . The data are collected when the robot keeps static.

The robot maintains a high transparency and backdrivability (low friction and low inertia) thanks to the following designs:

- The motors are placed near the robot base in such a way that their mass does not significantly affect the robot's inertia.
- Load springs are mounted on joints 2 and 3 to compensate for the robot link weight.

These features also make the robot lightweight and compact in volume, guaranteeing a small space occupation and an easy installation or uninstallation. The robot base is placed on the examination table beside the patient's bed.

2.2.2 Kinematics

Cartesian calculation

The sketch of the robot-assisted surgical system is shown in Fig. 2.3, where the robot holds an instrument at wrist center P . Two different frames are defined: frame $\mathcal{F}_0 = (O, (\mathbf{x}_0, \mathbf{y}_0, \mathbf{z}_0))$ attached to the robot base (fixed), thus called robot base frame, and frame $\mathcal{F}_I = (P, (\mathbf{x}_I, \mathbf{y}_I, \mathbf{z}_I))$ attached to the instrument with origin at point P and \mathbf{z}_I along the instrument axis, thus called robot end-effector frame or instrument frame.

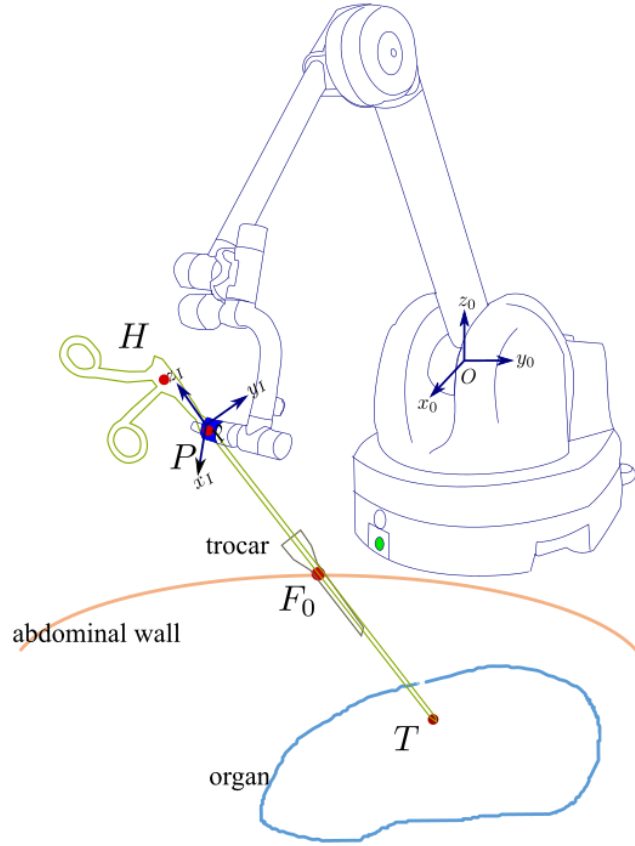


Fig. 2.3 Kinematics of Achilles System.

The instrument is inserted into the abdomen at the entry point F through a trocar and its tip keeps directly in contact with the tissues. Point H and point T are defined as the centers of handle and tip of the instrument, respectively, in such a way that H , P and T are aligned on a typical long rigid laparoscopic surgical instrument. Their positions are known in the robot end-effector frame \mathcal{F}_I .

With the Denavit-Hartenberg parameters [69] given in Table. 2.1, the transformation matrix from instrument frame \mathcal{F}_I to robot base frame \mathcal{F}_0 can be calculated as:

$$\mathbf{T}_{0 \rightarrow I}(\theta) = \mathbf{T}_{0 \rightarrow 1}(\theta_1) \mathbf{T}_{1 \rightarrow 2}(\theta_2) \dots \mathbf{T}_{6 \rightarrow 7}(\theta_7) \mathbf{T}_{7 \rightarrow I}, \quad (2.1)$$

with $\theta = [\theta_1, \dots, \theta_7]^T$ and $\mathbf{T}_{i-1 \rightarrow i}(\theta_i)$ ($i \in \{1, \dots, 7\}$) representing homogeneous transformation. θ is the joint vector of the robot with θ_i as its i^{th} component.

From $\mathbf{T}_{0 \rightarrow I}(\theta)$, kinematic models mapping joint angles into wrist position and orientation at point P can be extracted. Namely, the position of wrist point P , denoted as ${}^0\mathbf{p}_P$, and the instrument axis vector, denoted as ${}^0\mathbf{z}_I$, both expressed in the robot base frame \mathcal{F}_0 , can be

Table 2.1 Denavit-Hartenberg parameters of Achilles

i	α_{i-1}	a_{i-1}	d_i	θ_i
1	0	0	0	θ_1
2	$-\pi/2$	0	0	θ_2
3	0	0.45	-0.045	θ_3
4	0	0.3023	0.045	θ_4
5	$-\pi/2$	0	0.1848	θ_5
6	$\pi/2$	0	0	θ_6
7	$\pi/2$	0	0	θ_7

obtained. ${}^0\mathbf{p}_P$ depends only on the first four joint angles, the first three of which are measured precisely thanks to the high resolution optical encoders, the fourth does not vary except for the occasional configuration adjustment. ${}^0\mathbf{z}_I$ depends not only on $\theta_1, \theta_2, \theta_3, \theta_4$, but also on θ_5 and θ_6 , whose values are obtained from potentiometers, affected by noise. With ${}^0\mathbf{p}_P$ known, position of any point M belonging to the instrument can be computed, provided that the distance between point P and point M is known (depending on which the pure translational matrix $\mathbf{T}_{7 \rightarrow I}$ is calculated). However, ${}^0\mathbf{p}_M$ (when M is not P) is affected by noise since the computation of $\mathbf{T}_{7 \rightarrow I}$ relies on θ_5 and θ_6 . For illustration purpose, both the norm of the position at point P (with red solid line) and that at point T (with blue dashed line) are depicted in Fig. 2.4.

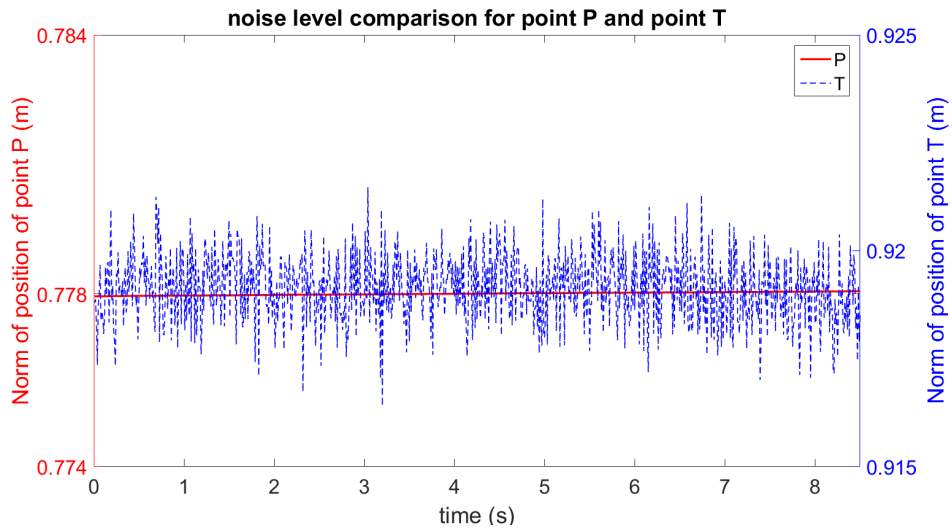


Fig. 2.4 Norms of positions of point P and T . The red solid line shows the noise level of ${}^0\mathbf{p}_P$ on the order of 10^{-4} while the blue dashed line indicates the noise level of ${}^0\mathbf{p}_T$ on the order of 10^{-3} . The data are collected when the robot keeps static.

Velocity calculation

The translational velocity ${}^0\mathbf{v}_P$ of wrist center P and the rotational velocity $\omega_{I/0}$ of the instrument with respect to robot base can be computed from the joint velocity vector $\dot{\theta} = [\dot{\theta}_1 \dots \dot{\theta}_7]^T$ using the kinematic model:

$$\begin{pmatrix} {}^0\mathbf{v}_P \\ \omega_{I/0} \end{pmatrix} = \underbrace{\begin{pmatrix} \mathbf{J}_{v1,P} & \mathbf{J}_{v2,P} & 0 \\ \mathbf{J}_{\omega 1} & \mathbf{J}_{\omega 2} & \mathbf{J}_{\omega 3} \end{pmatrix}}_{\mathbf{J}_P} \dot{\theta}, \quad (2.2)$$

where \mathbf{J}_P is the 6×7 Jacobian matrix at point P . $\mathbf{J}_{v1,P}$, $\mathbf{J}_{\omega 1}$ and $\mathbf{J}_{\omega 3}$ are 3×3 sub-matrices while $\mathbf{J}_{v2,P}$ and $\mathbf{J}_{\omega 2}$ are 3×1 sub-matrices. The upper right null sub-matrix indicates that the movement of the last three joints has no influence on ${}^0\mathbf{v}_P$. Note that in our work, \mathbf{J}_P is assumed to be full rank, which is practically guaranteed in the prototype due to physical joint limit that leaves kinematic singularities out of the workspace.

As mentioned in Sec. 2.2.1, joint 4 is an indexed joint used for robot configuration adjustment. This indicates that only when the configuration changes, $\dot{\theta}_4$ is not equal to 0. Therefore, during the surgical gesture, we assume that $\dot{\theta}_4 = 0$. Eq. (2.2) is hence simplified as:

$$\begin{pmatrix} {}^0\mathbf{v}_P \\ \omega_{I/0} \end{pmatrix} = \begin{pmatrix} \mathbf{J}_{v1,P} & 0 \\ \mathbf{J}_{\omega 1} & \mathbf{J}_{\omega 3} \end{pmatrix} \dot{\theta}', \quad (2.3)$$

where $\dot{\theta}' = [\dot{\theta}_1 \ \dot{\theta}_2 \ \dot{\theta}_3 \ \dot{\theta}_5 \ \dot{\theta}_6 \ \dot{\theta}_7]^T$.

Another way to compute ${}^0\mathbf{v}_P$ is through differentiation of ${}^0\mathbf{p}_P$, which we adopt in this work. However, the procedure of differentiation largely magnifies the noise amplitude. To solve this problem, we employ a first order low pass digital filter to reduce noise effect. The filter time constant τ is experimentally tuned in such a way that the filter can sufficiently get rid of noise without causing large delay. Fig. 2.5 illustrates the unfiltered and filtered velocities at point P , represented by the blue dashed line and the red solid line, respectively. τ is chosen as 0.05 s.

Once the robot wrist velocity ${}^0\mathbf{v}_P$ is known, it is easy to obtain the velocity ${}^0\mathbf{v}_M$ of any point M lying on the instrument. This could be implemented through differentiation of ${}^0\mathbf{p}_M$, whose result is noisy, or through a velocity relationship of points lying on the instrument, called lever model, which will be described in detail in Chapter. 3.

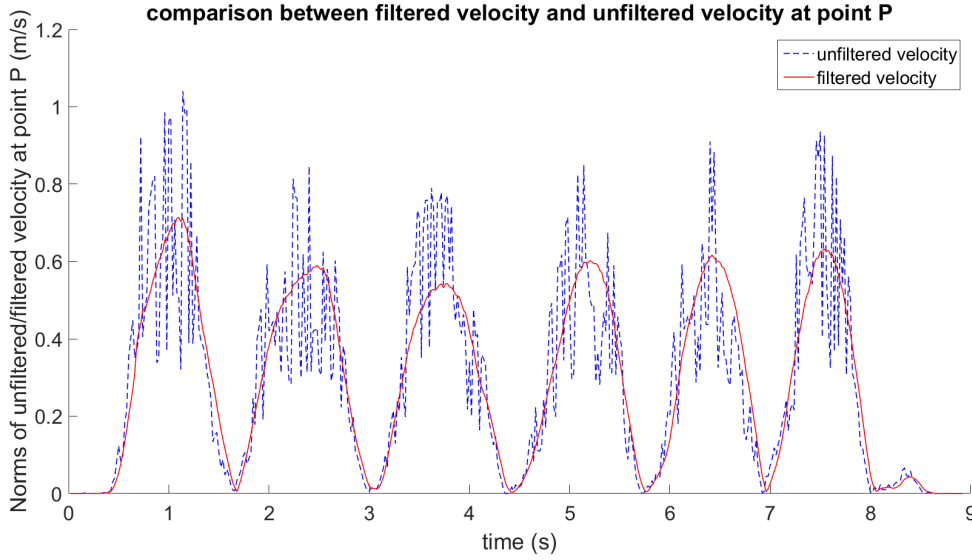


Fig. 2.5 Norms of the unfiltered and filtered velocities at point P when the robot is manually moved by a user while applying a null joint torque. The blue dashed line represents the unfiltered velocity ${}^0\mathbf{v}_P$ and the red solid line shows the filtered velocity.

2.2.3 Actuation

In terms of the low level electronics, the motor torque is controlled by a current loop. Namely, the control input for the motors of the first three joints is current i_i , $i \in \{1, 2, 3\}$. Current i_i corresponds to a joint torque τ_i with a scalar factor k_i representing the motor torque constant and the transmission ratio:

$$\tau_i = k_i i_i, \quad i \in \{1, 2, 3\}. \quad (2.4)$$

With this relationship known, in the following, we consider torque as the control input of the first three joints' motors.

Due to static-kinematic duality, the transpose of the Jacobian matrix can be used to map the robot wrench applied through P to the end-effector into the joint torques. When joint 4 is at the locked state, the static transmission model is written as:

$$\boldsymbol{\tau} = \begin{pmatrix} \mathbf{J}_{v1,P}^T & \mathbf{J}_{\omega1}^T \\ 0 & \mathbf{J}_{\omega3}^T \end{pmatrix} \begin{pmatrix} {}^0\mathbf{f}_P \\ {}^0\mathbf{m}_P \end{pmatrix}, \quad (2.5)$$

where $\boldsymbol{\tau} = [\tau_1 \ \tau_2 \ \tau_3 \ \tau_5 \ \tau_6 \ \tau_7]^T$, ${}^0\mathbf{f}_P$ is the force exerted by the robot to the instrument and \mathbf{m}_P is the moment applied by the robot at point P .

Since joints 5 to 7 are not motor-driven, their torques are null. We thus have:

$$\begin{pmatrix} [\tau_1 \ \tau_2 \ \tau_3]^T \\ [0 \ 0 \ 0]^T \end{pmatrix} = \begin{pmatrix} \mathbf{J}_{v1,P}^T & \mathbf{J}_{\omega1}^T \\ 0 & \mathbf{J}_{\omega3}^T \end{pmatrix} \begin{pmatrix} {}^0\mathbf{f}_P \\ {}^0\mathbf{m}_P \end{pmatrix}. \quad (2.6)$$

From Eq. (2.6), it is seen that the robot wrench has a null moment at P . Therefore, the wrench exerted by the robot motors at P is a pure force, which can be expressed in \mathcal{F}_0 as:

$$\{\mathcal{W}\}_P = \left\{ \begin{array}{c} {}^0\mathbf{f}_P \\ {}^0\mathbf{m}_P = \mathbf{0} \end{array} \right\}. \quad (2.7)$$

Thus Eq. (2.6) can be simplified as:

$$(\tau_1 \ \tau_2 \ \tau_3)^T = \mathbf{J}_{v1,P}^T {}^0\mathbf{f}_P. \quad (2.8)$$

Eq. (2.8) maps from the robot wrench applied at point P to the three active joints torques. It indicates that it is sufficient to control the robot kinematics at point P by just controlling the three motors since it only requires to generate a pure force at this point.

2.2.4 General idea of the comanipulated system

From the above descriptions, we summarize the measures provided in real time by the robot as follows:

- the position of point M with respect to frame \mathcal{F}_0 : ${}^0\mathbf{p}_M$ ($M = P, H, T$).
- the orientation of the instrument axis with respect to the frame \mathcal{F}_0 : ${}^0\mathbf{z}_I$.
- the velocity of point M with respect to frame \mathcal{F}_0 : ${}^0\mathbf{v}_M$ ($M = P, H, T$).
- the rotational velocity of the instrument frame \mathcal{F}_I with respect to frame \mathcal{F}_0 : $\omega_{I/0}$.

The command sent back to control the robot in real time is the following:

- the pure force of the robot exerted at point P with respect to frame \mathcal{F}_0 whose components are expressed in base $(\mathbf{x}_0, \mathbf{y}_0, \mathbf{z}_0)$: ${}^0\mathbf{f}_P$.

Practically how the comanipulated system works as a whole: The sensors attached to the comanipulator, with high or low noise, detect the joint positions, which are sent to the robot internally embedded controller and mapped into the end-effector position or velocity. The robot is connected to a Windows desktop (Intel i5, 2.50 GHz, 8.00 G RAM) through an

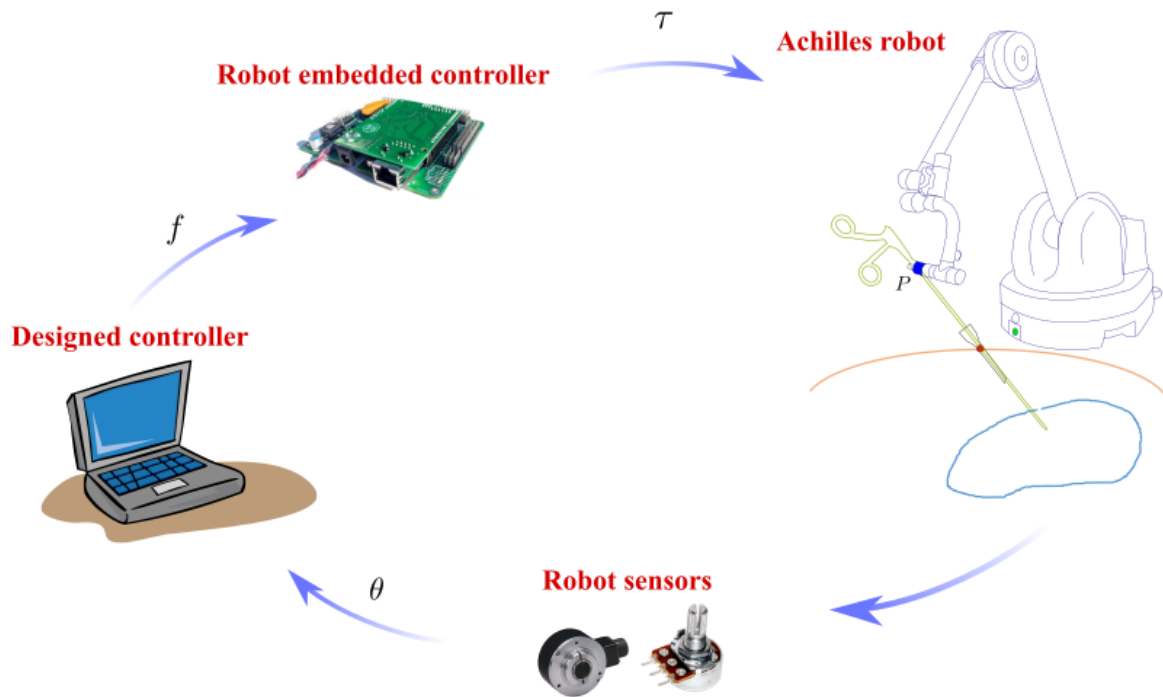


Fig. 2.6 Illustration of the comanipulated system.

Internet cable, on which the designed controller of Achilles is implemented in Qt. Data or commands are exchanged through the robot service provided by the robot company Haption installed on the computer. The program is designed in the way to ensure that the sampling rate of the control loop of Achilles is approximately 1000 Hz. Based on the information provided by the robot controller, different control laws such as instrument gravity compensation or trocar detection and localization could be developed and implemented to compute control commands. Then the force commands are further transformed into torques by the robot embedded controller using the Jacobian matrix through the APIs provided by Haption, which are then sent back to serve as the motor input in the form of current signals. Notice that due to the passive wrist point of Achilles, the force exerted by the robot is a pure force with null moment at the wrist center point P .

2.3 Gravity compensation for laparoscopic instrument

2.3.1 Implementation

Since the mass and the structure of different instruments may vary from one to another, we take JAiMY as an example to show how the gravity compensation could be implemented.

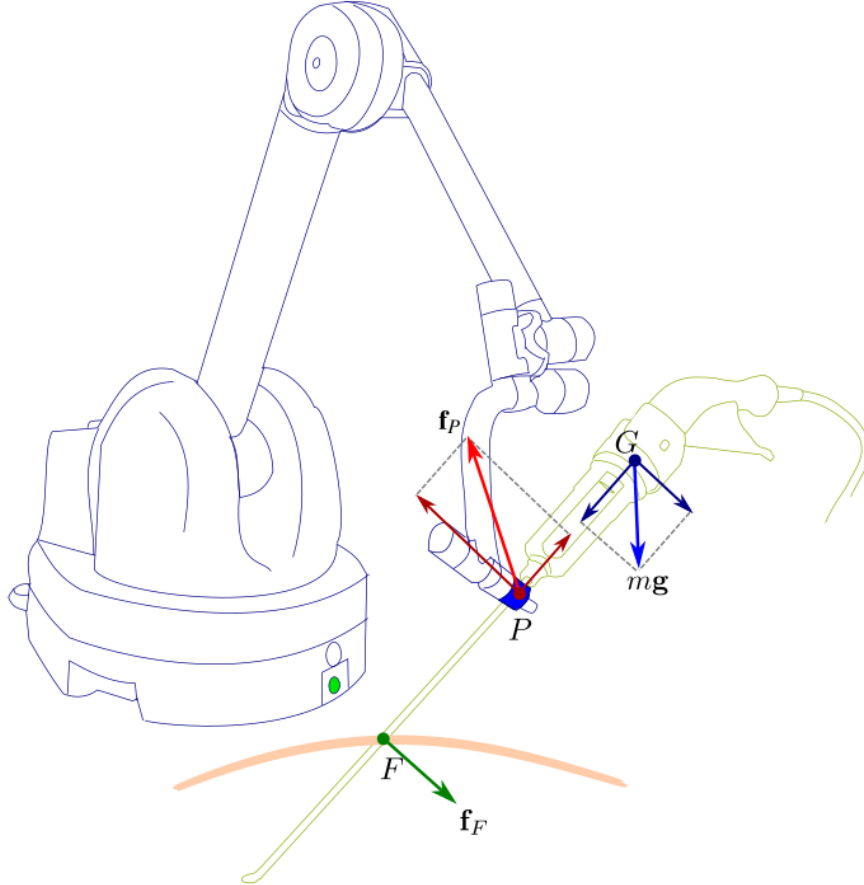


Fig. 2.7 Illustration of gravity compensation.

We assume that the center of gravity of the instrument, illustrated as point G in Fig. 2.7, is known. In reality, it can be easily found by doing balancing experiments. For the sake of simplicity, G is considered to be aligned with P , H and T . Then the gravity wrench \mathcal{W}_g expressed at point G is

$$\{\mathcal{W}_g\}_G = \begin{Bmatrix} m\mathbf{g} \\ \mathbf{0} \end{Bmatrix}, \quad (2.9)$$

where m denotes the mass of the instrument, and \mathbf{g} denotes the gravity field vector with the norm $\|\mathbf{g}\| = 9.81 \text{ m} \cdot \text{s}^{-2}$.

The sum of applied wrenches after gravity compensation is supposed to be a null wrench. We can write the expression at point F :

$$\sum \{\mathcal{W}\}_F = \mathbf{0} . \quad (2.10)$$

Forces that could exert a wrench at point F are instrument gravity, robot force and trocar force. The instrument is supposed to keep immobile without dropping when the surgeon does not hold it or not add forces on it. Therefore, human force is not included in Eq. (2.10). In addition, the tissue or the organ may also apply a wrench at point F when they contact with the instrument tip. However, as mentioned before, there should be no tip-tissue contact without intentional manipulation supervised by the surgeon. Therefore, we do not consider this factor neither for Eq. (2.10). Finally, Eq. (2.10) is expanded as:

$$\{\mathcal{W}_g\}_F + \{\mathcal{W}_r\}_F + \{\mathcal{W}_f\}_F = \mathbf{0} , \quad (2.11)$$

where $\{\mathcal{W}_g\}_F$ is the gravity wrench applied to the instrument at point F , which is expressed as:

$$\{\mathcal{W}_g\}_F = \left\{ \begin{array}{c} m\mathbf{g} \\ \mathbf{d}_{FG} \times m\mathbf{g} \end{array} \right\} . \quad (2.12)$$

with \mathbf{d}_{FG} being the vector from point F to point G . $\mathbf{d}_{FG} = d_{FG}\mathbf{z}_I$, where the value of d_{FG} changes with the insertion depth of the instrument. \mathbf{z}_I is the z axis of the instrument frame \mathcal{F}_I .

$\{\mathcal{W}_r\}_F$ is the robot wrench applied at point F , written as:

$$\{\mathcal{W}_r\}_F = \left\{ \begin{array}{c} \mathbf{f}_P \\ \mathbf{d}_{FP} \times \mathbf{f}_P \end{array} \right\} . \quad (2.13)$$

where \mathbf{f}_P is the robot force exerted at point P and \mathbf{d}_{FP} is the vector from point F to point P whose norm also varies according to the instrument insertion depth.

As to $\{\mathcal{W}_f\}_F$, it is the wrench due to the force applied by the trocar to the instrument. Of course, the friction between the abdomen and the trocar may affect $\{\mathcal{W}_f\}_F$. Since this value greatly depends on the trocar type, it is not considered for a rough implementation of gravity compensation. Force exerted at point F generates no torque, therefore, one has:

$$\{\mathcal{W}_f\}_F = \left\{ \begin{array}{c} \mathbf{f}_F \\ \mathbf{0} \end{array} \right\} . \quad (2.14)$$

Combining Eq. (2.11) to Eq. (2.14), one can write:

$$\begin{cases} m\mathbf{g} + \mathbf{f}_P + \mathbf{f}_F = \mathbf{0} . & (a) \\ \mathbf{d}_{FG} \times m\mathbf{g} + \mathbf{d}_{FP} \times \mathbf{f}_P = \mathbf{0} . & (b) \end{cases} \quad (2.15)$$

Writing:

$$\mathbf{f}_P = a_P \mathbf{x}_I + b_P \mathbf{y}_I + c_P \mathbf{z}_I , \quad (2.16)$$

Multiplying \mathbf{z}_I^T with Eq. (2.15) (a) one gets:

$$\mathbf{z}_I^T \cdot m\mathbf{g} + \mathbf{z}_I^T \cdot \mathbf{f}_P + \mathbf{z}_I^T \cdot \mathbf{f}_F = 0 . \quad (2.17)$$

Generally, the component of \mathbf{f}_F perpendicular to the instrument axis is far larger than the parallel component. Therefore, we approximately have $\mathbf{z}_I^T \cdot \mathbf{f}_F = 0$. With $\mathbf{z}_I^T \cdot \mathbf{f}_P = c_P$, the coefficient c_P is calculated as:

$$c_P = -\mathbf{z}_I^T \cdot m\mathbf{g} . \quad (2.18)$$

Multiplying \mathbf{x}_I^T with Eq. (2.15) (b) one gets:

$$\mathbf{x}_I^T \cdot (\mathbf{d}_{FG} \times m\mathbf{g} + \mathbf{d}_{FP} \times \mathbf{f}_P) = 0 . \quad (2.19)$$

Using the rule of scalar triple product, one has:

$$m\mathbf{g}^T \cdot (\mathbf{x}_I \times \mathbf{d}_{FG}) + \mathbf{f}_P^T \cdot (\mathbf{x}_I \times \mathbf{d}_{FP}) = 0 . \quad (2.20)$$

Notice that $\mathbf{d}_{FG} = d_{FG} \cdot \mathbf{z}_I$ and $\mathbf{d}_{FP} = d_{FP} \cdot \mathbf{z}_I$, one gets:

$$m\mathbf{g}^T \cdot (-d_{FG} \cdot \mathbf{y}_I) + \mathbf{f}_P^T \cdot (-d_{FP} \cdot \mathbf{y}_I) = 0 . \quad (2.21)$$

Knowing $\mathbf{f}_P^T \cdot \mathbf{y}_I = b_P$, the coefficient b_P is calculated as:

$$b_P = -m \frac{d_{FG}}{d_{FP}} \mathbf{g}^T \cdot \mathbf{y}_I . \quad (2.22)$$

Similarly, the coefficient a_P is:

$$a_P = -m \frac{d_{FG}}{d_{FP}} \mathbf{g}^T \cdot \mathbf{x}_I . \quad (2.23)$$

Therefore, combining Eq. (2.18), Eq. (2.22) and Eq. (2.23), we obtain the force generated by the robot at point P :

$$\mathbf{f}_P = -m(\beta(\mathbf{I} - \mathbf{z}_I \mathbf{z}_I^T) + \mathbf{z}_I \mathbf{z}_I^T) \mathbf{g}, \quad \beta = \frac{d_{FG}}{d_{FP}}. \quad (2.24)$$

From Eq. (2.24), we see that the robot force can actually be decomposed into two parts. One component, $-m \cdot \mathbf{z}_I \mathbf{z}_I^T \mathbf{g}$, aims to cancel out the gravity projected along the instrument axis so as to prevent the instrument from getting inserted into the patient's abdomen unintentionally. The left part, which is perpendicular to the instrument axis, is used to generate a moment at the trocar entry point F to counteract the moment generated by the instrument gravity.

Note that the ratio β depends on the trocar information. To calculate β , it is necessary to know the trocar position in real time. In other words, only when the trocar information is known, can the gravity compensation method described above be used.

2.3.2 Evaluation

For JAiMY, we measured its mass as 0.48 kg, and the distance d_{PG} from the robot wrist position to the instrument center of gravity as 0.12 m. With these information, we can implement gravity compensation for JAiMY easily according to Eq. (2.24).

In order to evaluate the program, we carried out a simple experiment where JAiMY was placed at different configurations (positions and orientations) with respect to the robot base. An interface is provided in such a way that an additional force ${}^0\mathbf{f}_z$ can be manually added in the positive or negative direction of \mathbf{z}_0 axis of base frame. At each configuration where the instrument is in a equilibrium condition, we first increase the force in the positive \mathbf{z}_0 direction until the instrument loses balance and starts to move. This value is recorded. Then the same procedure is performed in the negative \mathbf{z}_0 direction at the same instrument configuration. Fig. 2.8 illustrates a typical instrument configuration where a force ${}^0\mathbf{f}_z$ is added in the negative \mathbf{z}_0 direction.

There are in total 30 different instrument configurations chosen, roughly covering the workspace of the robot and the possible movement areas of the instrument. Fig. 2.9 illustrates the distribution of the collected configurations as well as the corresponding forces required to break the original equilibrium. Table. 2.2 lists the norm of the statistical values of the experimental analysis.

The purpose of adding ${}^0\mathbf{f}_z$ is to balance all the forces exerting to the instrument so that a static equilibrium could be reached when inserted into the trocar. Ideally, ${}^0\mathbf{f}_z$ equals $\mathbf{0}$. However, in real situation, the force generated by the robot to compensate the gravity might

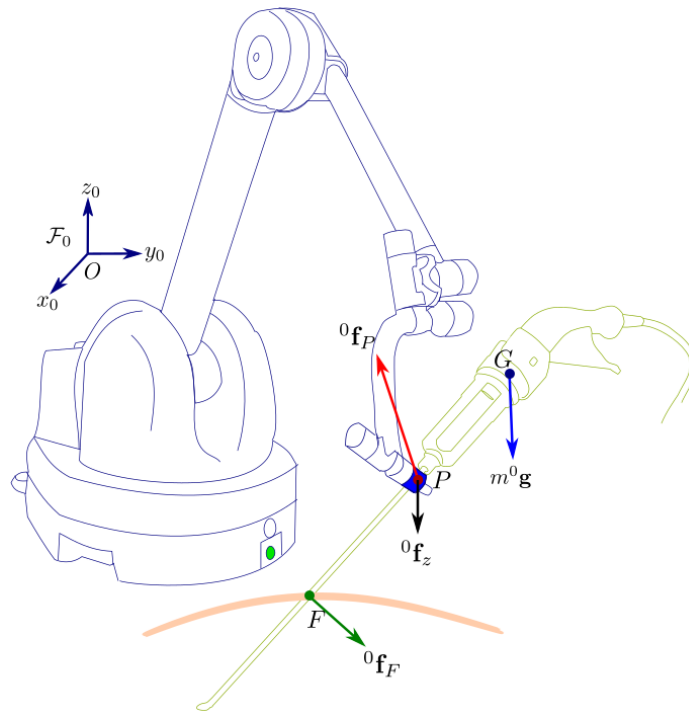


Fig. 2.8 A typical instrument configuration for gravity compensation experiment.

not be enough due to disturbing factors such as the cable of the instrument, trocar friction, not precise measurement of instrument mass and distance of d_{PG} , to name a few. From Table. 2.2 we see that the maximum norms of force for both positive and negative \mathbf{z}_0 direction are around 2 N while the minimum values are more than 10 times less. This signifies that the trocar friction has a varied influence on the instrument moment at the trocar insertion point with the change of instrument position and orientation. This may also be explained by the imperfect gravity compensation of the robot weight from springs.

Table 2.2 Experimental results for instrument gravity compensation

Force(N)	\mathbf{z}_0	$-\mathbf{z}_0$
Max	2.13	1.94
Min	0.15	0.13
Mean	0.93	0.85
Standard Deviation	0.56	0.45

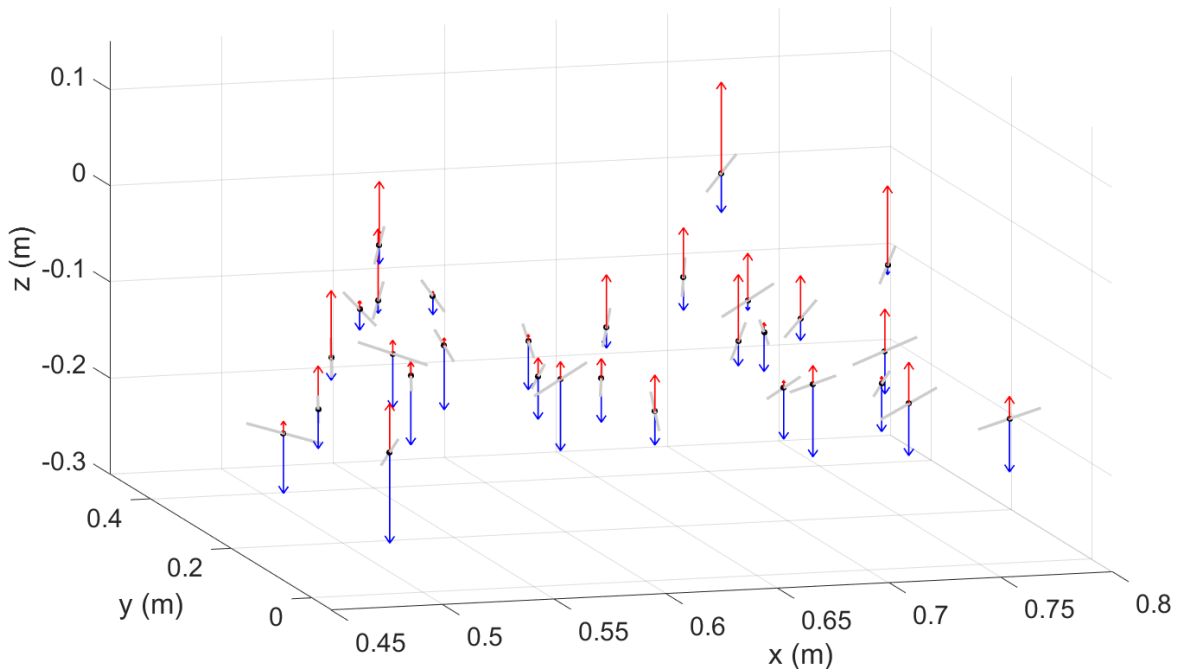


Fig. 2.9 **The experimental results for instrument gravity compensation.** 30 configurations are plotted, with black dots representing the robot wrist position ${}^0\mathbf{p}_P$, gray line representing the instrument axis. The red and blue arrows indicate the forces added upwards in the positive \mathbf{z}_0 and downwards in the negative \mathbf{z}_0 direction, respectively.

2.4 Robust trocar detection and localization

2.4.1 Specific aims

Context: comanipulation

Achilles, as a comanipulated robot, displays force fields aimed at guiding the surgeon's gestures. For example, the gravity compensation for the laparoscopic instrument which is described in detail in last section releases surgeons from the fatigue caused by holding weighty instruments. The implementation of these functions requires an estimation of the trocar location, see *e.g.* [70]. This estimation is to be run on the fly while the robot and the surgeon perform a comanipulated task.

Without loss of generality, we consider that, in the free mode, the surgeon can manipulate the instrument through a trocar to perform a given gesture. He/she may remove it from the trocar, and insert it through another incision. The robot never imposes movements.

We then look for an algorithm that can robustly detect the trocar presence and further obtain its position in real time without requiring any prior information or registration. The

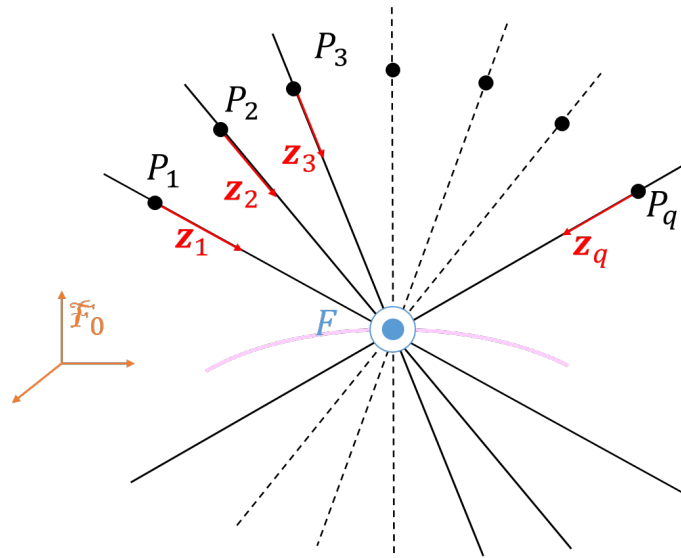


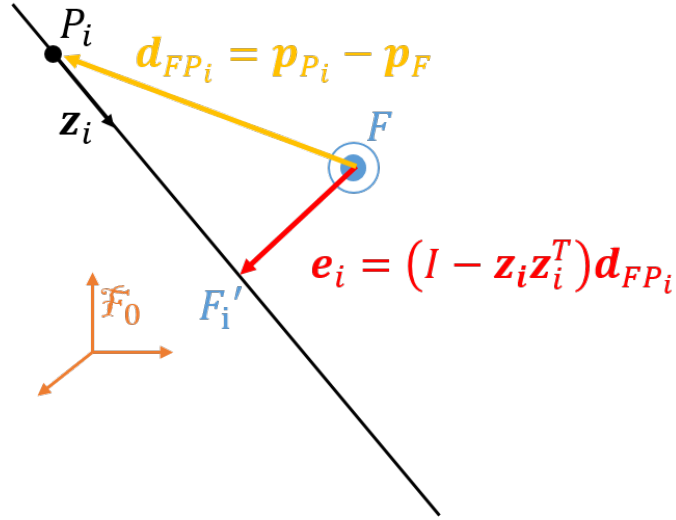
Fig. 2.10 **Principle of trocar detection:** Ideally, the fulcrum point F is the intersection of the instrument axes (P_i, \mathbf{z}_i) , $i \in \{1 \dots q\}$ measured from q different instantaneous robot configurations.

algorithm shall work without being able of imposing a movement. Also, it shall allow to detect position changes of both patient and robot base without readjustment of the equipment during the surgical operation.

Principle of trocar position estimation

Fig. 2.10 illustrates the principle used for trocar localization. The reference frame is a frame \mathcal{F}_0 attached to the base of the robot. The coordinates ${}^0\mathbf{p}_F$ of the fulcrum point F in \mathcal{F}_0 are to be determined from geometric measures in q configurations. At the i^{th} configuration, the instrument axis is a straight line passing through a given point P_i , and directing along a given unit vector \mathbf{z}_i . It is assumed that, from the joint position sensors of the robot, and thanks to a kinematic model, we can measure the position ${}^0\mathbf{p}_{P_i}$ of P_i and the components ${}^0\mathbf{z}_i$ of \mathbf{z}_i in frame \mathcal{F}_0 , $\forall i \in \{1 \dots q\}$.

In theory, whenever the instrument is inserted into a trocar, all the lines intersect at the fulcrum F . In practice, due to measurement noise, backlash between the trocar and the instrument, tissue deformations or calibration errors in the robot kinematic model, successive lines will not perfectly intersect. An optimization algorithm is therefore to be used to estimate the “best fulcrum location”, given a set on straight lines. This is done in the next section.

Fig. 2.11 Projection of F into the instrument axis.

2.4.2 Least square algorithm

To estimate the trocar location from a set of q straight lines (P_i, \mathbf{z}_i) , a simple solution is to find the point F whose average distance from the given lines is minimal.

As illustrated in Fig. 2.11, given a point F , and the i^{th} straight line (P_i, \mathbf{z}_i) , the vector \mathbf{e}_i from F to its projection F_i' onto (P_i, \mathbf{z}_i) is given by:

$$\mathbf{e}_i = \mathbf{d}_{F_i'F} = \mathbf{d}_{FP_i} - \mathbf{d}_{F_i'P_i}, \quad (2.25)$$

where \mathbf{d}_{AB} denotes the vector from a point A to a point B .

Furthermore:

$$\mathbf{d}_{F_i'P_i} = (\mathbf{z}_i^T \mathbf{d}_{FP_i}) \mathbf{z}_i. \quad (2.26)$$

Substituting Eq. (2.26) to Eq. (2.25) yields:

$$\mathbf{e}_i = (\mathbf{I} - \mathbf{z}_i \mathbf{z}_i^T) \mathbf{d}_{FP_i}. \quad (2.27)$$

In the base frame \mathcal{F}_0 , this last equation writes:

$${}^0\mathbf{e}_i = \underbrace{(\mathbf{I} - {}^0\mathbf{z}_i {}^0\mathbf{z}_i^T)}_{=: {}^0\mathbf{b}_i} {}^0\mathbf{p}_{P_i} - \underbrace{(\mathbf{I} - {}^0\mathbf{z}_i {}^0\mathbf{z}_i^T)}_{=: {}^0\mathbf{A}_i} {}^0\mathbf{p}_F. \quad (2.28)$$

Grouping all the equations for q measurements yields:

$${}^0_q\mathbf{e} = {}^0_q\mathbf{b} - {}^0_q\mathbf{A} \cdot {}^0\mathbf{p}_F, \quad (2.29)$$

where:

$${}^0_q\mathbf{A} = \begin{pmatrix} {}^0\mathbf{A}_1 \\ {}^0\mathbf{A}_2 \\ \dots \\ {}^0\mathbf{A}_i \\ \dots \\ {}^0\mathbf{A}_q \end{pmatrix}, \quad {}^0_q\mathbf{b} = \begin{pmatrix} {}^0\mathbf{b}_1 \\ {}^0\mathbf{b}_2 \\ \dots \\ {}^0\mathbf{b}_i \\ \dots \\ {}^0\mathbf{b}_q \end{pmatrix}, \quad {}^0_q\mathbf{e} = \begin{pmatrix} {}^0\mathbf{e}_1 \\ {}^0\mathbf{e}_2 \\ \dots \\ {}^0\mathbf{e}_i \\ \dots \\ {}^0\mathbf{e}_q \end{pmatrix}. \quad (2.30)$$

In the ideal configuration, when F is the fulcrum location, ${}^0_q\mathbf{e}$ equals zero. With real data, this will not happen. We compute an estimate \hat{F}_q of F by minimizing the norm of ${}^0_q\mathbf{e}$. It is well known that, according to Least Square optimization, the coordinates of this estimate can be computed by:

$${}^0\mathbf{p}_{\hat{F}_q} = \underset{{}^0\mathbf{p}_F}{\operatorname{argmin}} \left(\| {}^0_q\mathbf{b} - {}^0_q\mathbf{A} \cdot {}^0\mathbf{p}_F \|^2 \right) = \left({}^0_q\mathbf{A}^T \cdot {}^0_q\mathbf{A} \right)^{-1} {}^0_q\mathbf{A}^T {}^0_q\mathbf{b}. \quad (2.31)$$

Practically implementing this algorithm requires answering two main questions. The first one concerns the selection of measures to be included for optimization. The second one concerns the interpretation of the result. Indeed, even if the instrument is not inserted in the trocar, Eq. (2.31) will provide an estimation. Therefore, after the computation of ${}^0\mathbf{p}_{\hat{F}_q}$, it is necessary to evaluate the effectiveness of this value to be used as an estimation of the trocar position. To do that, we further calculate the average of the norm of the estimated error, denoted as e_q , which is:

$$e_q = \frac{1}{q} \sum_{i=1}^q \left\| {}^0\mathbf{A}_i \cdot {}^0\mathbf{p}_{\hat{F}_q} - {}^0\mathbf{b}_i \right\|. \quad (2.32)$$

The smaller is the value of e_q , the higher is the probability that the instrument passes through a fixed point.

2.4.3 Trocar detection and localization

In order to practically implement the algorithm described above, the general principle is as follows:

Step 1. Built a data list L_q containing q measured data pairs $c_i = ({}^0\mathbf{p}_{P_i}, {}^0\mathbf{z}_i)$, $i = 1, 2, \dots, q$.

Step 2. Apply the LS method to L_q and calculate the trocar position ${}^0\mathbf{p}_{\hat{F}_q}$ from Eq. (2.31).

Step 3. Compute the average of the norm of the estimated error e_q according to Eq. (2.32).

Step 4. Use e_q to determine whether a trocar is detected or not. If a trocar is detected, then ${}^0\mathbf{p}_{\hat{F}_q}$ is its position, otherwise, ${}^0\mathbf{p}_{\hat{F}_q}$ is abandoned.

In the following, we discuss the realization of the algorithm in detail.

Building a data list for trocar estimation

We know that to perform the least square method, more than one measurement is required. Therefore, a data list, denoted as L_q , is built to store q data pairs as the input of the estimation algorithm. The list is implemented with a circular buffer: Once q values have already been stored and a new value is to be considered, the oldest value is discarded. This allows for permanent updating of the data while forgetting the oldest measurement.

To select data pairs to be included list L_q , we should make sure each data pair c_i represents an instrument configuration different from others in the list, so as to ensure the effectiveness and the precision of the least square method. To this aim, two functions are defined in order to evaluate the displacement between two configurations.

1. **Linear displacement of the robot wrist center.** The linear displacement between two robot configurations characterized by $({}^0\mathbf{p}_{P_j}, {}^0\mathbf{z}_j)$ and $({}^0\mathbf{p}_{P_k}, {}^0\mathbf{z}_k)$, respectively, is defined by:

$$d_{j,k} = \|(\mathbf{I} - {}^0\mathbf{z}_j {}^0\mathbf{z}_j^T) ({}^0\mathbf{p}_{P_j} - {}^0\mathbf{p}_{P_k})\| . \quad (2.33)$$

Notice that the distance $d_{j,k}$ is not affected by displacements along the instrument axis, as they do not contribute to change Eq. (2.27).

2. **Orientation of the instrument axis.** The orientation displacement between two robot configurations characterized by $({}^0\mathbf{p}_{P_j}, {}^0\mathbf{z}_j)$ and $({}^0\mathbf{p}_{P_k}, {}^0\mathbf{z}_k)$, respectively, is defined by:

$$\theta_{j,k} = \text{acos}({}^0\mathbf{z}_j, {}^0\mathbf{z}_k) . \quad (2.34)$$

Notice that any rotation of the instrument around \mathbf{z} does not affect $\theta_{j,k}$.

From these distances, the pseudo code of building a data list L_q containing q data pairs is detailed in Algorithm 1 where:

- `measure_from_robot()` reads the robot joint position and returns the pair $({}^0\mathbf{p}_P, {}^0\mathbf{z})$.

- $\text{add_to_circular_buffer}(L_q, c, q)$ adds c to the list L_q by concatenation, and, if the list length equals q , removes the oldest value of the list.
- δ_d and δ_θ are the linear and rotational displacements thresholds beyond which any new value shall be included.

Algorithm 1 Algorithm building a data list L_q with q data pairs

Initialization:

$c_1 \leftarrow \text{measure_from_robot}()$
 $L_q \leftarrow \{c_1\}$
 $i \leftarrow 2$

Periodic function (at sampling rate): :

$c_i \leftarrow \text{measure_from_robot}()$
if $[(d_{i-1,i} > \delta_d) \text{ or } (\theta_{i-1,i} > \delta_\theta)]$ **then**
 $L_q \leftarrow \text{add_to_circular_buffer}(L_q, c_i, n)$
 $i \leftarrow i + 1$
end if

Choosing q is also of primary importance. In general, to filter out the noise and to obtain a precise estimation, q shall be large. However, a large list takes longer time to be filled in, which slows down the estimation procedure and causes delays.

To deal with this dilemma, we build 2 lists, a small one L_m , with m data pairs, whose main purpose is to rapidly detect the existence of the trocar, and a larger one L_n , containing n components, which is mainly used to provide a stable and precise trocar position when the trocar has been detected. We denote the estimated trocar positions from these two lists as ${}^0\mathbf{p}_{\hat{F}_m}$ and ${}^0\mathbf{p}_{\hat{F}_n}$, respectively, and the associated trocar position estimation errors as e_m and e_n , respectively.

Trocar detection

In this section, we detail a second algorithm used to detect whether the trocar is present.

At the initialization, it is supposed that the instrument is not inserted into a trocar. Then building lists L_m and L_n starts. Whenever the shortest list, L_m , is full, a least square estimation is performed according to Eq. (2.31) and the associated error e_m is computed thanks to Eq. (2.32).

To detect presence of a trocar from this configuration, a test is made on the error e_m . When it is small enough (smaller than a threshold δ_{e_m}), this indicates that the instrument

probably passes through a fixed point, which most likely is a trocar. However, from the large set of experiments that were performed to assess the robustness of the approach, a special configuration was identified leading to false positive detection: The surgeon may move the instrument outside the patient (not inserted in a trocar) in such a way that the instrument orientation changes while P does not move. This is due to the fact that, with our comanipulation robot, P is the center of the robot passive wrist. In such a configuration, the LS algorithm detects P as the fulcrum point. To eliminate this false positive detection, a second criterion is used for trocar detection: The distance between P and \hat{F} shall be larger than a threshold Δ_{depth} , ensuring that the detected point is not P .

When a trocar has been detected, the algorithm shall detect when the surgeon extracts the instrument from the trocar. Two configurations occur.

1. When the long list L_n is not yet filled, we still have to rely on L_m to make a decision. Since the signal e_m is noisy due to the smallness of m , we detect an extraction of the instrument from the trocar when e_m is larger than a given threshold $\Delta_{e_m} > \delta_{e_m}$.
2. When L_n is full, we rely on e_n , which is less noisy than e_m , and compare it to a threshold Δ_{e_n} .

This corresponds to the pseudo-code of Algorithm 2, where $\text{Length}(L)$ returns the number of elements already included in a list L and $\text{Least_square_estimation}(L)$ performs a LS estimation from L and returns the estimated position and the associated error. Algorithm 2 runs at each sampling period, in parallel to Algorithm 1 that builds the lists.

Algorithm 2 Algorithm for trocar detection

Initialization:

trocar_is_present \leftarrow false

Periodic function (at sampling rate):

if trocar_is_present = false **then**

if Length(L_m) = m **then**

$\left({}^0\mathbf{p}_{\hat{F}_m}, e_m\right) \leftarrow$ Least_square_estimation(L_m)

if $e_m < \delta_{e_m}$ and $\|\mathbf{d}_{\hat{F}_m P}\| > \delta_{\text{depth}}$ **then**

 trocar_is_present \leftarrow true

$\hat{F} \leftarrow \hat{F}_m$

end if

end if

else

if Length(L_n) < n **then**

$\left({}^0\mathbf{p}_{\hat{F}_n}, e_n\right) \leftarrow$ Least_square_estimation(L_n)

if $e_n > \Delta_{e_n}$ **then**

 trocar_is_present \leftarrow false

else

$\hat{F} \leftarrow \hat{F}_n$

end if

else

$\left({}^0\mathbf{p}_{\hat{F}_n}, e_n\right) \leftarrow$ Least_square_estimation(L_n)

if $e_n > \Delta_{e_n}$ **then**

 trocar_is_present \leftarrow false

else

$\hat{F} \leftarrow \hat{F}_n$

end if

end if

end if

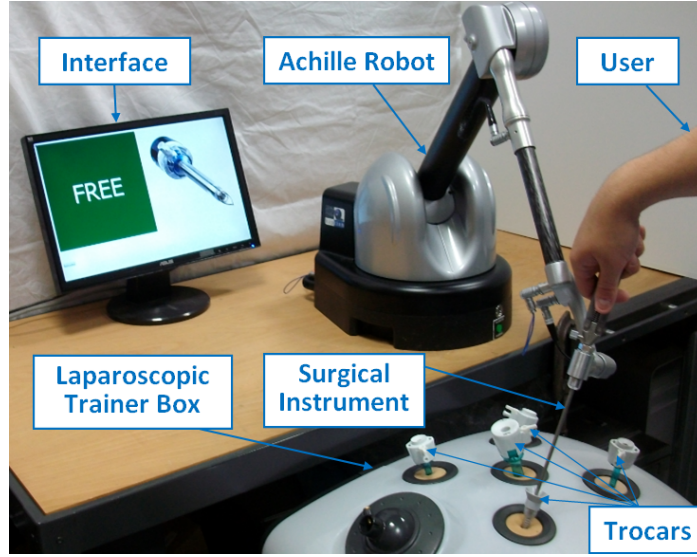


Fig. 2.12 Trocar detection and localization experiment setup.

2.4.4 Experimental validation

In-vitro experiments

In vitro experiments for trocar detection and localization were performed with Achilles in lab to verify the effectiveness of the proposed solution. Figure 2.12 is a photograph of the experimental setup.

A screen interface displays the trocar status as well as the current mode of Achilles (Free or Locked). During the trocar detection experiment, the system is always in Free mode.

We use a laparoscopic trainer box to simulate a patient's abdomen where four trocars are attached. The user inserts the instrument into four trocars one by one and manipulates the instrument simultaneously with the Achilles robot. For each trocar, the algorithm records the calculated trocar positions as well as the time when trocar status changes, *i.e.*, from not detected to detected, and vice-versa.

Thresholds for trocar detection are experimentally tuned as follows:

- Length of the large data list L_n : $n = 100$.
- Length of the small sublist L_m : $m = 20$.
- Thresholds for inclusion into a data list: $\delta_d = 0.005$ m and $\delta_\theta = 5^\circ$.
- Thresholds for trocar insertion detection: $\delta_{e_m} = 0.009$ m and $\delta_{\text{depth}} = 0.05$ m.

Table 2.3 Experimental results of robustness verification for trocar detection

	Insertion	Extraction	Total
Video	108	108	216
Robot	108	108	216
Success Rate	100%	100%	100%

Table 2.4 Experimental results of rapidness verification for trocar detection

Delay (s)	Insertion	Extraction
Max	4.3	1.4
Min	1.1	0.17
Mean	1.9	0.79
Standard Deviation	0.54	0.29

- Thresholds for trocar extraction detection: $\Delta_{e_m} = \Delta_{e_n} = 0.025$ m.

Firstly, robustness and rapidness of the algorithm are evaluated. The instrument is inserted in and extracted out of the four trocars in a random order. The time duration of keeping instrument inserted into one trocar is about 10 seconds while the time outside of a trocar lasts about 2 seconds. The total experiment lasts 23 minutes, and involves 108 insertion-extraction cycles. A camera is used to record the whole process.

We can visually observe on the video the time when the instrument is inserted in or extracted out of trocars and manually time stamp these events (with a precision of one frame, *i.e.* 25 ms). Using these time stamps as a ground truth, we can measure, from the robot data recorded and synchronized with the video, the delay between the real insertion (resp. extraction) and the detected trocar insertion (resp. extraction). In Table. 2.3, we see that all the insertions and extractions are correctly detected, which assesses the robustness of the proposed solution. In Table. 2.4, the statistics for the measured delays are reported. This delay is due to the necessary time for the algorithm execution. The average time delay for insertion and extraction are 1.9 s and 0.79 s respectively, with corresponding standard deviations 0.54 s and 0.29 s. At the scale of a surgical procedure, this rapidness can be viewed as acceptable.

The next step is to assess the precision of the method. Unfortunately, there is no known ground truth for a real trocar position. First, backlash appears between the trocar and the instrument. Second, the deformations of the simulated tissue as well as those of the instrument introduce trocar position deviations. For these reasons, rather than verifying the algorithm precision, which is formally impossible, we verify its numerical consistency. A

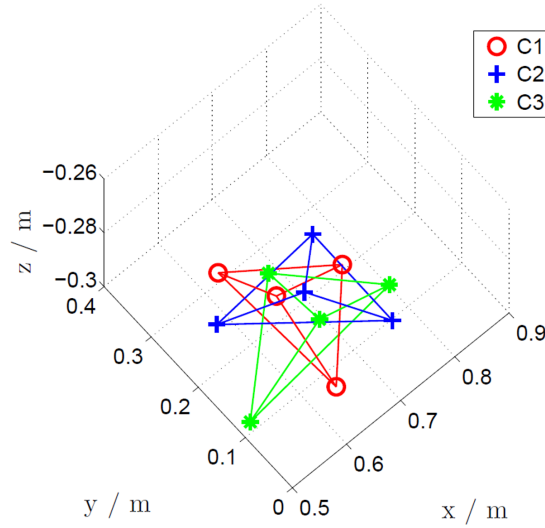


Fig. 2.13 Central positions of all trocars in 3D view for the lab experiments.

second experiment is designed, where the relative position of the trainer box with respect to the robot base changes. A given robot-trainer box relative position and orientation is called a configuration. In this experiment, we used three different configurations, represented by C_1 , C_2 and C_3 , respectively. Three sets of data recording estimated trocar positions are collected.

Using k-means clustering method, for each configuration we can identify four groups of points and their corresponding centroids, depicted in Fig. 2.13. Centroids of trocars obtained from C_1 are illustrated in red circles, C_2 in blue crosses and C_3 in green stars. The centroids of clustered point clouds are used as the mean detected trocar positions.

Since the relative positional relationship of the four trocars in space is independent of their relative positions to the robot, for the above three configurations, by some computation, we should obtain fixed trocar internal distribution information. More specifically, the calculated distance between a given trocar T_m and another trocar T_n , denoted as $\|\mathbf{d}_{T_m T_n}\|$, is supposed to be theoretically the same for C_1 , C_2 and C_3 . Table. 2.5 gives all the distances between any two trocars for the three configurations. The average distance of the three configurations and standard deviations are also shown.

We observe that distances between any two trocar centroids for the three configurations exhibit low standard deviations (typically 1 mm), indirectly assessing the numerical consistency of the proposed algorithm and its “precision”.

This is visually illustrated in Fig. 2.14 and Fig. 2.15. To obtain these plots, we performed a rigid transformation for data sets of C_1 and C_3 to align them with data set of C_2 . After the rigid transformation, it is observed that the centroids of the four trocars under three

Table 2.5 Distances between trocar centroids in the lab experiments

	C_1	C_2	C_3	Mean	std
$\ \mathbf{d}_{T_1T_2}\ (\text{m})$	0.1719	0.1710	0.1701	0.1710	9.0×10^{-4}
$\ \mathbf{d}_{T_1T_3}\ (\text{m})$	0.2430	0.2453	0.2460	0.2448	1.6×10^{-3}
$\ \mathbf{d}_{T_1T_4}\ (\text{m})$	0.1221	0.1229	0.1212	0.1221	8.5×10^{-4}
$\ \mathbf{d}_{T_2T_3}\ (\text{m})$	0.1733	0.1742	0.1734	0.1736	4.9×10^{-4}
$\ \mathbf{d}_{T_2T_4}\ (\text{m})$	0.1244	0.1234	0.1245	0.1241	6.1×10^{-4}
$\ \mathbf{d}_{T_3T_4}\ (\text{m})$	0.1222	0.1235	0.1229	0.1229	6.5×10^{-4}

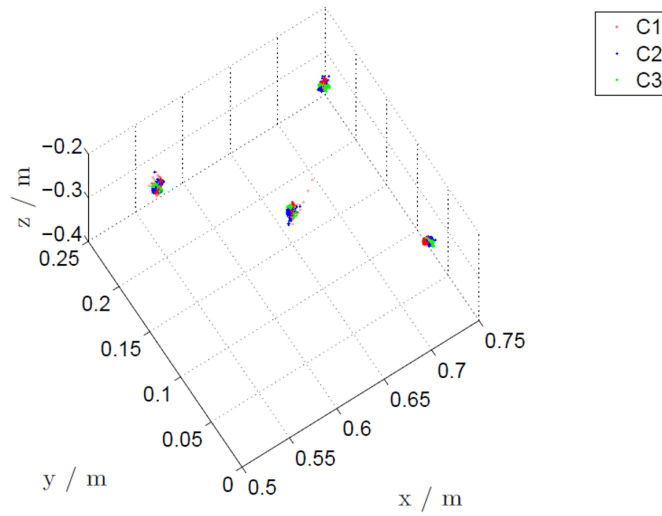


Fig. 2.14 Experimentally obtained trocar positions in 3D view after transformation for the lab experiments.

configurations closely coincide, indicating that the relative positional structure obtained from different configurations is consistent.

In-vivo experiments

In vivo experiments with a living pig have been conducted at Institut Mutualiste Montsouris in Paris. The experiment obtained the agreement from the local ethical committee. The purpose of the experiment was to verify the robustness of the proposed detection and localization algorithm under real conditions. A major difference lies in the fact that the so-called fulcrum point is less still in the OR than during a dry lab experiment. This is due to both skin flexibility (and forces applied on the fulcrum by the surgeon when performing surgery), breathing, and possible changes in insufflation conditions.

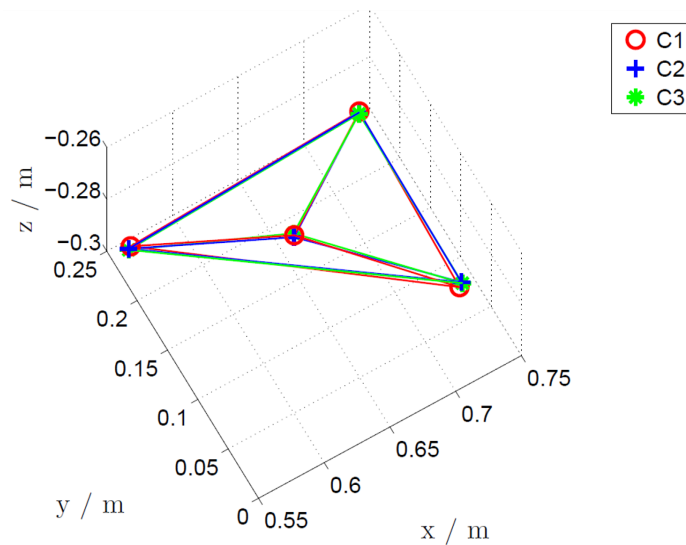


Fig. 2.15 Central positions of all trocars in 3D view after transformation for the lab experiments.

The surgeon performed a wide variety of surgical gestures by comanipulating the instrument together with Achilles, as seen in Fig. 2.16.

Three instrument trocars were installed on the pig's abdomen, at locations allowing the reach of most anatomical sites. These three trocars were different in both size and type. During the experiment, the surgeon used two different instruments: one was a traditional rigid laparoscopic surgical forceps, and the other was a robotic articulated instrument named JAiMY, manufactured by Endocontrol, France.

Meanwhile, during the experiment, Achilles was installed on a table connected to the surgical bed. Two different configurations C_1 and C_2 were chosen during the procedure, corresponding to two different locations of Achilles' base with respect to the pig.

The data for configuration C_1 was collected when the standard forceps was used while the data for configuration C_2 was recorded when JAiMY served as the tool. Original data together with their centroids which are obtained through k-means clustering method are displayed in Fig. 2.17, with small blue circles and green squares representing data of C_1 and C_2 , respectively, red dots and black solid squares representing centroids for C_1 and C_2 .

In Fig. 2.17, we observe that the data collected from the in vivo experiments are dispersed, compared with data from in vitro experiments shown in Fig. 2.14. This was indeed expected, as fulcrum movements do occur. It shall be noticed that, in order to challenge the detection algorithm, the surgeon was trying to access regions of the abdomen that were far from each

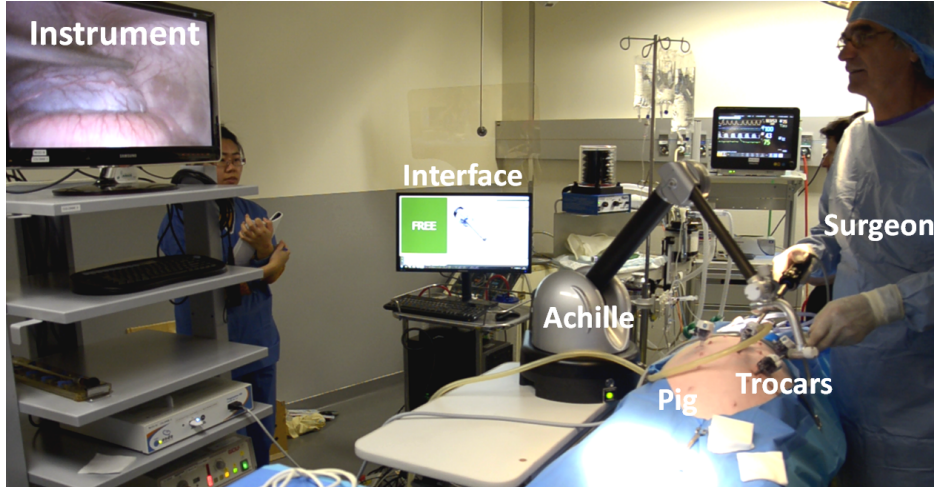


Fig. 2.16 Pig experiment scenario.

Table 2.6 Distances and angles between trocar centroids in the animal experiment

	C_1	C_2	Mean	std
$\ \mathbf{d}_{T_1T_2}\ (\text{m})$	0.1605	0.1746	0.1676	4.2×10^{-3}
$\ \mathbf{d}_{T_1T_3}\ (\text{m})$	0.1577	0.1517	0.1547	1.0×10^{-2}
$\ \mathbf{d}_{T_2T_3}\ (\text{m})$	0.1753	0.1748	0.1750	3.5×10^{-4}
$\widehat{T_2T_1T_3}(\text{rad})$	1.1669	1.1227	1.1448	3.1×10^{-2}
$\widehat{T_1T_2T_3}(\text{rad})$	0.9740	0.8981	0.9360	5.4×10^{-2}
$\widehat{T_1T_3T_2}(\text{rad})$	1.0007	1.1208	1.0608	8.5×10^{-2}

other, some of them requiring large torsion of the trocar with significant forces applied at the fulcrum.

A first remarkable result is that the detection function was not affected by these conditions: as for the dry lab experiment, 100% insertions and 100% extractions were appropriately detected, with similar response times. Further, due to the capacity of the algorithm to compute the trocar location in real time, the trocar was not “lost” when the surgeon was deforming on purpose the fulcrum. Rather, the estimated trocar position was smoothly adapted by the algorithm, without outliers in terms of extraction detection.

As for the dry lab experiments, there was no ground truth in the OR to compare with the estimated trocar localization. Instead, we compare the results obtained with C_1 and C_2 by computing a transform between them that should emphasize a constant trocar relative distribution. More precisely, in this experiment, for each configuration the three trocars constitute a triangle. An ideal result would give two congruent triangles, namely, C_1 and

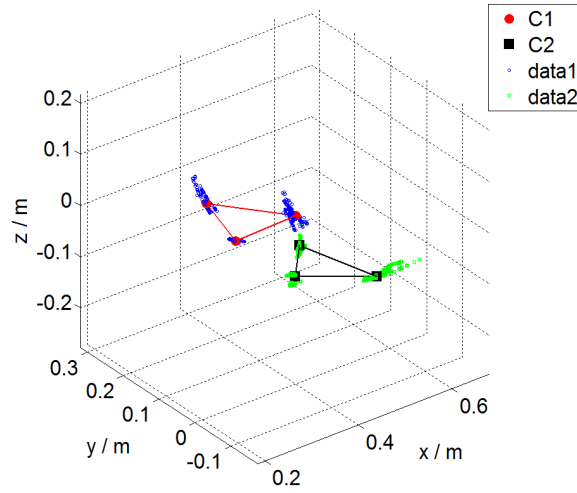


Fig. 2.17 Experimentally obtained trocar positions and centroids before transformation for the pig experiments.

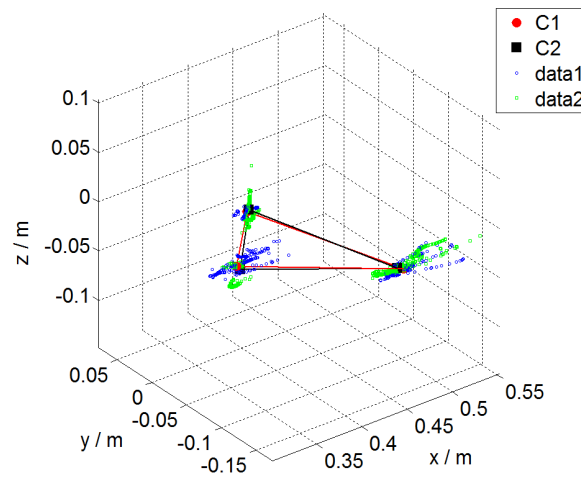


Fig. 2.18 Trocar positions and centroids after transformation for the pig experiments.

C_2 with equal trocar distances. The angle, constituted by three trocars T_u , T_v and T_w with trocar T_v as the apex, denoted as $\widehat{T_u T_v T_w}$, should be equal as well. Table 2.6 lists all the distances and angles of the two triangles obtained from these two configurations as well as their averages and standard deviations.

Figure 2.18 illustrates the results, where a rigid transformation is applied to data sets of C_1 to align with data set of C_2 . Both the numerical results and the plots exhibit consistency of the two configurations (distances between corresponding trocars in two configurations: 0.0078 m, 0.0076 m, 0.0054 m), proving the consistency of the results.

2.5 Conclusions

The physical characteristics of comanipulator Achilles is first depicted in terms of its mechanical design, kinematic calculation and actuation. Gravity compensation for the surgical instrument is a basic function to assist surgeons by improving ergonomics. Its implementation is described in theory and verified experimentally.

A major concern in deploying robotic assistance tools in the OR is to minimize the time requirement for installing the system. In this chapter, we addressed this concern by proposing a real-time trocar detection and localization for robotic-assisted surgery. The proposed solution is based on the least square principle. The practical implementation is realized and validated by experiments, both in vitro and in vivo, whose results show practical efficiency of the method. Results can be summarized as follows:

- There is no need for fastidious registration prior to the operation, which saves time.
- There is no need of external sensors.
- The movement of the patient or the robot during the operation is allowed thanks to the algorithm robustness and its forgetting capabilities.
- The algorithm is not influenced by patient breath or changes in insufflation conditions.
- Change of trocars during the operation is allowed without new registration.
- The algorithm exhibits numerical stability, precision, robustness and rapidness.

Chapter 3

Variable viscosity control

3.1 Introduction

A useful function that a robot can bring when comanipulating an object with a human operator is damping. To this aim, the robot may simply be programmed to exhibit viscosity. In a number of comanipulation applications, the viscosity shall vary during operation.

An existing approach consists in programming a high viscosity at low velocities (*e.g.*, to filter tremor during fine movements) and a low viscosity at high velocities (*e.g.*, to limit the amount of resistive force during large movements). In this chapter, this approach is shown to potentially degrade human's natural motion performance. This degradation is due to the viscosity drop when the subject accelerates, resulting in a sudden reduction of the robot resistance to motion.

To cope with this problem, a new approach is proposed to achieve the desired behavior in a stable manner. It consists in slowing down the viscosity variations thanks to a first order linear filter. The method is experimentally verified to be effective.

3.2 Variable viscosity control

3.2.1 Basic control law

In Chapter. 2, we described that Achilles can be controlled to exert a pure force $\mathbf{f} \in \mathbb{R}^3$ at its wrist point P . Meanwhile, position $\mathbf{x} \in \mathbb{R}^3$ and velocity $\mathbf{v} \in \mathbb{R}^3$ of point P can be measured through the robot sensors. With such a comanipulator, programming a viscosity is achieved by the following controller:

$$\mathbf{f} = -b\mathbf{v} . \tag{3.1}$$

We propose to make the viscosity $b \in \mathbb{R}$ depending on the norm of the velocity:

$$b = b_{max} \cdot \lambda (\|\mathbf{v}\|) , \quad (3.2)$$

where b_{max} is the maximal value of the viscosity and $0 \leq \lambda \leq 1$. More precisely, as proposed in [56], two thresholds, v_{min} and v_{max} are defined, with $0 < v_{min} < v_{max}$, and λ is computed by linear interpolation between its maximal value 1 and its minimal value b_{min}/b_{max} :

$$\lambda = \begin{cases} 1, & \text{if } \|\mathbf{v}\| < v_{min}, \\ \frac{b_{min}}{b_{max}}, & \text{if } \|\mathbf{v}\| > v_{max}, \\ 1 - \frac{\|\mathbf{v}\| - v_{min}}{v_{max} - v_{min}} \left(1 - \frac{b_{min}}{b_{max}}\right), & \text{otherwise.} \end{cases} \quad (3.3)$$

The variation of b with respect to $\|\mathbf{v}\|$ is illustrated in Fig. 3.1.

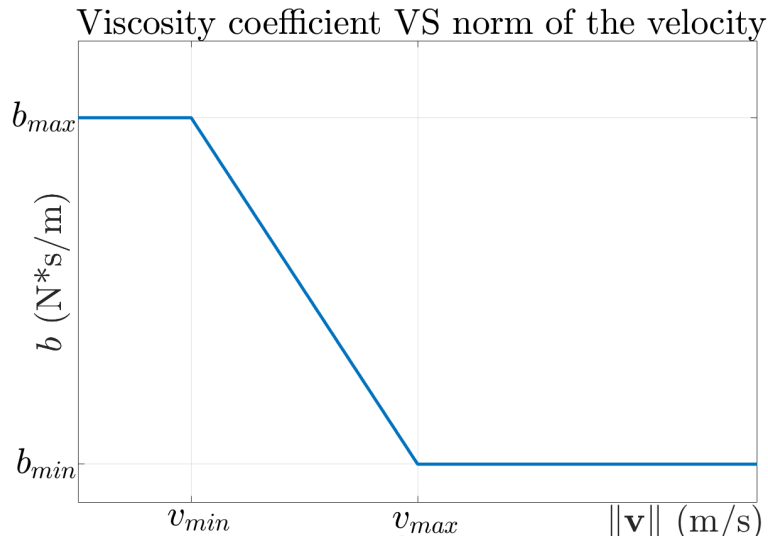


Fig. 3.1 Variation of the viscosity coefficient with respect to the norm of the velocity, as proposed in [56].

One major problem raised by this approach comes from the fact that, within a given range of velocities, the resistive force applied by the robot decreases as the velocity increases, as illustrated in Fig. 3.2. This can be compared to the Stribeck effect used, in tribology, to describe a drop in the friction force between the static regime and the dynamic regime. This phenomenon can be viewed as a local positive feedback and is known to create instability at low velocities, resulting in stick-slip motions [71]. By analogy, we can expect the system to exhibit instability when the user is trying to move the robot at a velocity that belongs to the region of negative slope (dashed curve in Fig. 3.2).

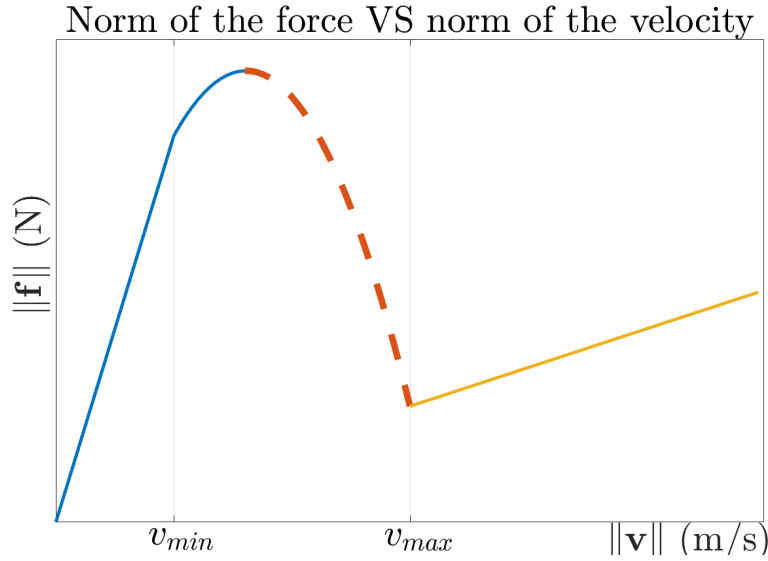


Fig. 3.2 Variation of the norm of the resistive force with respect to the norm of the velocity.

3.2.2 Theoretical analysis of instability

In order to study the stability problem from a theoretical point of view, we consider a simple control task. The comanipulator Achilles is connected to a 1 dof control robot at point P , which means that the motion of the former is guided by the latter. The task requires that the wrist point P of Achilles moves from a fixed starting point to a fixed ending point along a straight line at a constant velocity v_d under the guidance of the control robot. Fig. 3.3 is an illustration of the task.

The control law of Achilles is running according to Eq. (3.1), with b computed thanks to Eq. (3.2) and Eq. (3.3). Since the control robot aims to regulate the velocity of Achilles at the desired value, it can actually be considered to serve as a PI velocity controller. Furthermore, a feedforward force term is applied to the control robot in order to imitate human's ability of evaluating the amount of force required for achieving the desired velocity. Thus, the controller of the control robot writes:

$$f_c = f_d + k_p(v_d - v) + k_i \int (v_d - v) dt, \quad (3.4)$$

where f_c is the force produced by the control robot and f_d is the feedforward term. Assuming a good force prediction, one has:

$$f_d = b_d v_d, \quad (3.5)$$

where $b_d := b(v_d)$. If the end-effector of the 1 dof control robot is modeled as a pure mass m subject to both the Achilles robot force f and the control robot force f_c , the closed loop

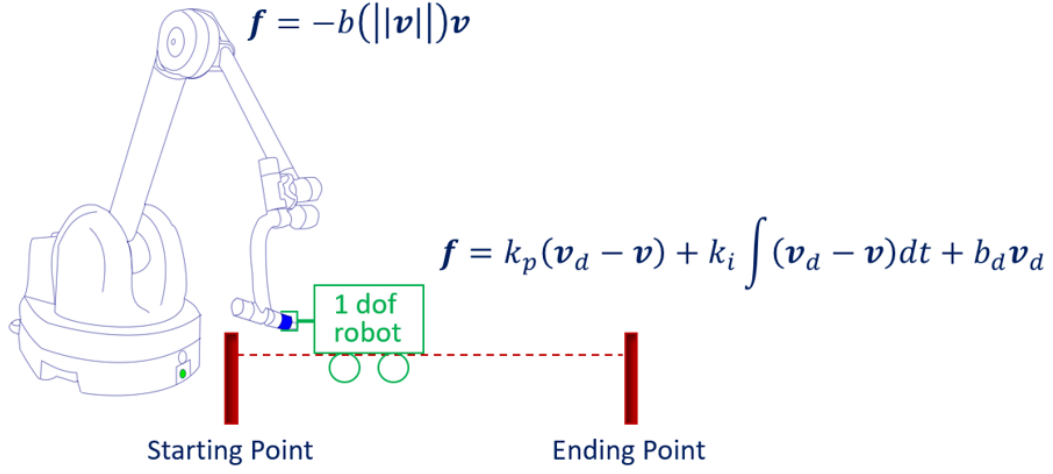


Fig. 3.3 Illustration of theoretical analysis of instability.

behavior then writes:

$$m\dot{v} = f + f_c = -bv + b_d v_d + k_p(v_d - v) + k_i \int (v_d - v)dt . \quad (3.6)$$

Eq. (3.6) can be rewritten as:

$$m\dot{v} = -v(b - b_d) - (b_d + k_p)(v - v_d) + k_i \int (v_d - v)dt . \quad (3.7)$$

For the sake of simplicity, we choose the system state variables as:

$$x_1 = \int (v_d - v)dt , \quad (3.8)$$

$$x_2 = v_d - v . \quad (3.9)$$

Their derivatives are consequently obtained as:

$$\dot{x}_1 = x_2 , \quad (3.10)$$

$$\dot{x}_2 = -\dot{v} . \quad (3.11)$$

According to Eq. (3.9), $v = v_d - x_2$. Eq. (3.7) becomes:

$$\dot{x}_2 = -\frac{k_i}{m}x_1 - \frac{k_p + b}{m}x_2 + \frac{bv_d - b_d v_d}{m} . \quad (3.12)$$

We now limit the study in the region where instability potentially occurs. Locally, b is an affine function of v : $b = b_0 - \alpha v$. Then Eq. (3.12) becomes:

$$\dot{x}_2 = -\frac{k_i}{m}x_1 - \frac{k_p + b_0 - 2\alpha v_d}{m}x_2 - \frac{\alpha}{m}x_2^2 - \frac{\alpha v_d^2 + b_d v_d - b_0 v_d}{m}. \quad (3.13)$$

Combining Eq. (3.8) ~Eq. (3.13), we can easily write the system state space equations:

$$\begin{pmatrix} \dot{x}_1 \\ \dot{x}_2 \end{pmatrix} = \begin{pmatrix} x_2 \\ -\frac{k_i}{m}x_1 - \frac{k_p + b_0 - 2\alpha v_d}{m}x_2 - \frac{\alpha}{m}x_2^2 - \frac{\alpha v_d^2 - b_0 v_d}{m} \end{pmatrix}. \quad (3.14)$$

Since the system model is nonlinear, we would like to do the Jacobian linearization around the equilibrium point.

$$\begin{pmatrix} \dot{x}_1 \\ \dot{x}_2 \end{pmatrix} = \underbrace{\begin{pmatrix} 0 & 1 \\ -\frac{k_i}{m} & -\frac{k_p + b_0 - 2\alpha v}{m} \end{pmatrix}}_{=: \mathbf{A}(v)} \begin{pmatrix} x_1 \\ x_2 \end{pmatrix}. \quad (3.15)$$

The reference velocity in the PI control is v_d , therefore, this system has a unique equilibrium point $(x_1, x_2) = (0, 0)$, around which the space equations linearize as:

$$\begin{pmatrix} \dot{x}_1 \\ \dot{x}_2 \end{pmatrix} = \underbrace{\begin{pmatrix} 0 & 1 \\ -\frac{k_i}{m} & -\frac{k_p + b_0 - 2\alpha v_d}{m} \end{pmatrix}}_{=: \mathbf{A}(v_d)} \begin{pmatrix} x_1 \\ x_2 \end{pmatrix}. \quad (3.16)$$

The eigenvalues of $\mathbf{A}(v_d)$ are $e_{1,2} = \left(-T \pm \sqrt{T^2 - 4k_i m}\right) / 2m$, with $T = k_p + b_0 - 2\alpha v_d$. Since $m > 0$, the real parts of the eigenvalues are both negative if and only if $\alpha < (b_0 + k_p) / (2v_d)$.

We therefore conclude that the system is locally asymptotically stable if $\alpha < (b_0 + k_p) / (2v_d)$, and if $\alpha > (b_0 + k_p) / (2v_d)$, the equilibrium is unstable. In other words, given a slope α for the viscosity drop, a desired velocity v_d , only a high stiffness k_p can stabilize the system.

3.2.3 Experimental evidence of instability

What is more interesting and meaningful is to use a human user to replace the 1 dof control robot for the theoretical analysis. However, it is much more complex to model a human controller. An oversimplified model would be imprecise and unconvincing. Therefore, instead of modeling, we performed experiments to evaluate the instability problem. An experimental setup was created as shown in Fig. 3.4.

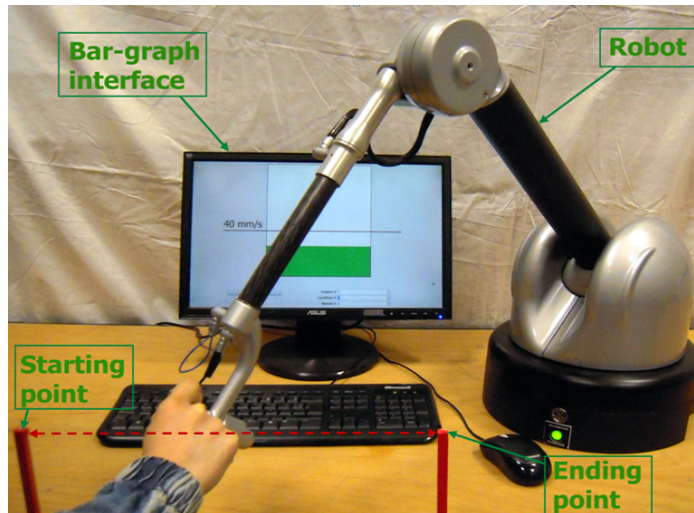


Fig. 3.4 A scene of the controller stability experiment.

The experimental task is basically the same as that described in Sec. 3.2.2, *i.e.*, guiding Achilles to move from the starting point to the ending point constantly and straightly as much as possible. A human user takes the place of the control robot to hold the wrist of Achilles. The magnitude of the given desired velocity v_d is 0.04 m/s. The distance between the starting point and the ending point materialized in the workspace is 0.4 m.

The user is instructed to roughly follow a straight line, without drastic constraint on trajectory precision following. Rather, s/he is asked to focus on the velocity. For this purpose, s/he is provided with a bar-graph interface depicted in Fig. 3.5. A gauge shows the current norm of the velocity, while a black line shows the desired value that the gauge should reach. During the experiment, the user is asked to maintain the bar-graph level to its desired value, which corresponds to a movement at v_d .

The comanipulator's control law is still running as given in Eq. (3.1), with a velocity-varying viscosity coefficient.

We designed three conditions of viscosity coefficient variations, with different functions $\lambda(\|\mathbf{v}\|)$. For Condition C_1 , $\lambda(\|\mathbf{v}\|)$ is designed in such a way that v_d fits within the high viscosity coefficient region. For Condition C_2 , $\lambda(\|\mathbf{v}\|)$ is designed in such a way that v_d fits within the viscosity coefficient drop region, leading to an intermediate viscosity coefficient. For Condition C_3 , $\lambda(\|\mathbf{v}\|)$ is designed in such a way that v_d fits within the low viscosity coefficient region. The three λ functions are represented in Fig. 3.6. The magnitude of the desired velocity, v_d , is the same for the three experiments. Note that the dropping slopes of the three conditions are the same.

Ten naive subjects, one female and nine males, aged from 22 to 45, have performed the experiment. All of them are right handed. They were presented conditions in a random order.

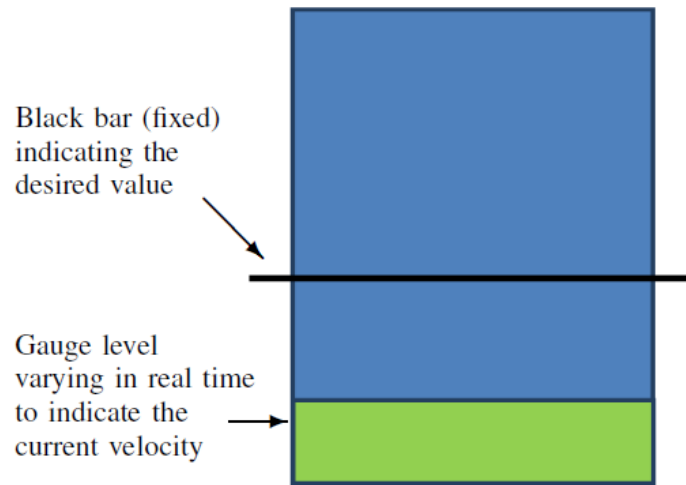


Fig. 3.5 Gauge providing a visual feedback to the user of the current velocity.

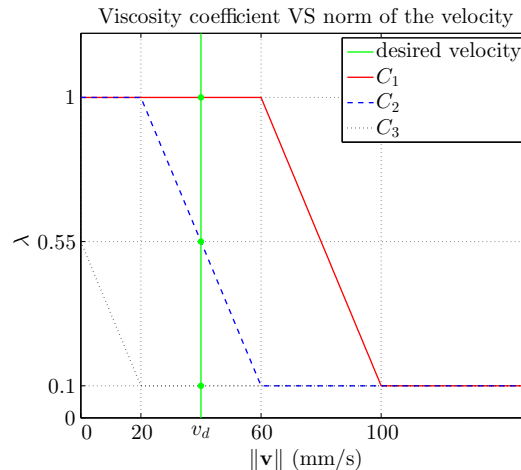


Fig. 3.6 Three designs of $\lambda(\|\mathbf{v}\|)$ used for the stability experiment.

For each condition, before recording the experiment, they were allowed to perform the task, back and forth, for a few times, in order to identify what is the level of force required to move the robot at v_d .

A typical experimental result is represented in Fig. 3.7 for a given subject. It can be clearly seen that for Conditions C_1 and C_3 , the subject can stabilize the velocity. Yet less error is observed for C_1 , due to the higher damping provided by a high viscosity coefficient. Most importantly, instability is observed under Condition C_2 : With an initial low velocity, corresponding to b_{max} , the subject accelerates in order to reach the desired velocity. However, due to the viscosity drop, the robot's resistance to motion decreases and the acceleration is higher than expected by the subject, resulting in a high velocity, corresponding to b_{min} . The subject then tries to slow down, but, as the viscosity increases, the deceleration is again

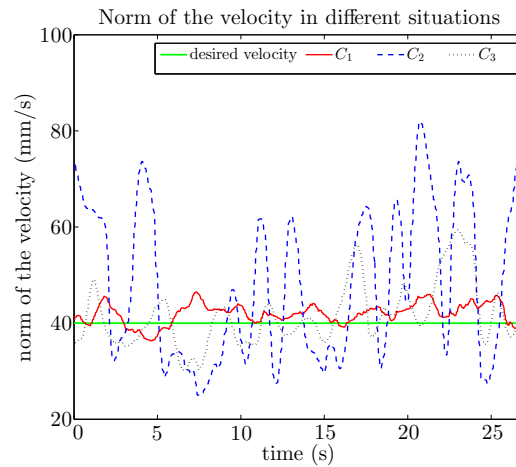


Fig. 3.7 Experimentally observed velocity for a given subject under Conditions $C_1 - C_3$.

higher than expected, resulting in the low velocity regime. Finally, the user oscillates between two limit regimes and is not able to stabilize the velocity at the desired value, similarly to stick-slip movements observed in [71].

This example behavior was observed with all subjects. Note that to compute the Root-mean-square (RMS) velocity error, only the middle part of the data was kept so as to prevent the effects of acceleration and deceleration happening when subjects start or stop the experiment. In Fig. 3.8, we present the RMS velocity errors together with their standard deviations recorded during the experiments, averaged across the 10 subjects, for the 3 conditions. The error of each subject is also shown in the figure as a small point to give more information. In order to quantitatively assess the comparative performance under these three conditions, a Student's t-test was performed to compare the RMS velocity errors under different conditions.

The average observed RMS error of C_3 is 4.7 mm/s ($\sigma = 0.94$ mm/s), which is roughly two times of the average error of C_1 ($\mu = 2.2$ mm/s, $\sigma = 0.57$ mm/s). The difference is statistically significant with a p-value of $p = 2.7 \times 10^{-6}$, much smaller than the general limit for statistical significant level 0.05. Meanwhile, the average RMS error of C_2 is 13 mm/s ($\sigma = 3.5$ mm/s), nearly three times of the average error of C_3 . The obtained p-value is $p = 4.0 \times 10^{-5}$, meaning that this difference of mean errors is also statistically significant. Therefore, we can conclude that the viscosity assists to the stability of the system while the dropping viscosity coefficient causes unstable performance.

The experimental results are in accordance with the theoretical conclusion. The system is unstable for the region with a large dropping viscosity coefficient. Subjects tended to increase

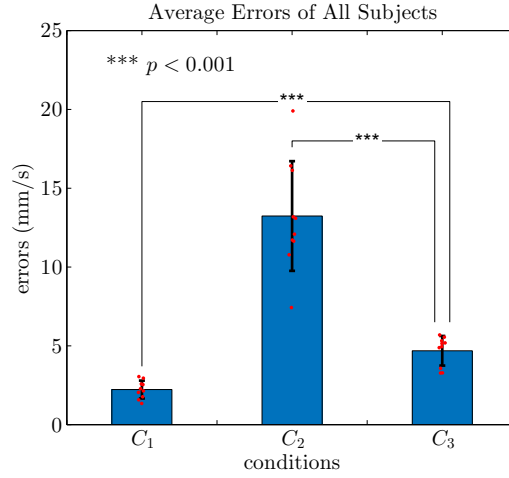


Fig. 3.8 Errors averaged across ten subjects under Conditions $C_1 - C_3$.

their arm stiffness in order to stabilize the system under Condition C_2 , but the performance was not satisfying.

3.3 Adding a dynamics to slow down viscosity variation

3.3.1 Viscosity control with filtered coefficient

In order to make the viscosity transition more smooth, we propose to apply a first order low pass filter to the viscosity coefficient. This *viscosity coefficient filter* is aimed at slowing down the variation of the viscosity coefficient, thus slowing down the viscous force changes so as to let the user have the time adapting to the force the robot applies. The control law now becomes:

$$\mathbf{f} = -b_f \mathbf{v}, \quad (3.17)$$

where b_f is the filtered viscosity coefficient defined by the following first order equation:

$$\dot{b}_f = (1/\tau) (b - b_f), \quad (3.18)$$

τ being the filter time constant in seconds.

3.3.2 Theoretical investigation of stability

For the theoretical investigation, we still employ the model built in Sec. 3.2.2. Now the system dynamics becomes:

$$m\dot{v} = -b_f v + b_d v_d + k_p (v_d - v) + k_i \int (v_d - v) dt . \quad (3.19)$$

Keeping x_1 and x_2 unchanged as in Eq. (3.8) and Eq. (3.9), we choose another state variable x_3 as:

$$x_3 = b_d - b_f . \quad (3.20)$$

Its derivative writes in the condition that b keeps as a function of v : $b_0 - \alpha v$

$$\begin{aligned} \dot{x}_3 &= -\dot{b}_f & (3.21) \\ &= \frac{1}{\tau} (b_f - b_0 + \alpha v) \\ &= \frac{1}{\tau} (b_f - b_0 + \alpha (v_d - x_2)) \\ &= -\frac{\alpha}{\tau} x_2 - \frac{1}{\tau} x_3 + \frac{\alpha v_d + b_d - b_0}{\tau} . \end{aligned} \quad (3.22)$$

The closed loop dynamics now writes:

$$m\dot{v} = -(b_d - x_3)(v_d - x_2) + k_p x_2 + k_i x_1 + b_d v_d , \quad (3.23)$$

which leads to the derivative of x_2 as:

$$\dot{x}_2 = -\dot{v} = -\frac{k_i}{m} x_1 - \frac{k_p + b_d}{m} x_2 - \frac{v_d}{m} x_3 + \frac{1}{m} x_2 x_3 . \quad (3.24)$$

Therefore, the combinations of Eq. (3.10), Eq. (3.22) and Eq. (3.24) gives the new state space equations:

$$\begin{pmatrix} \dot{x}_1 \\ \dot{x}_2 \\ \dot{x}_3 \end{pmatrix} = \begin{pmatrix} x_2 \\ -\frac{k_i}{m} x_1 - \frac{k_p + b_d}{m} x_2 - \frac{v_d}{m} x_3 + \frac{1}{m} x_2 x_3 \\ -\frac{\alpha}{\tau} x_2 - \frac{1}{\tau} x_3 + \frac{\alpha v_d + b_d - b_0}{\tau} \end{pmatrix} . \quad (3.25)$$

Likewise, we can write the Jacobian linearization around the equilibrium point:

$$\begin{pmatrix} \dot{x}_1 \\ \dot{x}_2 \\ \dot{x}_3 \end{pmatrix} = \underbrace{\begin{pmatrix} 0 & 1 & 0 \\ -\frac{k_i}{m} & -\frac{k_p+b_f}{m} & -\frac{v}{m} \\ 0 & -\frac{\alpha}{\tau} & -\frac{1}{\tau} \end{pmatrix}}_{=: \mathbf{B}(v)} \begin{pmatrix} x_1 \\ x_2 \\ x_3 \end{pmatrix}. \quad (3.26)$$

At the reference velocity of the PI control, the viscosity obtains its desired value. In other words, when $v = v_d$, we have $b_f = b_d$. Therefore, the equilibrium point of this system is $(x_1, x_2, x_3) = (0, 0, 0)$, around which the space equations linearize as:

$$\begin{pmatrix} \dot{x}_1 \\ \dot{x}_2 \\ \dot{x}_3 \end{pmatrix} = \underbrace{\begin{pmatrix} 0 & 1 & 0 \\ -\frac{k_i}{m} & -\frac{k_p+b_d}{m} & -\frac{v_d}{m} \\ 0 & -\alpha\omega & -\omega \end{pmatrix}}_{=: \mathbf{B}(\omega)} \begin{pmatrix} x_1 \\ x_2 \\ x_3 \end{pmatrix}. \quad (3.27)$$

where $\omega = 1/\tau$, is the frequency of the first order low pass filter.

The expression of the eigenvalues of $\mathbf{B}(\omega)$ is rather complex and does not fit in this paper format. However, our aim, in the next step, is to show that, whatever the value of the other (positive) parameters, there always exists a neighborhood around zero for ω where all the eigenvalues of $\mathbf{B}(\omega)$ have negative real parts. The characteristic polynomial of $\mathbf{B}(\omega)$ writes:

$$\kappa^3 + \left(\frac{b_d+k_p}{m} + \omega\right)\kappa^2 + \left(\frac{b_d+k_p - \alpha v_d}{m}\omega + \frac{k_i}{m}\right)\kappa + \frac{k_i}{m}\omega.$$

When $\omega = 0$, the roots to this polynomial are $\kappa_{1,2}(0) = -\frac{b_d+k_p}{2m} \pm \sqrt{\left(\frac{b_d+k_p}{2m}\right)^2 - \frac{k_i}{m}}$, which have negative real parts and $\kappa_3(0) = 0$.

Since the eigenvalues are continuous functions of the matrix coefficients, for $\omega > 0$ and small enough, $\kappa_{1,2}(\omega)$ are transformed into eigenvalues that also have negative real parts.

In this case, the third eigenvalue, $\kappa_3(\omega)$, is a real root of the characteristic polynomial, which can be written as:

$$\kappa^3 + a\kappa^2 + b\kappa + c.$$

For $\omega > 0$ and small enough, it is easy to verify that $a > 0, b > 0, c > 0$, since $\frac{b_d+k_p}{m} > 0$, and $\frac{k_i}{m} > 0$. A positive or zero value of κ can certainly not make this characteristic polynomial equal to zero. Therefore, the third eigenvalue is strictly negative.

Finally we can conclude that for $\omega > 0$ and small enough, all the eigenvalues of $\mathbf{B}(\omega)$ have a negative real part. In other words, whatever the tuning of the controller, for τ large

Table 3.1 The seven conditions for controller stability experiment

Conditions	High viscosity coefficient (stable region)	Medium viscosity coefficient (unstable region)	Low viscosity coefficient (stable region)
No filter ($\tau = 0$ s)	C_1	C_2	C_3
Filter ($\tau = 1$ s)	C_4	C_5	C_6
Filter ($\tau = 2$ s)	NA	C_7	NA

enough (leading to a change of b_f slow enough), the system becomes locally asymptotically stable.

3.3.3 Experimental evaluation of stability

Of course, because the model used for the theoretical analysis is simple, the stability condition cannot be used to practically tune the controller. However, we have performed experiments keeping unchanged the viscosity parameters used in Sec. 3.2.3, and adding a first order filter to the viscosity coefficient, with $\tau = 1$ s or $\tau = 2$ s depending on the experiments.

The experimental protocol is the same as the one described in Sec. 3.2.3. Namely, 4 new conditions have been added to $C_1 - C_3$. A first set of 3 conditions, $C_4 - C_6$ are the same as $C_1 - C_3$ with a viscosity filter and $\tau = 1$ s. Condition C_7 is the same as C_2 (the unstable configuration) with $\tau = 2$ s. This is summarized in Table. 3.1.

In order to compare with the performance exhibited in Fig. 3.7, we plotted in Fig. 3.9 the time variation of the velocity norm, for the same given subject, under Conditions $C_4 - C_7$. For C_4 and C_6 , we observe similar performance as for C_1 and C_3 , respectively. Most importantly, for both C_5 and C_7 , corresponding to an intermediate viscosity for which instability was observed under Condition C_2 , the subject is now able to stabilize the velocity at the desired value.

A similar behavior was observed in all the 10 naive subjects. In Fig. 3.10, the RMS velocity error averaged across the 10 subjects is plotted for $C_1 - C_7$ (the results for $C_1 - C_3$ being reproduced from Fig. 3.8 in order to ease comparison). To be clear, the conditions are grouped according to their viscosity regions.

The RMS velocity errors of C_1 ($\mu = 2.2$ mm/s, $\sigma = 0.57$ mm/s) and C_4 ($\mu = 2.2$ mm/s, $\sigma = 0.73$ mm/s) are quite close to each other. The performed Student's t-test on C_1 and C_4 gives a p-value of $p = 0.86$, meaning the difference of the average RMS errors between these two conditions is not statistically significant. A similar relationship can be observed between

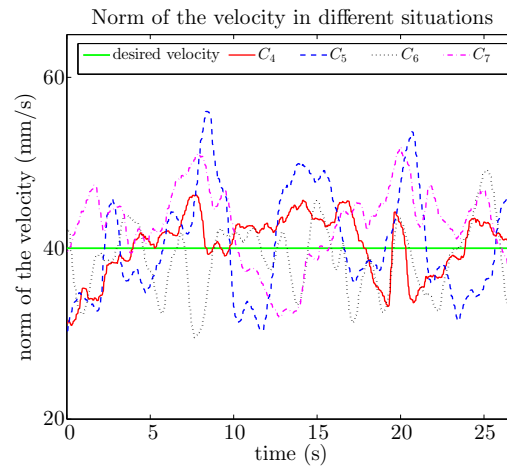


Fig. 3.9 Experimentally observed velocity for a given subject under conditions $C_4 - C_7$.

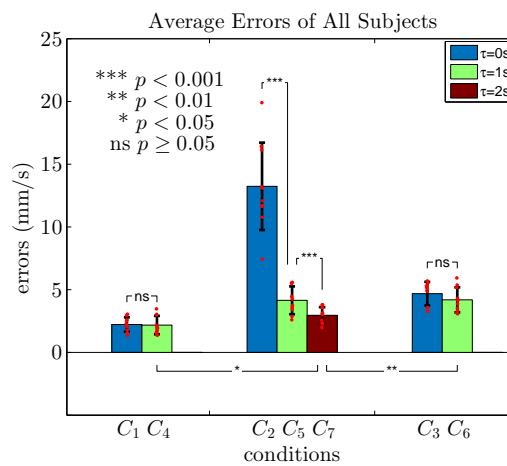


Fig. 3.10 Errors averaged across ten subjects under Conditions $C_1 - C_7$.

C_3 ($\mu = 4.7$ mm/s, $\sigma = 0.94$ mm/s) and C_6 ($\mu = 4.2$ mm/s, $\sigma = 1.0$ mm/s) with a p-value of $p = 0.25$. Thus we can draw the conclusion that adding a viscosity coefficient filter does not affect the performance of the original stable regions with high viscosity coefficient or with low viscosity coefficient.

As for C_2 ($\mu = 13$ mm/s, $\sigma = 3.5$ mm/s), C_5 ($\mu = 4.2$ mm/s, $\sigma = 1.1$ mm/s) and C_7 ($\mu = 3.0$ mm/s, $\sigma = 0.65$ mm/s), where the viscosity coefficient is intermediate and the filter time constants are $0s$, $1s$, $2s$, respectively, the RMS velocity errors drastically drops thanks to the added filter, making the original unstable behavior in the intermediate viscosity coefficient region become stable. The differences of C_2 and C_5 , C_5 and C_7 are both statistically significant with p-values of 9.5×10^{-6} and 5.2×10^{-4} , respectively, obtained from the Student's t-test. Furthermore, the error of C_7 being smaller than that of C_5 corresponds to the theoretical study in Sec. 3.3.2 that for τ large enough, the system becomes locally asymptotically stable.

In conclusion, adding a viscosity coefficient filter was experimentally found as an efficient way to prevent the instability for the medium viscosity coefficient drop region.

3.4 Point-to-point experiment

After the theoretical analysis as well as the experimental verification of the potential stability problem of the variable viscosity controller given a velocity based task for the subjects, a simple point-to-point movement experiment was carried out to further study the influence of viscous force on human's motion profile.

3.4.1 Materials and methods

Experiment setup

The experiment setup was implemented as shown in Fig. 3.11. We still use Achilles as the comanipulator. An instrument with a metal head is attached to the robot at the wrist point P . The control law of Achilles is running at the sampling interval of 1 ms according to Eq. (3.1), with b computed thanks to Eq. (3.2) and Eq. (3.3).

Four sticks (indicated as A, B, C and D in Fig. 3.11) are installed on a horizontal board, whose position with respect to the robot keeps unchanged during the experiment. At the top of each stick, there is a small metal chip connected to an Arduino Mega 2560 board. The touch of the instrument head and the stick chip triggers a signal which is sent to the computer for recording. At the side of each stick, a led is installed and connected to the Arduino board. Thus signals can be sent to control the illumination of all leds.

The heights of sticks A and C are both 55 mm, those of sticks B and D both 90 mm. The distances (measured from one chip to another) between AB, BC, AC and BD are 410 mm, 255 mm, 500 mm and 103 mm respectively. The heights and distances are chosen in such a way that all the movements of 6 joints of the robot are involved and the robot workspace is approximately covered.

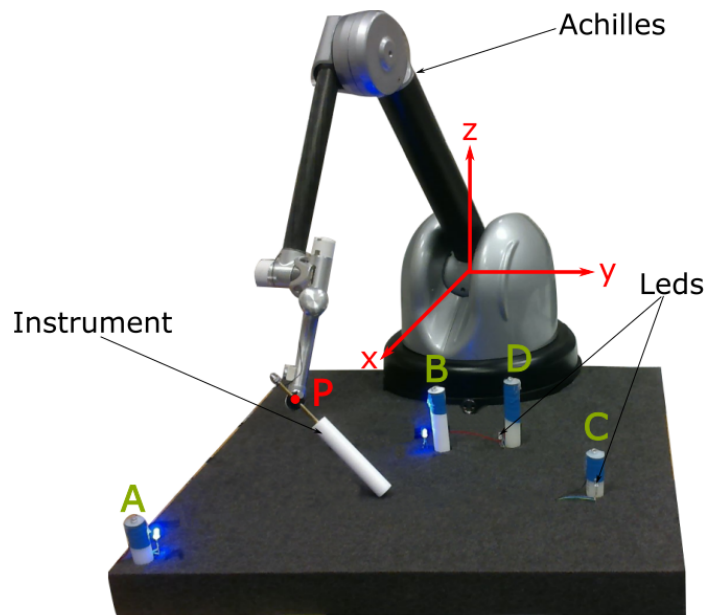


Fig. 3.11 The point-to-point movement experimental setup.

Experiment protocol

The whole experiment is divided into the following steps:

1. **Setting an initial posture.** The subject is instructed to choose a comfortable position which is a function of arm length. This position is marked by footmarks on the floor and fixed during the experiment.
2. **Calibration of viscosity curve.** The viscosity curve in Fig. 3.1 is determined by four parameters: b_{max} , b_{min} , v_{max} and v_{min} . b_{max} and b_{min} keep the same for all subjects while v_{max} and v_{min} are personalized. In order to obtain v_{max} , the viscosity b is first set as constant value b_{min} . The subject is instructed to do a point-to-point movement in a natural manner between the largest distance AC repeatedly. The peak velocities are collected and averaged, the average then multiplied by a ratio of 0.5 to get v_{max} . v_{min} is likewise obtained with b equal to b_{max} , the peak velocity collected and the average multiplied by 1.2 to get v_{min} . The ratios of 0.5 and 1.2 were determined by a prior

tuning experiment. Thus, the viscosity profile is created and will be applied for the rest of the experiment.

3. **Definition of controllers.** Five different controllers ($C_1 - C_5$, listed in Table. 3.2) are designed: C_1 with no viscosity, C_2 with maximum viscosity; $C_3 - C_5$ with variable viscosity where $b_{max} = 60 \text{ N} \cdot \text{s} \cdot \text{m}^{-1}$, $b_{min} = 0$, v_{max} and v_{min} are values saved in calibration step. C_3 has no filter. C_4 and C_5 have a viscosity filter with time constant 0.25s and 0.5s respectively.
4. **Tasks.** The subject is instructed to do point-to-point movements between different points. There are 4 trajectories: AB, AC, BC, BD. One trajectory is randomly picked by the computer and indicated by two enlightened leds. As presented in Fig. 3.11, the leds of points A and B are illuminated, indicating that the current trajectory is AB (or BA). After a trajectory is picked, one of the five controllers is randomly chosen. No additional constraint is imposed to subjects but doing natural movements.
5. **Recording.** We call a task the combination of one trajectory and one controller. Each task is repeated 5 times in the recording procedure (also in a random order). The pointing movements are recorded in a file at the sampling interval of 10 ms. Therefore, there are in total 100 records for each subject. Before recording, the subject is allowed to try as many times as needed until he/she thinks well practiced.
6. **Questionnaire.** The subject is finally asked to fill in a questionnaire on the experimental feelings. Basically, he/she needs to answer how many different situations felt and to describe which situation is the most difficult according to trajectory.

29 naive healthy subjects, 11 females and 18 males, aged from 22 to 49, 3 left-handed, have participated in the experiment. We discarded the data of subject 4 because this subject moved so slowly that the velocity never passed v_{min} , which is considered to have disobeyed the experimental protocol. We also removed some missed trials with irregular trajectories (*e.g.* if the subject was disturbed by surroundings). 40 bad files were deleted in total, accounting for 1.43% of all recorded files.

Performance indicators

According to the “minimal jerk hypothesis”, a widely accepted model in neuroscience, the human movement between pairs of targets is featured with a roughly straight hand trajectory together with a single-peaked, bell-shaped speed profile [54]. The bell curve is approximately symmetric about the peak velocity. Some research further reveals that when the final target

Table 3.2 The five controllers for point-to-point movement experiment

Conditions	No viscosity $b = 0$	Constant viscosity $b = 60 \text{ N} \cdot \text{s} \cdot \text{m}^{-1}$	Variable viscosity
No filter ($\tau = 0 \text{ s}$)	C_1	C_2	C_3
Filter ($\tau = 0.25 \text{ s}$)	NA	NA	C_4
Filter ($\tau = 0.5 \text{ s}$)	NA	NA	C_5

location is precisely controlled, the whole point-to-point movement can be decomposed into two phases: an approaching phase followed by a correction phase [72]. At the approaching phase, a transfer motion with gross displacement and low accuracy brings the hand close to the target [73]. The movement passes through an acceleration stage and then through a longer deceleration stage. In addition, the smooth bell shaped movement can be followed by the correction phase where the hand reaches the target. Fine corrective motions based on visual and proprioceptive feedback are added to adjust the position. Those corrective actions lead to irregularity and asymmetry of the shape of the speed profile by prolonging the deceleration stage [74].

In order to assess how different controllers affect the human natural motions, we abstract from the literature six indicators to quantitatively compare subjects' performance. These indicators, serving as the representative of gesture quality, are listed as follows:

- **PI_1 : Peak velocity.**

$$PI_1 = v_{max} , \quad (3.28)$$

where v_{max} is the maximum velocity reached during one point-to-point movement, corresponding to the peak of the bell curve.

- **PI_2 : Total task time.** It is the completion time of a single point-to-point task.

$$PI_2 = t_{end} - t_{init} , \quad (3.29)$$

where t_{init} and t_{end} are decided when the endpoint velocity is greater than 0.01 m/s.

- **PI_3 : Correction time ratio.** It is by definition the ratio between the correction time t_{corr} (a time interval from where 30% of peak velocity in the dropping region to where the task ends, illustrated in Fig. 3.12) and the total task time:

$$PI_3 = \frac{t_{corr}}{t_{end} - t_{init}} . \quad (3.30)$$

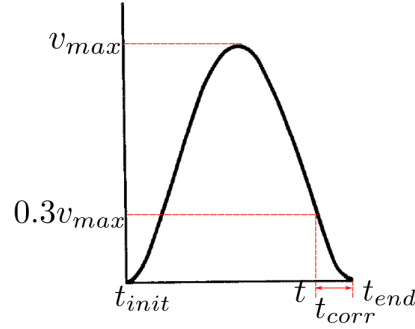


Fig. 3.12 Illustration of correction time.

- **PI_4 : Jerk.** The jerk metric is the average rate of change of acceleration during a movement and is a measurement of motion smoothness [75].

$$PI_4 = \frac{1}{t_{end} - t_{init}} \int_{t_{init}}^{t_{end}} \left[\left(\frac{d^3x}{dt^3} \right)^2 + \left(\frac{d^3y}{dt^3} \right)^2 + \left(\frac{d^3z}{dt^3} \right)^2 \right] dt, \quad (3.31)$$

where $[x, y, z]$ are the recorded endpoint coordinates. A large value means that the subject might have difficulty in guiding the robot.

- **PI_5 : Trajectory curvature.** It is defined as the maximum deflection of the path from a straight line joining the initial and final positions [75].

$$PI_5 = \frac{\max(d_p(t))}{\|\overrightarrow{P(t_{end})} - \overrightarrow{P(t_{init})}\|}, \quad (3.32)$$

where $d_p(t) = \frac{\|\overrightarrow{(P(t) - P(t_{init}))} \times \overrightarrow{(P(t_{end}) - P(t_{init}))}\|}{\|\overrightarrow{P(t_{end}) - P(t_{init})}\|}$ is the instantaneous distance of the vector position of pointer $\overrightarrow{P(t)}$ from the straight line joining $\overrightarrow{P(t_{init})}$ and $\overrightarrow{P(t_{end})}$. A large value indicates that the movement is greatly deviated from its natural path.

- **PI_6 : Energy.** It is the power integrated over time.

$$PI_6 = \int_{t_{init}}^{t_{end}} \mathbf{v} \cdot \mathbf{f} dt, \quad (3.33)$$

where \mathbf{v} and \mathbf{f} are velocity and force vectors recorded at the end-effector, respectively. A large value indicates that the subject needs to do more work for the same task.

To evaluate the influence of different controllers on the performance indicators, a two-way analysis of variance (ANOVA; groups: $C_1 - C_5$; blocks: AB, BC, AC, BD) with replication

is performed. The significance level is set as 0.05. Then Tukey's HSD post hoc test is conducted.

3.4.2 Experimental results

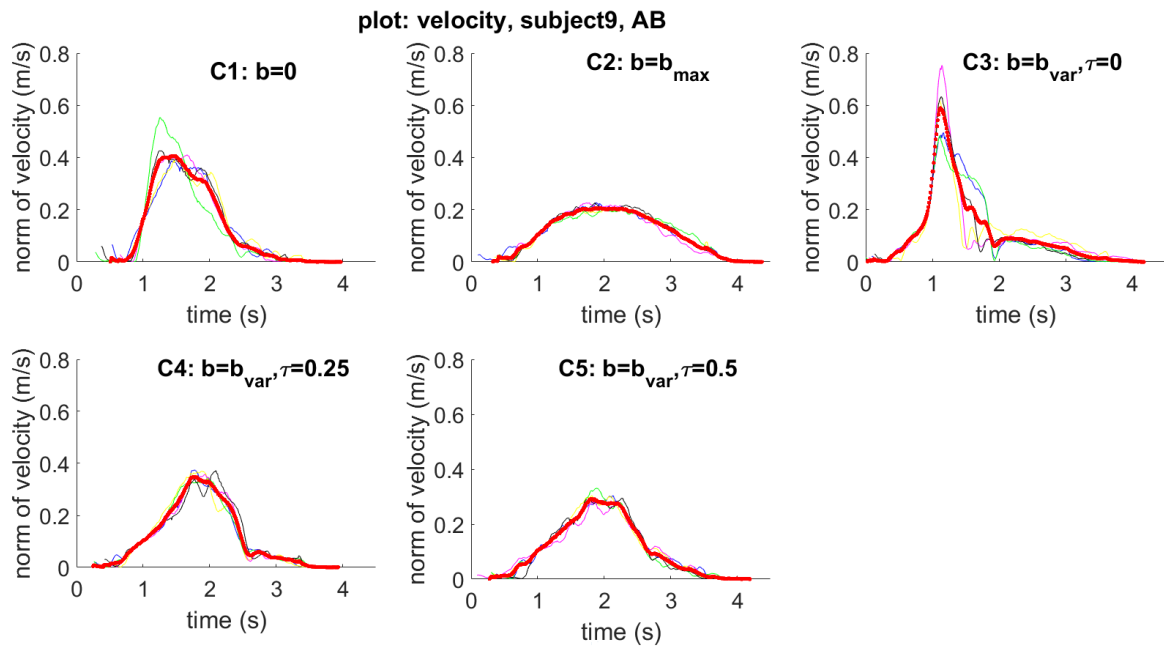


Fig. 3.13 A typical velocity profile of trajectory AB under controllers 1-5. Each thin curve represents an effective record. The thick red curves are averaged velocities of all effective records. Same representations for Fig. 3.14.

The velocity profiles obtained in a typical subject under the controllers $C_1 - C_5$ are displayed on Fig. 3.13 and Fig. 3.14 for a representative long segment AB and the short segment BD. For BD, the velocity is decreased by added viscosity, with similar profiles for the controllers $C_2 - C_5$ (consistently with the calibration adjusted so that the velocity remained below v_{min} to perform BD task). For AB, the constant viscosity controller (C_2) decreases the velocity while controller C_3 with rapidly variable viscosity induces an irregular velocity profile with a brisk higher peak followed by irregularities. The controllers C_4 and C_5 , with filtered viscosity dynamics, seem to induce slower but more regular and symmetric velocity profiles.

With controller C_1 , the peak velocity is approximately a linear function of movement distance as shown by Fig. 3.15 which displays the mean results in the group of subjects. The linear function of distance is modified with controller C_2 (slower slope or plateau) and with controller C_3 (faster variation with distance). The linear relationship with distance is

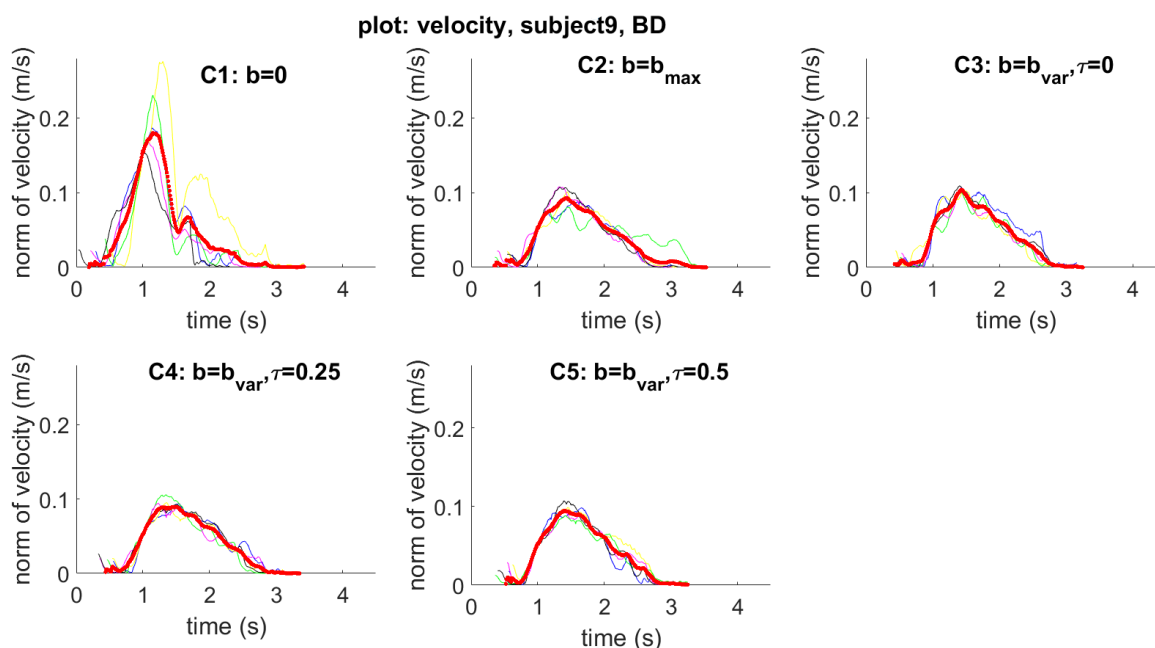


Fig. 3.14 A typical velocity profile of trajectory BD under controllers 1-5.

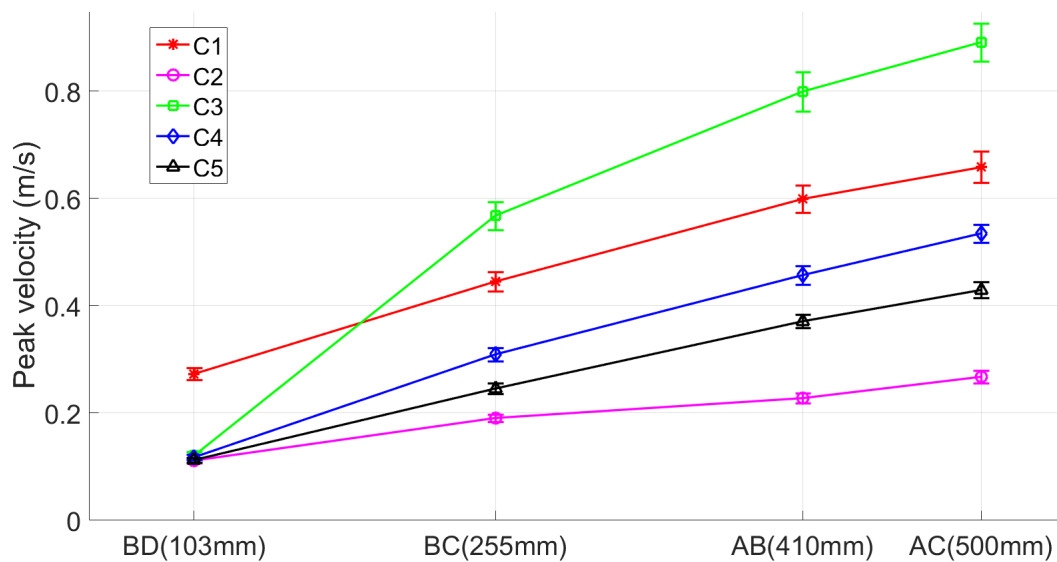


Fig. 3.15 Mean values and SEM of peak velocity of 28 subjects.

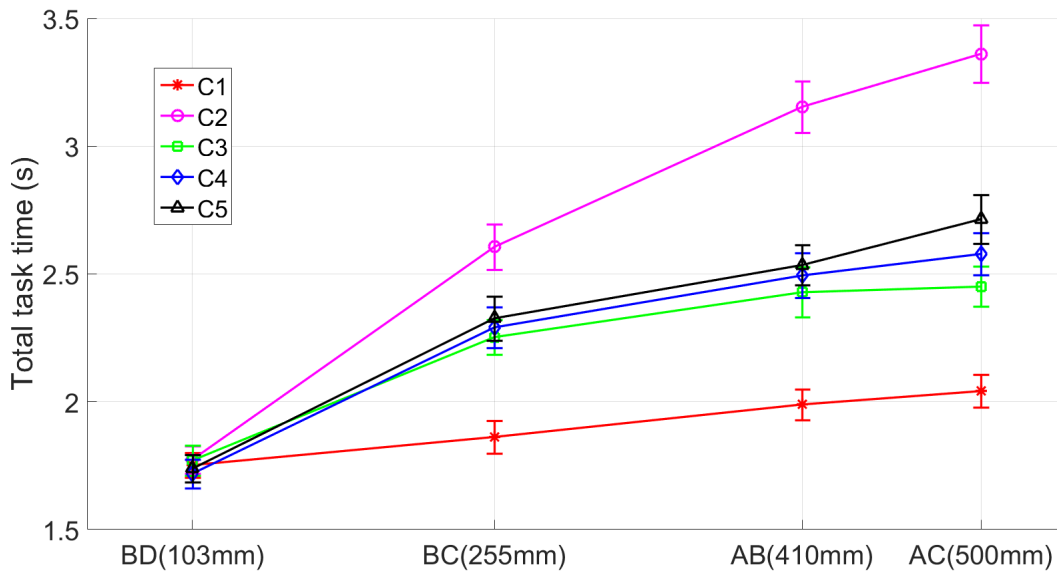


Fig. 3.16 Mean values and SEM of total task time of 28 subjects.

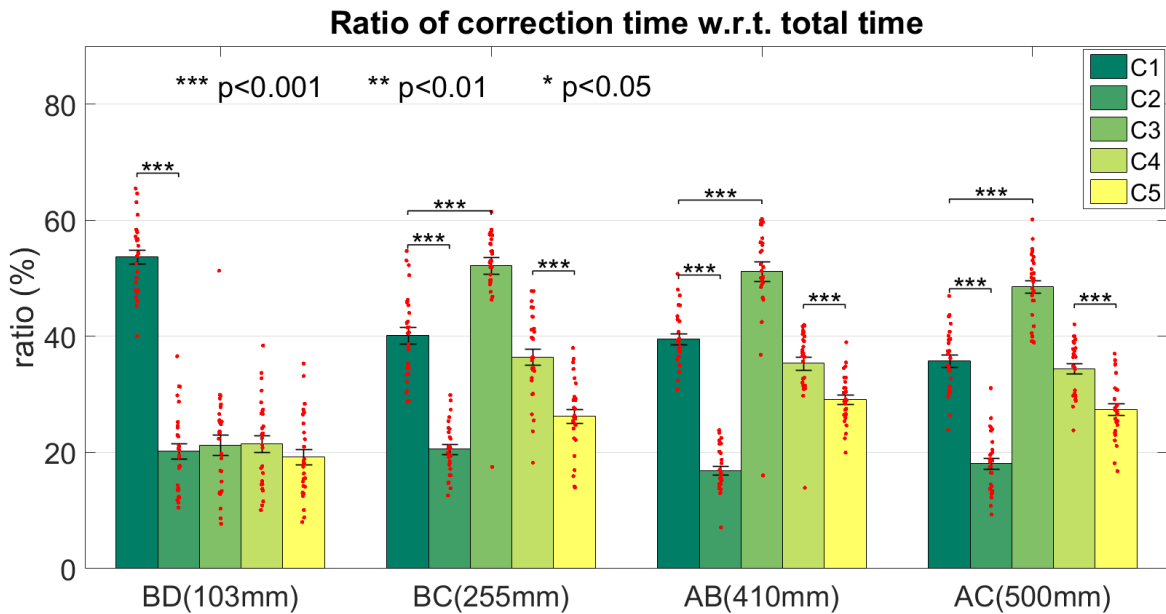


Fig. 3.17 Graph showing mean values of correction time ratio of 28 subjects, for all 4 trajectories under all 5 controllers. Error bars represent the standard error of the mean (SEM) with 95% confidence interval. Asterisks indicate significance level based on Tukey's HSD test between two controllers. Red dots on each bar represent mean correction time ratio of all effective records of one single subject. Sample size $N = 28$. Same representations for Fig. 3.18 - Fig. 4.10.

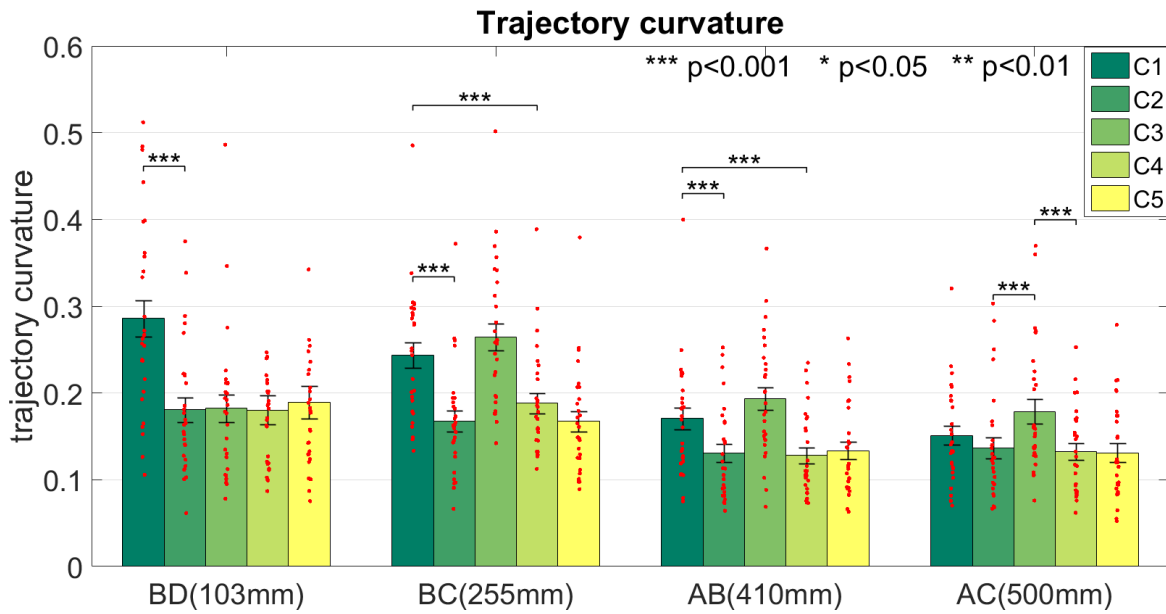


Fig. 3.18 Mean values and SEM of trajectory curvature of 28 subjects.

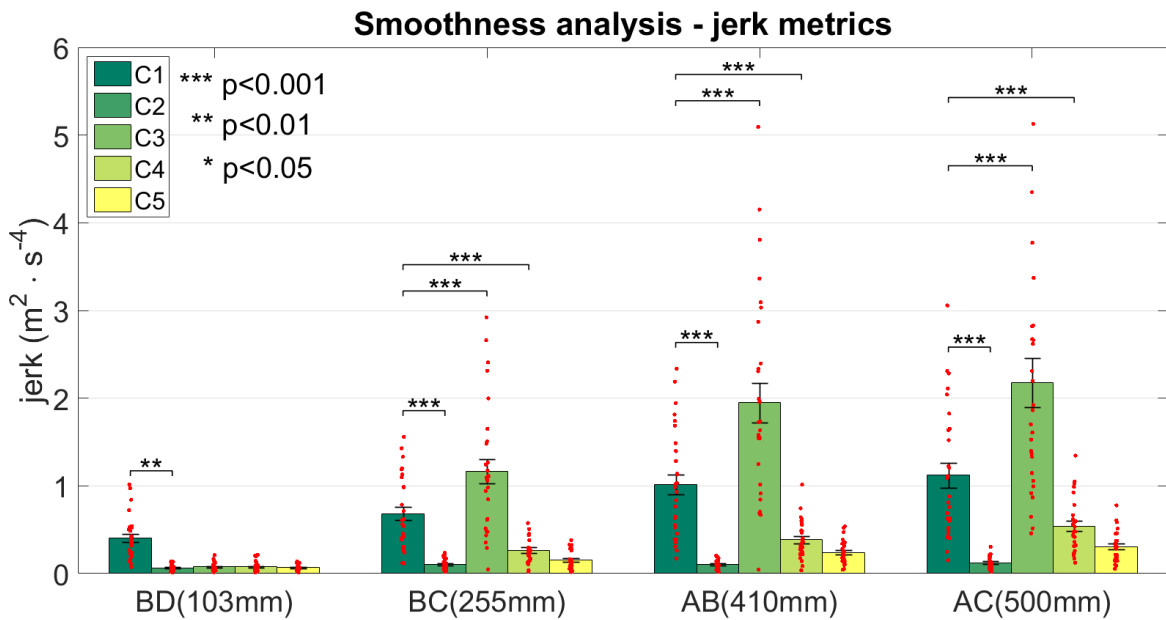


Fig. 3.19 Mean values and SEM of jerk metrics of 28 subjects.

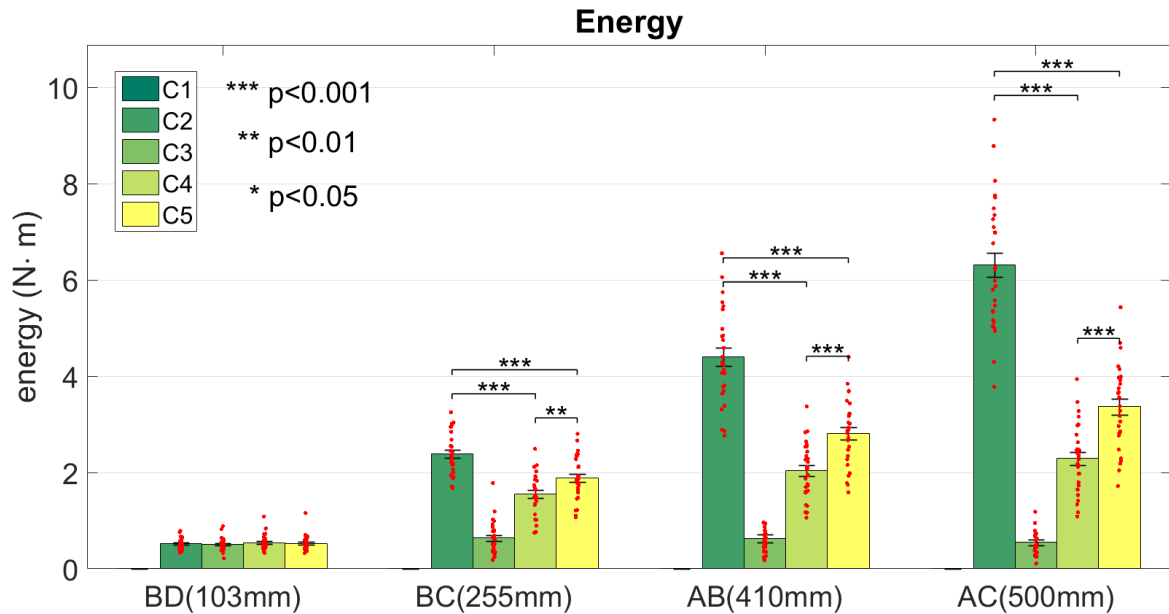


Fig. 3.20 Mean values and SEM of energy of 28 subjects.

restored for controllers C_4 and C_5 , with offset but relatively similar slopes. The total duration of the movements also increases with movement distance (Fig. 3.16). The duration is largely increased by a constant high viscosity (C_2) while the variable viscosity controllers ($C_3 - C_5$) show similar results with intermediate range of duration.

The increase in total duration is mainly due to an increase of correction time. The correction time ratio is significantly decreased by the added constant viscosity whatever the task, as seen by comparing C_1 and C_2 in Fig. 3.17. For the long segments AB-BC-AC controller C_3 increases significantly the ratio of correction time by reference to the null force controller (C_1) and to the controller with constant viscosity (C_2); the controllers with filtered viscosity ($C_4 - C_5$) being intermediary. The correction time is significantly shorter with C_5 . In contrast, for the task BD, the correction time ratio remains low for the controllers $C_2 - C_5$.

The trajectory curvature (Fig. 3.18) is decreased by the added viscosity (significant difference between C_1 and C_2 , except for task AC). For the long segments, the controller with rapidly variable viscosity (C_3) induces a higher curvature but the differences is not significant. The controllers with filtered viscosity variations ($C_4 - C_5$) reduce significantly the curvature of movements by reference to controller C_1 . For task BD, the curvature remains low in the $C_2 - C_5$ modes.

The added constant viscosity (C_2) decreases significantly the jerk metric by reference to the controller C_1 , showing that it induces smoother movements (Fig. 4.6). For the long segments, the jerk metric increases significantly with controller C_3 even above the control level. The modes with damped viscosity ($C_4 - C_5$) restore the smoothness of the movements,

with a jerk metric below the level of control. For BD segment, the jerk metric remains low in the modes $C_2 - C_5$.

For the long segments, the energy of the correction is particularly high with the constant viscosity mode C_2 and increases with the length of the segment. The mode with variable viscosity (C_3) significantly decreases the energy. The modes with damped viscosity ($C_4 - C_5$) give intermediate results, the mode C_5 consuming more energy than C_4 . For BD task, the energy is low whatever the control mode.

3.4.3 Discussion

For natural situation C_1 , the symmetry, reflected by the correction time ratio, decreases as a function of peak velocity. This observation is in accordance with the result presented in [76] that velocity curves at high speeds are more symmetric than at low speeds. The constant viscosity in C_2 decreases the time spent on the corrective movements and makes the velocity profile more symmetric. The increase of symmetry is also reported in [73] where the active assistance of the robot makes operator's speed profiles more symmetric than without robot during a point-to-point transportation of an object. Meanwhile, the less required movements for motion adjustment lead to much smaller jerk values. This can be explained as subjects have less difficulty in guiding the robot and thus have smoother motion. Moreover, the exerted viscosity also reduces the path deviation, diminishing the influence of robot friction and inertia.

Even though C_2 outperforms C_1 in terms of trajectory deflection, motion smoothness and correction time ratio, however, it constrains the efficiency by consuming more time due to the lowered velocity. Besides, the large energy consumption of C_2 tends to lead to fatigue. These constraints are mainly for long and medium trajectories while for short trajectory the viscous force does not significantly prolong the movement time.

From the above comparison, we conclude that a constant viscosity controller is appropriate for tasks with short distance. For large or medium trajectory, viscous force is beneficial to movement quality but decreases performance when it comes to energy. In reality, the viscosity is mainly preferred for the correction phase to easily and precisely reach the target. As for the approaching phase, the accuracy requirement is not strictly demanded, instead, fastness and easiness of the movement are the primary criteria. Therefore, the variable viscosity controller C_3 which generates no force for gross velocity is proposed. This strategy acts as C_2 for short distances when the velocity remains small, which is proven by the nearly identical experimental results of all indicators between C_2 and C_3 detected for BD.

Even though C_3 satisfies the requirements for both large and low velocities, it induces problems in the transition region, as analyzed in Sec. 3.2.1. The result that the average

peak velocity of C_3 largely exceeds the natural velocity of C_1 indicates that the user has the risk of losing control of the instrument, which is potentially dangerous for human-robot interaction. Besides, the symmetry is destroyed: the slopes of last part of acceleration and of first part of deceleration become steep, while the prolonged correction phase makes the whole deceleration phase much longer than the accelerative counterpart. This phenomenon is reflected by the large value of correction time ratio of C_3 .

C_4 and C_5 with a viscosity filter are thus proposed to slow down the variation of viscosity coefficient. Analysis shows that they can maintain the benefits of constant viscosity controller for short trajectory. As to the long or medium trajectory, the experimental results show that they have the ability to restore the bell curve symmetry. Unlike C_3 , the peak velocities of C_4 and C_5 never pass beyond the natural velocity, posing no risk of instability. Moreover, smaller values of trajectory curvature and jerk compared with C_1 means that subjects were less affected by the robot, and that the performance is closer to the natural movement path. The less energy consumption means that subjects do not need to do as much work as in C_2 , thus having less tendency to fatigue.

It is worth to point out that there is a trade-off for indicator performance when choosing filter time constant. A smaller one, *e.g.*, adopted by C_4 , has a better performance in terms of energy consumption. On the other hand, a larger one used in C_5 has a stronger capacity to adjust viscosity variation. Therefore, the choice of filter time constant depends on the real necessity.

The above analysis as well as the feedback of subjects in questionnaire give proofs to the following hypothesis: for large motions, the requirement of the ability to move rapidly and easily demands no force while for small motions, viscous force could serve to facilitate the stability and precision. A linear transition between small and large motions might drastically disturb users' controllability of the robot. Adding a first-order low pass filter can keep the benefits of both high precision and stability for fine motions and rapid response for large motions, yet at the same time, avoid the abrupt acceleration and deceleration.

3.5 Conclusions

This chapter concerns applications of comanipulation where the viscosity coefficient is designed to decrease as the velocity increases. An instability problem, that was yet unreported in the literature, was experimentally identified and theoretically shown using an illustrative model. A solution was proposed by including a secondary dynamics in the variations of the viscosity. A theoretical analysis supports this proposition, while experiments show its practical efficiency. The effect of this variable viscosity control on human's motion

performance was also experimentally identified through an experiment consisting of simple point-to-point movement tasks. The comparison of user performance between the filtered and unfiltered viscosity controller confirms the practical efficiency of the proposition.

Chapter 4

Lever model effect

4.1 Introduction

In laparoscopic surgery, the trocar and the instrument form a lever, with the entry point as its fulcrum. The motion of points lying on the instrument is under the constraint of a specific relationship, which is called the lever effect or the fulcrum effect. The movement of the tip of the instrument and that of the handle are inverses, and their amplitude ratio for the rotational motions depends on the insertion depth of the instrument into the trocar. Therefore, the involuntary physical hand tremor might be amplified, which would decrease surgeons' performance. In this chapter, Achilles is employed to serve as a comanipulator to provide viscous force on the instrument so as to filter out the hand tremor of the surgeon. This force is physically applied at the robot wrist point P as detailed in Chapter. 2. It can be computed to evaluate equivalent forces at any point of the instrument thanks to a lever model [39]. By using the lever model, the viscosity controller can be applied at different instrument points which might bring different outcomes.

4.2 Establishment of lever model

Consider M as an arbitrary point on the instrument axis, \mathbf{v}_M , its velocity and \mathbf{f}_M , a force exerted at M . A relationship of forces and of velocities between point M and the robot wrist point P could be established. The lever model allows to compute the \mathbf{v}_M and \mathbf{v}_P avoiding using noisy signals. Figure 4.1 is an illustration of the lever model when M is considered as the instrument tip point T .

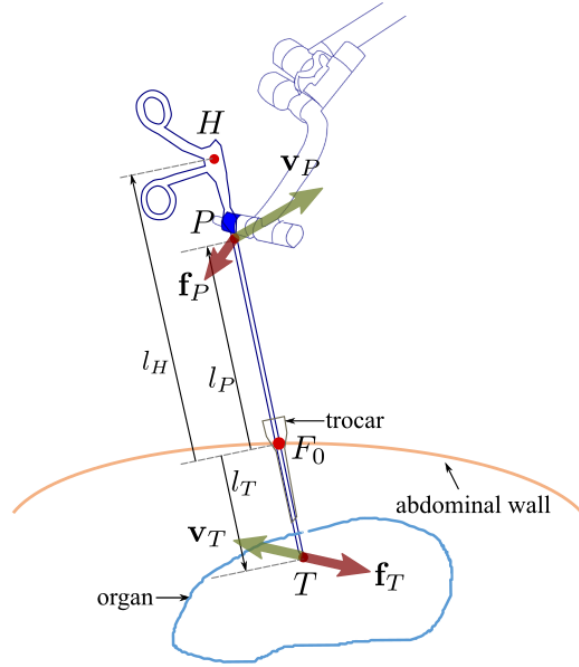


Fig. 4.1 Illustration of lever model.

4.2.1 Kinematic part

The entry point, denoted as F_0 , is supposed to be fixed in \mathcal{F}_0 . F is defined as a point that belongs to the instrument and instantaneously coincides with F_0 when the instrument passes through the trocar.

For any point M belonging to the instrument, represented by (F, \mathbf{z}_i) , we define a signed scalar l_M with:

$$\mathbf{d}_{FM} =: l_M \mathbf{z}_i . \quad (4.1)$$

Note that for a working configuration, the instrument being inserted into the patient's body, one has: $l_H > 0$, $l_P > 0$ and $l_T < 0$.

The presence of the trocar imposes a two-dof geometric constraint to the kinematic at point F . Therefore, for instrument movements inside the abdomen, the geometric constraint of only 4 dofs being allowed should be taken into consideration in the calculation of forward and inverse kinematics. In other words, equations have to be fulfilled at the entry point:

$$\mathbf{v}_{F,x} = 0, \mathbf{v}_{F,y} = 0 . \quad (4.2)$$

Therefore, \mathbf{v}_F only has the velocity along the instrument axis. We denote:

$$\left\{ \mathcal{T}_{I/0} \right\}_F = \left\{ \begin{array}{l} \mathbf{v}_F = v_z \mathbf{z}_I \\ \boldsymbol{\omega}_I = \omega_x \mathbf{x}_I + \omega_y \mathbf{y}_I + \omega_z \mathbf{z}_I \end{array} \right\}, \quad (4.3)$$

where v_z is the translational velocity of the instrument along \mathbf{z}_I ; ω_x , ω_y and ω_z are projections of the rotational velocity over \mathbf{x}_I , \mathbf{y}_I and \mathbf{z}_I , respectively. The velocity of a point M belonging to the instrument axis thus writes:

$$\begin{aligned} \mathbf{v}_M &= \mathbf{v}_F + \mathbf{d}_{MF} \times \boldsymbol{\omega}_I \\ &= v_z \mathbf{z}_I - l_M \mathbf{z}_I \times (\omega_x \mathbf{x}_I + \omega_y \mathbf{y}_I + \omega_z \mathbf{z}_I) \\ &= l_M \omega_y \mathbf{x}_I - l_M \omega_x \mathbf{y}_I + v_z \mathbf{z}_I. \end{aligned} \quad (4.4)$$

From Eq. (4.4) we can write the projection of \mathbf{v}_M along \mathbf{z}_I axis:

$$\mathbf{z}_I \mathbf{z}_I^T \mathbf{v}_M = v_z \mathbf{z}_I, \quad (4.5)$$

and the projection of \mathbf{v}_M into the plane perpendicular to \mathbf{z}_I axis:

$$(\mathbf{I} - \mathbf{z}_I \mathbf{z}_I^T) \mathbf{v}_M = l_M (\omega_y \mathbf{x}_I - \omega_x \mathbf{y}_I). \quad (4.6)$$

In particular, when $M \equiv P$,

$$\begin{aligned} \mathbf{z}_I \mathbf{z}_I^T \mathbf{v}_P &= v_z \mathbf{z}_I \\ (\mathbf{I} - \mathbf{z}_I \mathbf{z}_I^T) \mathbf{v}_P &= l_P (\omega_y \mathbf{x}_I - \omega_x \mathbf{y}_I). \end{aligned} \quad (4.7)$$

Combining Eq. (4.5), Eq. (4.6) and Eq. (4.7) we get the following relationship:

$$\begin{aligned} \mathbf{z}_I \mathbf{z}_I^T \mathbf{v}_M &= \mathbf{z}_I \mathbf{z}_I^T \mathbf{v}_P \\ (\mathbf{I} - \mathbf{z}_I \mathbf{z}_I^T) \mathbf{v}_M &= \alpha_M (\mathbf{I} - \mathbf{z}_I \mathbf{z}_I^T) \mathbf{v}_P, \quad \alpha_M := \frac{l_M}{l_P}. \end{aligned} \quad (4.8)$$

We rewrite \mathbf{v}_M as

$$\begin{aligned} \mathbf{v}_M &= (\mathbf{I} - \mathbf{z}_I \mathbf{z}_I^T) \mathbf{v}_M + \mathbf{z}_I \mathbf{z}_I^T \mathbf{v}_M \\ &= \alpha_M (\mathbf{I} - \mathbf{z}_I \mathbf{z}_I^T) \mathbf{v}_P + \mathbf{z}_I \mathbf{z}_I^T \mathbf{v}_P \\ &= [\alpha_M (\mathbf{I} - \mathbf{z}_I \mathbf{z}_I^T) + \mathbf{z}_I \mathbf{z}_I^T] \mathbf{v}_P. \end{aligned} \quad (4.9)$$

Therefore, one gets the final relationship between \mathbf{v}_M and \mathbf{v}_P :

$$\begin{aligned} \mathbf{v}_M &= \mathbf{L}(\alpha_M) \mathbf{v}_P, \quad \alpha_M = l_M/l_P, \\ \mathbf{L}(\alpha_M) &:= \alpha_M (\mathbf{I} - \mathbf{z}_I \mathbf{z}_I^T) + \mathbf{z}_I \mathbf{z}_I^T, \end{aligned} \quad (4.10)$$

where \mathbf{v}_P is the velocity of the robot wrist, which can be obtained from the robot sensors.

We call \mathbf{L} lever model matrix and α_M lever ratio, the computation of which will be presented in detail in Sec. 4.2.3. Note that $\mathbf{L} = \mathbf{L}^T$. This relationship allows computing the velocity of any point M belonging to the instrument axis from the velocity of point P , which can be measured in the robot base frame, without using the noisy measurement from the wrist sensors. Specially, projecting \mathbf{v}_M in instrument frame leads to:

$${}^I \mathbf{v}_M = {}^I \mathbf{L}(\alpha_M) {}^I \mathbf{v}_P, \quad {}^I \mathbf{L}(\alpha_M) = \begin{pmatrix} \alpha_M & 0 & 0 \\ 0 & \alpha_M & 0 \\ 0 & 0 & 1 \end{pmatrix}. \quad (4.11)$$

4.2.2 Dynamic part

From Eq. (4.10) we can obtain the velocity of any point on the instrument axis with \mathbf{v}_P given if the fulcrum location is known (l_M and l_P known). Dually, we now want to compute what pure force \mathbf{f}_P shall be applied by the robot at point P in order to be equivalent to an external wrench consisting in a pure force virtually applied at point M :

$$\{\mathcal{W}_{virt}\}_M = \left\{ \begin{array}{c} \mathbf{f}_{virt} \\ \mathbf{m}_{virtM} = \mathbf{0} \end{array} \right\}. \quad (4.12)$$

The robot wrench is expressed as:

$$\{\mathcal{W}\}_P = \left\{ \begin{array}{c} \mathbf{f}_P \\ \mathbf{m}_P = \mathbf{0} \end{array} \right\}. \quad (4.13)$$

The robot wrench and the virtual wrench defined by Eq. (4.12) are said to be equivalent iff:

$$\forall \mathbf{v}_P, \forall \boldsymbol{\omega}_I, \quad \mathbf{f}_P^T \mathbf{v}_P + \mathbf{0}^T \boldsymbol{\omega}_I = \mathbf{f}_{virt}^T \mathbf{v}_M + \mathbf{0}^T \boldsymbol{\omega}_I. \quad (4.14)$$

Therefore, exploiting the result from Eq. (4.10), we get:

$$\mathbf{f}_P = \mathbf{L}^T(\alpha_M) \mathbf{f}_{virt}. \quad (4.15)$$

Considering $\mathbf{L} = \mathbf{L}^T$, we finally have:

$$\mathbf{f}_P = \mathbf{L}(\alpha_M)\mathbf{f}_{\text{virt}}. \quad (4.16)$$

In the next, we will denote \mathbf{f}_M a punctual force applied at a point M without any moment at this point. With this convention, Eq. (4.16) writes:

$$\mathbf{f}_P = \mathbf{L}(\alpha_M)\mathbf{f}_M. \quad (4.17)$$

This last equation is the dual of Eq. (4.10). It can be used to compute the force \mathbf{f}_P applied by the robot at point P in order to produce a mechanical effect that is equivalent to a virtual force \mathbf{f}_M that would have been applied at point M .

4.2.3 The computation of lever model matrix

To compute \mathbf{v}_M from \mathbf{v}_P or \mathbf{f}_P from \mathbf{f}_M , it is necessary to know how the lever model matrix $\mathbf{L}(\alpha_M)$ is calculated.

From Eq. (4.11), we know how $\mathbf{L}(\alpha_M)$ is expressed in instrument base. In the following, we would like to obtain the lever model matrix in robot base $(\mathbf{x}_0, \mathbf{y}_0, \mathbf{z}_0)$. Recall that

$${}^0\mathbf{L}(\alpha_M) = \alpha_M (\mathbf{I} - {}^0\mathbf{z}_I {}^0\mathbf{z}_I^T) + {}^0\mathbf{z}_I {}^0\mathbf{z}_I^T.$$

It is therefore necessary to get both ${}^0\mathbf{z}_I$ and the lever ratio α_M .

The computation of ${}^0\mathbf{z}_I$

${}^0\mathbf{z}_I$ is actually a unit vector along the instrument axis, thus it can be expressed as:

$${}^0\mathbf{z}_I = \frac{{}^0\mathbf{d}_{F_0P}}{\|{}^0\mathbf{d}_{F_0P}\|} = \frac{{}^0\mathbf{d}_{OP} - {}^0\mathbf{d}_{OF_0}}{\|{}^0\mathbf{d}_{OP} - {}^0\mathbf{d}_{OF_0}\|}. \quad (4.18)$$

We have the vectors ${}^0\mathbf{d}_{OP} = {}^0\mathbf{p}_P$ and ${}^0\mathbf{d}_{OF_0} = {}^0\mathbf{p}_{F_0}$. ${}^0\mathbf{p}_P$ can be obtained directly from the robot measures and ${}^0\mathbf{p}_{F_0}$ is the trocar position expressed in robot base frame \mathcal{F}_0 , whose value can be estimated in real-time in our system by using the method detailed in Chapter. 2.

The computation of α_M

By the definition of l_M in Eq. (4.1), from ${}^I\mathbf{d}_{F_0M} = {}^I\mathbf{d}_{F_0P} + {}^I\mathbf{d}_{PM}$, we have

$$l_M = l_P + l_{PM}, \quad (4.19)$$

where l_{PM} is a signed value indicating the distance between point P and point M . When point M and point P at the same side of the fulcrum point F_0 , both l_{PM} and l_M are positive, otherwise, they are negative. Specially,

$$l_P = \|\mathbf{d}_{F_0P}^0\| = \|\mathbf{d}_{OP}^0 - \mathbf{d}_{OF_0}^0\| = \|\mathbf{p}_P^0 - \mathbf{p}_{F_0}^0\|. \quad (4.20)$$

With l_M and l_P known, the lever ratio can be easily calculated from:

$$\alpha_M = \frac{l_M}{l_P}. \quad (4.21)$$

4.2.4 Verification of lever model

In order to verify the effectiveness of the lever model, we calculate the tip velocity ${}^0\mathbf{v}_T$ in two different ways. One is using the rigid body formula with information of robot wrist velocity ${}^0\mathbf{v}_P$ and ${}^0\omega_I$. Recall that ${}^0\omega_I$ is affected by noise due to the potentiometers. The other approach is using the lever model with ${}^0\mathbf{v}_P$ and the estimated trocar position.

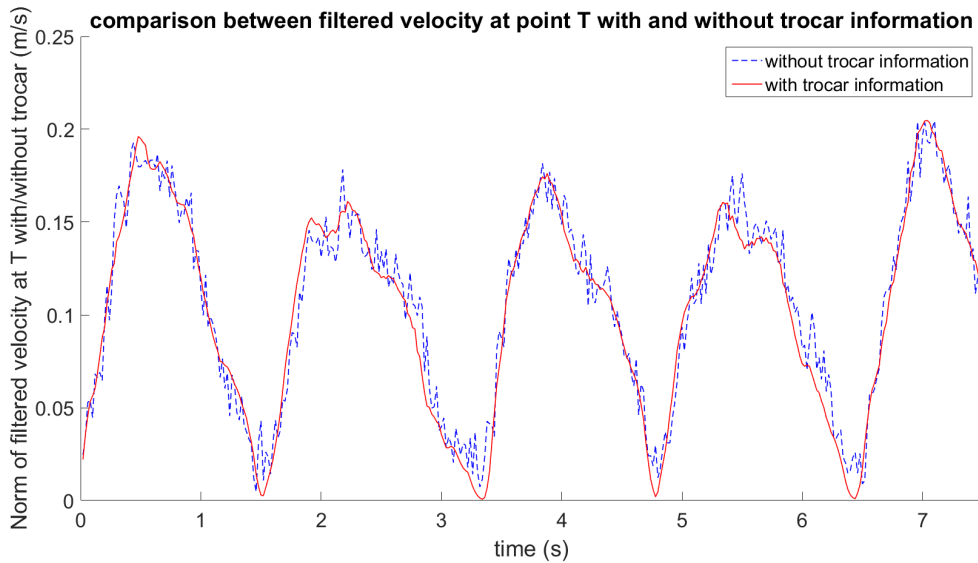


Fig. 4.2 **Comparison of noise level of the instrument tip velocity with and without using trocar information.** The red solid line represents the method with lever model while the blue dashed line represents that without using lever model. ${}^0\mathbf{v}_P$ used in both methods is filtered by a first order low pass digital filter.

Fig. 4.2 shows the comparative results. The blue dashed line and the red solid line correspond to the first and the second method, respectively. A first order low pass digital

filter is added in order to filter ${}^0\mathbf{v}_P$. Obviously, the tip velocity derived from the lever model is less noisy, validating the effectiveness of lever model.

4.2.5 Discussion about lever model

The following discussions are assumed in the instrument frame \mathcal{F}_I . Expanding the Eq. (4.11), one gets the following three equations:

$$v_{Mx} = \alpha_M v_{Px} , \quad (4.22)$$

$$v_{My} = \alpha_M v_{Py} , \quad (4.23)$$

$$v_{Mz} = v_{Pz} . \quad (4.24)$$

These equations indicate the features of the lever transformation in terms of kinematics. The movements of the instrument inserted into the abdomen during surgical procedures can be divided into two basic types: translations along the penetration axis and rotations about the fulcrum point. All instrument movements are actually their combinations. Eq. (4.24) corresponds to the translation while Eq. (4.22) and Eq. (4.23) correspond to the rotations. For translational movements, *i.e.*, in the \mathbf{z} direction, the coefficient is a constant number 1, meaning that all the points on the instrument have the same translational velocity. But for rotational movements, *i.e.*, in the \mathbf{x} and \mathbf{y} directions, the coefficients are the lever ratio, which varies according to the insertion depth. Therefore, there is a phenomenon of gain anisotropy in terms of the movement amplitude. Moreover, α_M is a signed number. When M stands for the instrument handle center point H , it is positive, while when M represents the instrument tip point T , it is negative. Namely, for rotational motions, when the surgeon's hand moves to one direction, the resulting movements of instrument tip inside the patient's body are in the reverse direction. This is referred as the fulcrum effect, which does not exist in the translational movement along the penetration axis. As a consequence, the direction of the instrument tip movement generally deviates from the direction of the hand movement.

Similarly, the expansion of Eq. (4.17) gives:

$$f_{Px} = \alpha_M f_{Mx} , \quad (4.25)$$

$$f_{Py} = \alpha_M f_{My} , \quad (4.26)$$

$$f_{Pz} = f_{Mz} . \quad (4.27)$$

The dynamic transformation of the lever model indicates exactly the same phenomenon from a dynamic point of view. The inertia is anisotropic due to a depth-dependent gain ratio for rotations to reorient the instrument and a constant gain for translation along the instrument axis. The inertia is direction-dependent as well, with direction switch of the net forces exerted at H , P and T . These features lead to a deviation of direction of variable acceleration, which might cause system instability.

From the above discussions, the characteristics of the kinematic and dynamic transformation of the lever model can boil down to the reciprocal inversion and scaling of motions and the altered sensation of forces. The relation between movements of the surgeon's hand outside the body and the resulting movements of instrument tip inside the patient makes the manipulation rather complex, which greatly challenges to the surgeon's motor skills and cognitive abilities. Besides, the fulcrum effect and the anisotropy are likely to contribute to more tissue damage than in open surgery [5]. It also affects the time to initiate a movement [6]. Our aim, in the chapter, is to use the comanipulator to add compensation so as to guide and ease the surgeon's gesture. Viscous fields will be used for this purpose.

4.3 Viscosity control with lever model

In this chapter, the same viscosity control law is employed as presented in Eq. (3.1) of Chapter. 3. For a specific point M belonging to the instrument axis where the controller behaves, Eq. (3.1) writes as:

$$\mathbf{f}_M = -b \cdot \mathbf{v}_M, \quad (4.28)$$

where b is the viscous positive coefficient. For the sake of simplicity, in this chapter, b keeps as a constant rather than a variable. This behavior generates the viscous forces opposite to velocities, isotropically, at a point M . Using lever model described in Sec. 4.2, this formula can also be expressed at point P :

$$\mathbf{f}_P = -b \mathbf{L}^2(\alpha_M) \mathbf{v}_P \quad (4.29)$$

It can then be projected in base $(\mathbf{x}_0, \mathbf{y}_0, \mathbf{z}_0)$ as:

$${}^0\mathbf{f}_P = -{}^0\mathbf{B} {}^0\mathbf{v}_P, \text{ with } {}^0\mathbf{B} = b {}^0\mathbf{L}^2(\alpha_M) \quad (4.30)$$

The matrix ${}^0\mathbf{B}$ is an anisotropic viscosity matrix, expressed in base $(\mathbf{x}_0, \mathbf{y}_0, \mathbf{z}_0)$, that provides an isotropic behavior at point M with a viscosity coefficient b . Notice that:

- When $M \equiv T$, remembering that l_T and l_P are opposite, $\alpha_T = l_T/l_P$ is negative, corresponding to the fact that both velocities and lateral forces of point P and point T are in the opposite direction.
- When $M \equiv H$, $\alpha_H = l_H/l_P$ is positive, meaning that the movements of and the applied forces on P and H are in the same direction.

In laparoscopic surgery, point M , where the viscosity controller is implemented, could be potentially chosen as the instrument handle center H or the instrument tip T . In order to study the effect of the controller implementation position, an experiment was conducted, which is explained in detail in following section.

4.4 Materials and methods

4.4.1 Experiment setup

Subjects are invited to participate a simple point-to-point movement experiment. This type of movements is well studied in human motor neuroscience and incorporated in the Peg-Board task of the Fundamentals in Laparoscopic Surgery [77, 78].

Fig. 4.3 shows a typical experiment scene. Achilles and a subject together hold and manipulate the instrument which is inserted into the laparoscopic trainer box through a trocar. Achilles is controlled at the sampling interval of 1 ms according to Eq. (4.30). The trocar is specially designed so that the effect of friction and backlash is minimized, which is partially enlarged in Fig. 4.3.

The inner scene of the trainer box is hidden by a cloth. An endoscope is used to provide visual feedback of the experimental field which is projected on a 2D image screen in front of the subject. The instrument tip is always kept in the camera field of view during the whole experiment.

Three metal points A , B and C , indicated as red circles in Fig. 4.3, are set as point-to-point movement targets in such a way that both translational, rotational and combinational motions are involved. The vertical depth between A and B is 25 mm. B and C are at the same depth level with a horizontal distance of 51 mm. These metal points are connected to an Arduino Mega 2560 board. A touch between the instrument tip and any of the three metal points will trigger a signal to indicate the start or the end of a movement. A signal screen serves as an indicator to remind the subject the current movement trajectory.

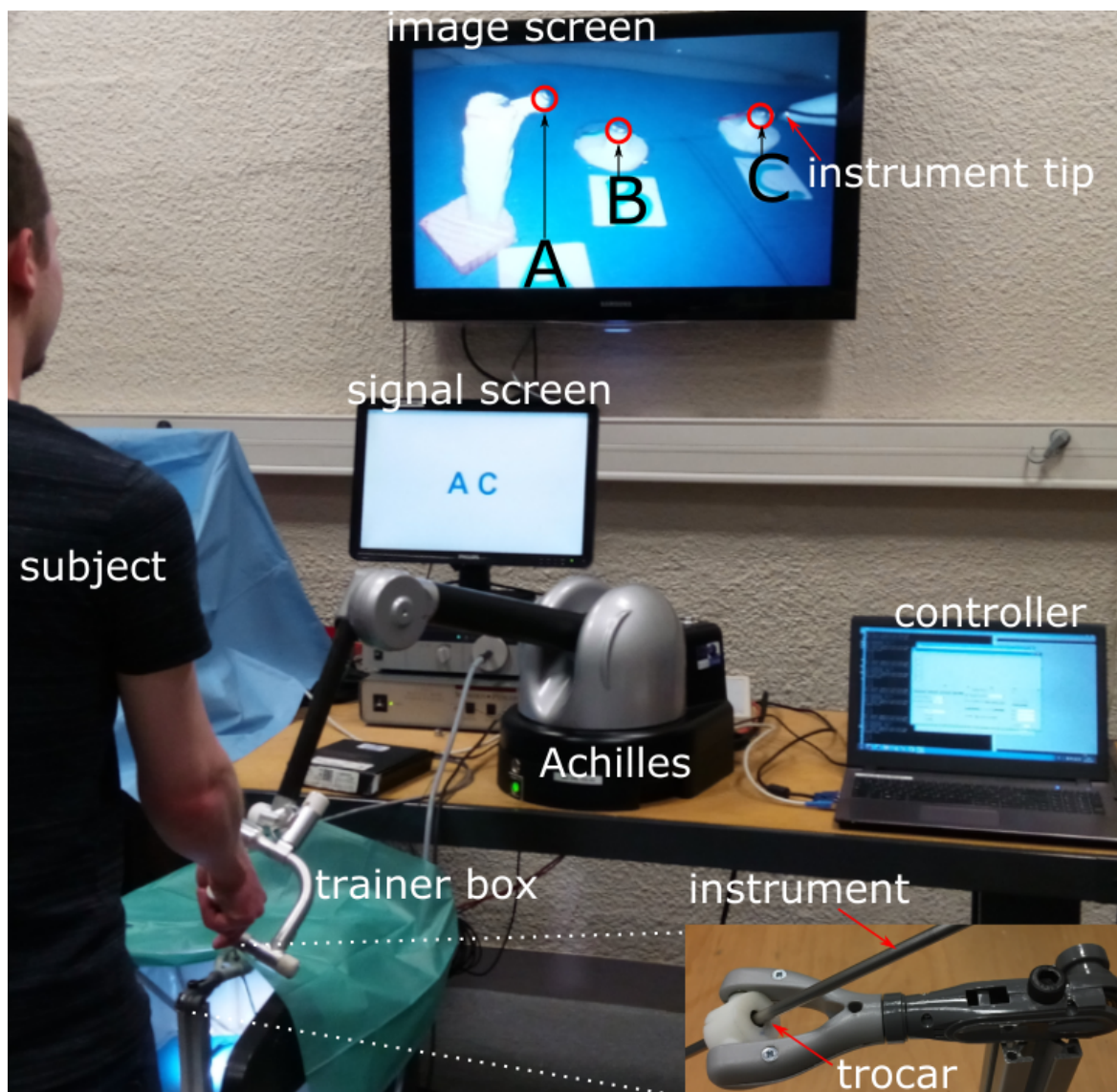


Fig. 4.3 Experimental setup.

4.4.2 Experiment protocol

Subjects.

17 naive subjects, 6 females and 11 males, aged from 21 to 53, have participated in the experiment. Two of them are left-handed. All subjects have given informed consent. The experiment was performed in accordance with the ethical standards laid down in the 1964 Declaration of Helsinki.

Three sessions.

The insertion depth is defined as the distance between the trocar point F_0 and the instrument tip point T , denoted as \mathbf{d}_{F_0T} . According to the insertion depth of the instrument into the trocar, the whole experiment is divided into three sessions : deep insertion, middle insertion and small insertion, illustrated in Fig. 4.4. The large insertion depth varies from 280 mm to 300 mm, the middle one from 195 mm to 215 mm while the small one from 95 mm to 115 mm. For each session, the experimental procedure and the setup keep unchanged expect for the adjustment of the insertion depth, which is obtained by moving the environment inside the laparoscopic trainer. Note that the camera-environment spatial relationship keeps consistent so that the experimental view displayed on the image screen is the same for all three sessions.

Four trajectories.

We call the one-way targeting movement from one point to another as a task. AB , BA , BC and AC are picked as possible trajectories for these tasks. The ideal trajectory of BC is a pure rotation while the other three are a combination of rotation and translation. For each task, one of the four trajectories is randomly selected by the algorithm and displayed on the signal screen to provide instructions to subjects. As indicated in Fig. 4.3, the current trajectory is AC .

Three controllers.

Depending on where the viscosity control law is implemented (at the instrument handle center H or at the instrument tip T), two controllers, named as controller H and controller T , are designed. In addition, a null controller, denoted as controller N , is also considered in the experiment as control situation under which the force is identically equal to zero. The constant viscosity coefficient is tuned to be $20 \text{ N} \cdot \text{s} \cdot \text{m}^{-1}$ through a prior experiment. In each

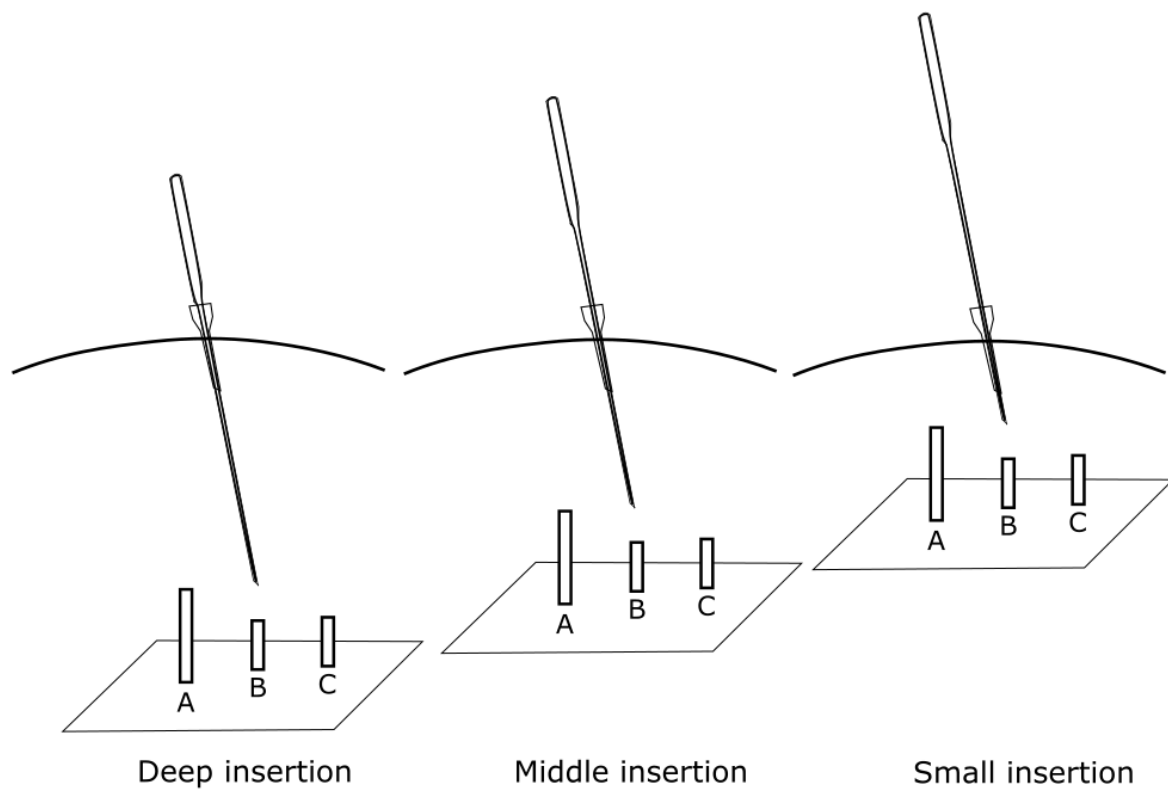


Fig. 4.4 **Three sessions of different insertion depths.** The manipulation area with points *A*, *B* and *C* is moved to change the instrument penetration depth.

task, once the trajectory is determined, one of the three controllers is picked by the algorithm in a random way as well.

One thing worthy to point out is that for large insertion, the lever ratio α might become a large number, whose square results in a large coefficient and causes the system instability. Therefore, in the large insertion session α is saturated to be $\alpha_s = 3.5$ for security reason. Of course, the saturation is applied equally in all directions in order to avoid further distortion.

Training and recording.

Since the way of manipulating the instrument resembles the procedures in traditional minimally invasive surgery, the disturbance of fulcrum effect and the loss of depth information pose great difficulties to naive subjects. Therefore, in the training step, subjects are suggested to do enough practice until their learning curve reaches a plateau. Formal experiment follows the training stage. Each task is repeated 5 times. During the experiment, tip positions of the instrument with respect to the robot base frame are recorded in real time at the sampling rate of 100 Hz.

Questionnaire.

In each depth session, after the experiment, subjects are required to fill in a questionnaire. Basically, they need to grade the three controllers from 1 to 5 (a higher score indicates that they prefer the sensation of the corresponding controller) in terms of performance such as movement smoothness, speed, targeting precision, etc. The questionnaire is presented in Appendix A. A short post experiment is proposed for subjects to help them recall and better compare their sensations to distinguish the behaviors of the controllers.

4.4.3 Performance indicators

Since it is the tip of the instrument that goes into the patient's abdomen and directly contact with tissues and organs, the tip movement quality is considered as the most essential characteristic. In this chapter, the same indicators ($PI_1 - PI_6$) listed in Chapter. 3 are used to describe the tip trajectory features under different controllers. They are peak velocity, total task time, correction time ratio, jerk, trajectory curvature and energy.

Apart from these indicators, a synchronization metric is also proposed as a measurement of tip movement characteristic, whose definition is illustrated in Fig. 4.5. The dashed line represents a typical trajectory of tip movement from the starting point to the ending point. This movement, as shown in Fig. 4.5 (A), comprises actually both angular motions of the instrument axis (θ , the angle between an instantaneous instrument axis and the initial one)

and the depth of the tip point (d , the signed distance between an instantaneous tip position and the starting point). v_θ and v_d in Fig. 4.5 (B) are normalized velocities of angle θ and depth d , respectively. The enclosed area by v_θ and v_d , depicted by the slashes, is considered as where the synchronization between angular motion and depth movement happens. We then define the synchronization metric as the ratio between this overlapped area, denoted as $A_{overlap}$, and the whole area encapsulated by v_θ and the horizontal axis, denoted as A_θ :

$$PI_7 = \frac{A_{overlap}}{A_\theta}. \quad (4.31)$$

A large value indicates a better synchronized movement and thus more natural.

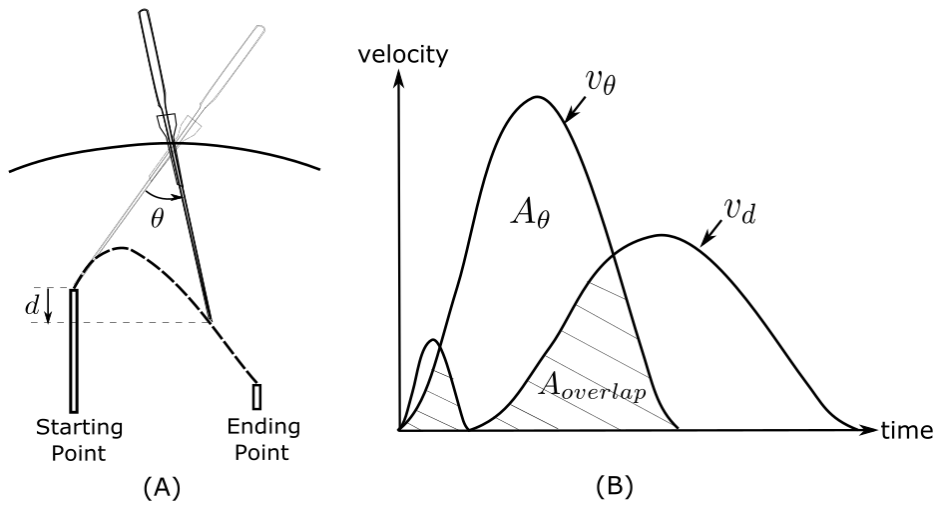


Fig. 4.5 Synchronization illustration.

4.4.4 Data analysis

1.86 % of the recorded files are not usable due to the environment disturbance to subjects and thus discarded during the data processing. The time series of the recorded Cartesian coordinates of the instrument tip were filtered by a low pass IIR filter with order 8, frequency 5 Hz. The starting and ending data for each task are determined by a velocity norm threshold (0.005 m/s).

Each performance metric is subjected to a three-way analysis of variance (ANOVA; factors: trajectory; insertion depth; controller) test, which determines whether the experimentally observed difference is statistically significant or not. In the literature on motion analysis [27], a difference is considered as statistically significant if the calculated p-value is smaller than 0.05. Therefore, the significance level for the ANOVA analysis is set as 0.05. Then

Tukey's HSD post hoc test is conducted to further compare between any of two controllers to find out where the difference lies.

4.5 Experimental results

Fig. 4.6 - Fig. 4.10 present the mean values and standard errors of the mean (SEMs) of corresponding metric averaged by all subjects.

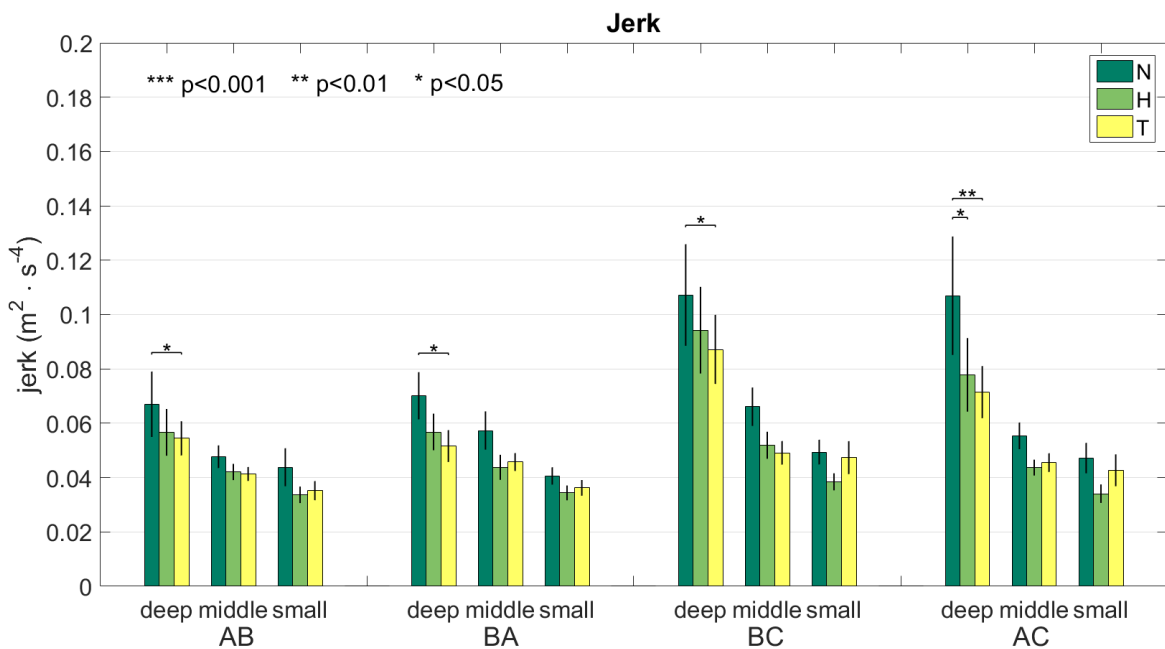


Fig. 4.6 Graph showing mean values of jerk of 17 subjects, for all 4 trajectories under 3 controllers. Results are grouped by trajectories, inside which further subgrouped by insertion depth. Error bars represent the standard error of the mean (SEM) with 95% confidence interval. Asterisks indicate significance level based on Tukey's HSD post hoc test between two controllers. Sample size $N = 17$. Same representations for Fig. 4.7 - Fig. 4.10.

Jerk. In general, both the mean and the SEM values of the jerk under controller N are larger than those under controllers H and T , for all combinations of trajectories and insertion depths. This is evidenced by the significant difference of the main effect of controller given by ANOVA ($F(2, 12) = 41.56, p < 0.001$). Multiple comparison test further shows that the difference is caused mainly due to controller N while no significant difference is observed between controllers H and T (N VS. H : $p < 0.001$; N VS. T : $p < 0.001$; H VS. T : $p = 0.97$). In addition, the interaction between controller and insertion depth is significant ($F(2, 12) = 4.87, p = 0.015$), indicating that the insertion depth has an influence on the

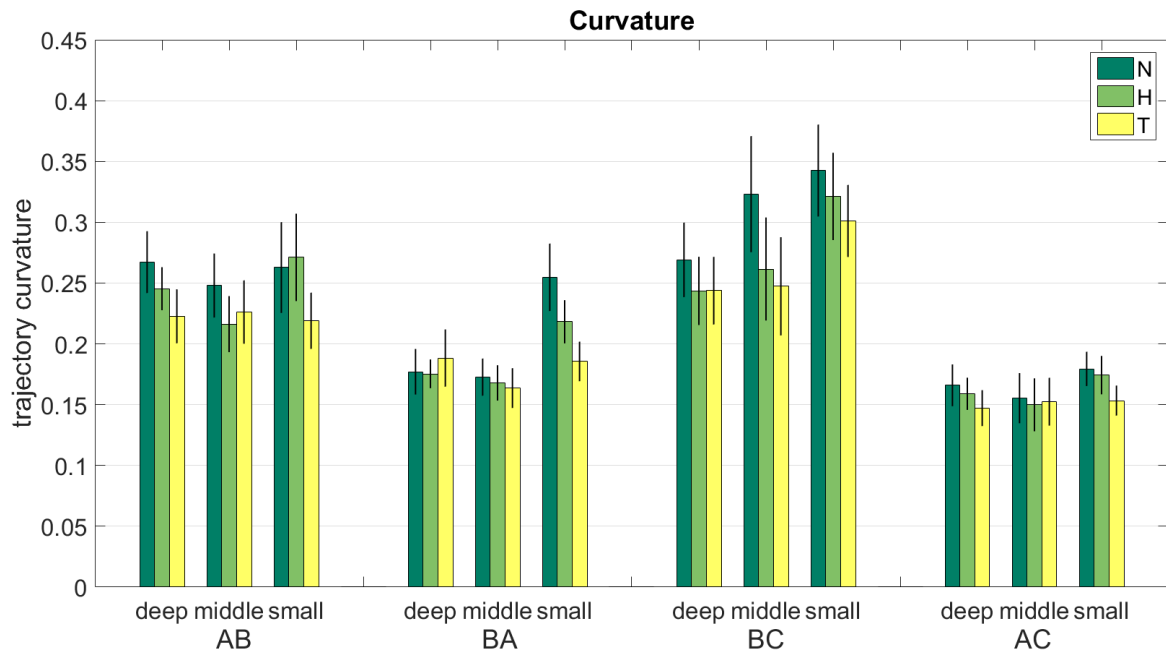


Fig. 4.7 Mean values and SEM of trajectory curvature of 17 subjects.

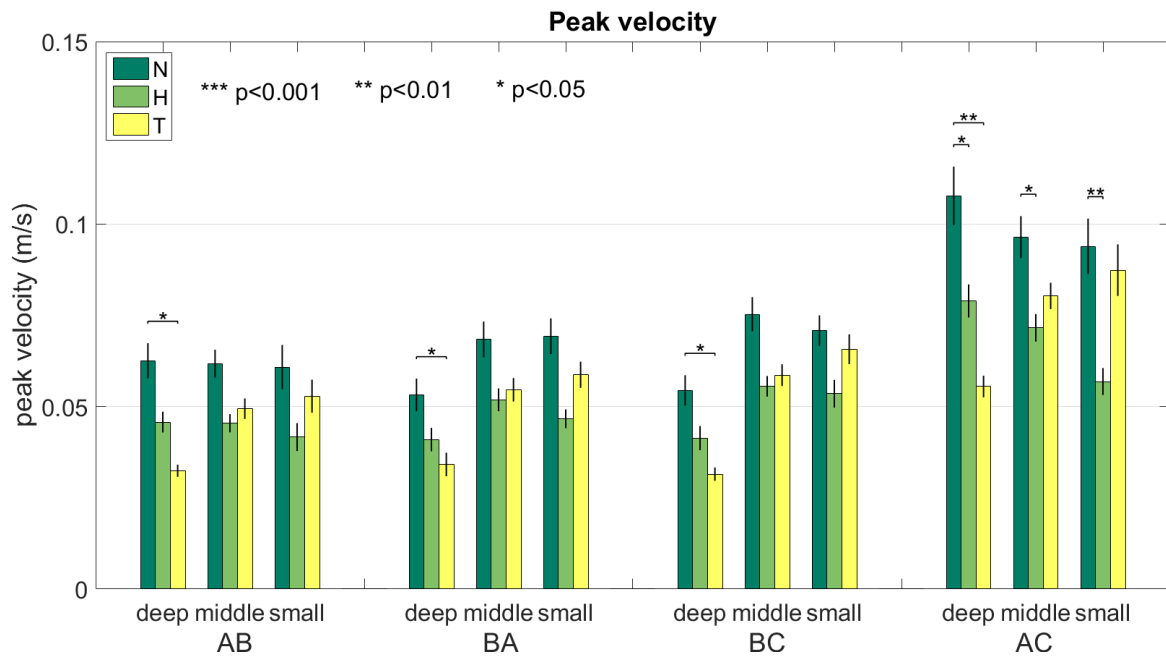


Fig. 4.8 Mean values and SEM of peak velocity of 17 subjects.

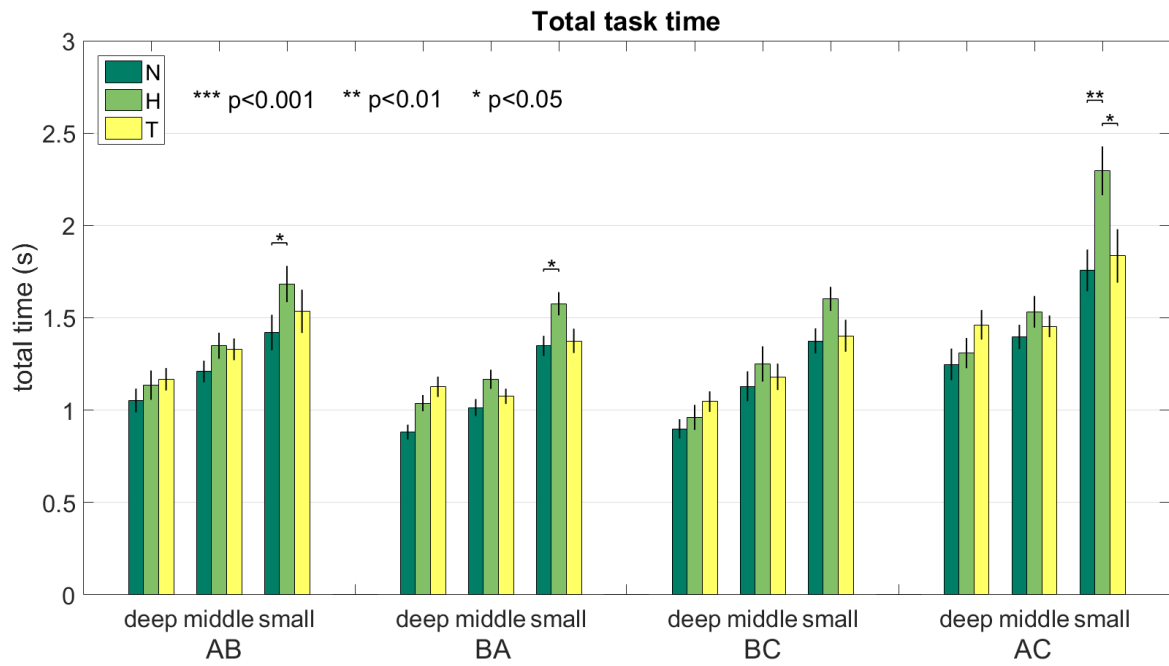


Fig. 4.9 Mean values and SEM of total task time of 17 subjects.

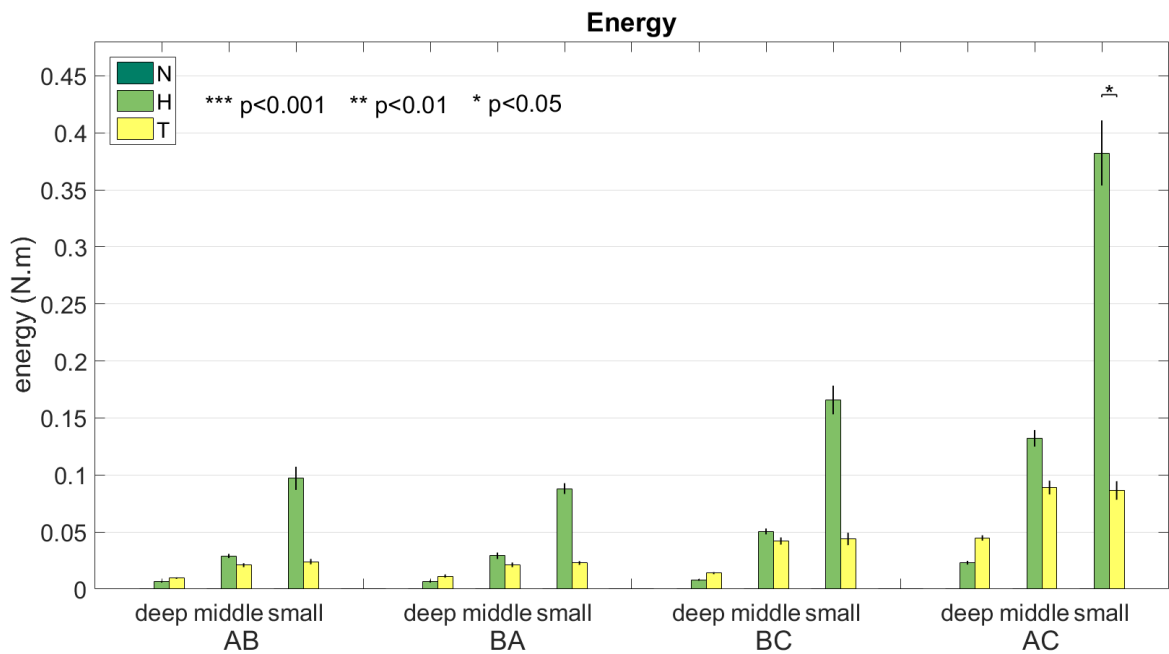


Fig. 4.10 Mean values and SEM of energy of 17 subjects.

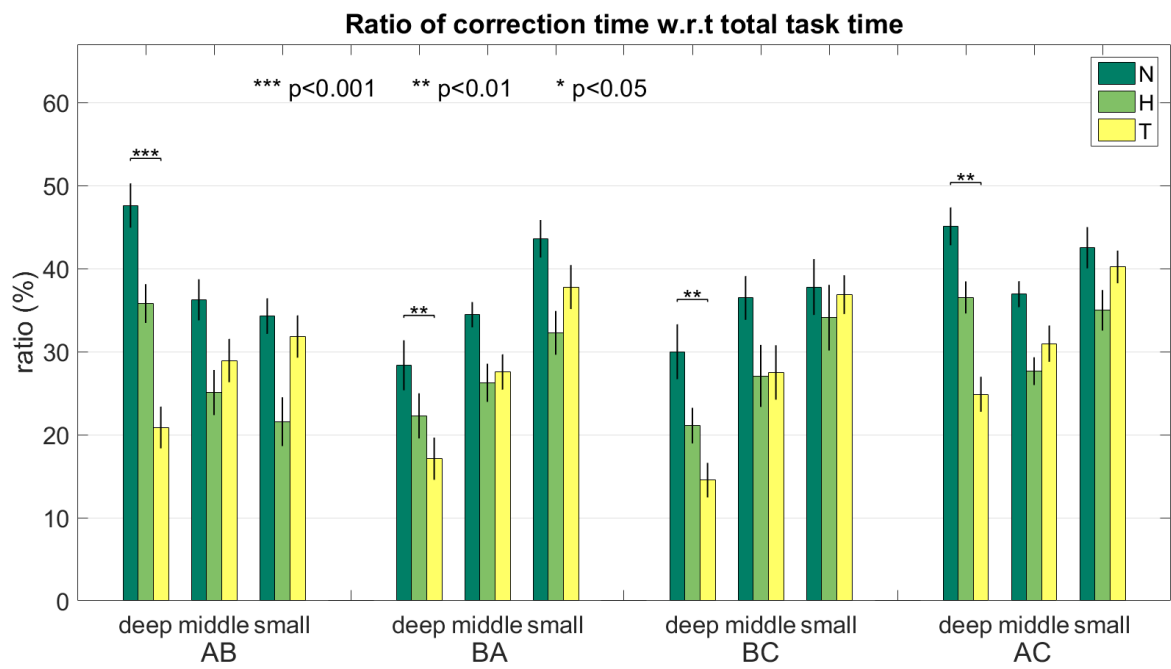


Fig. 4.11 Mean values and SEM of correction time ratio of 17 subjects.

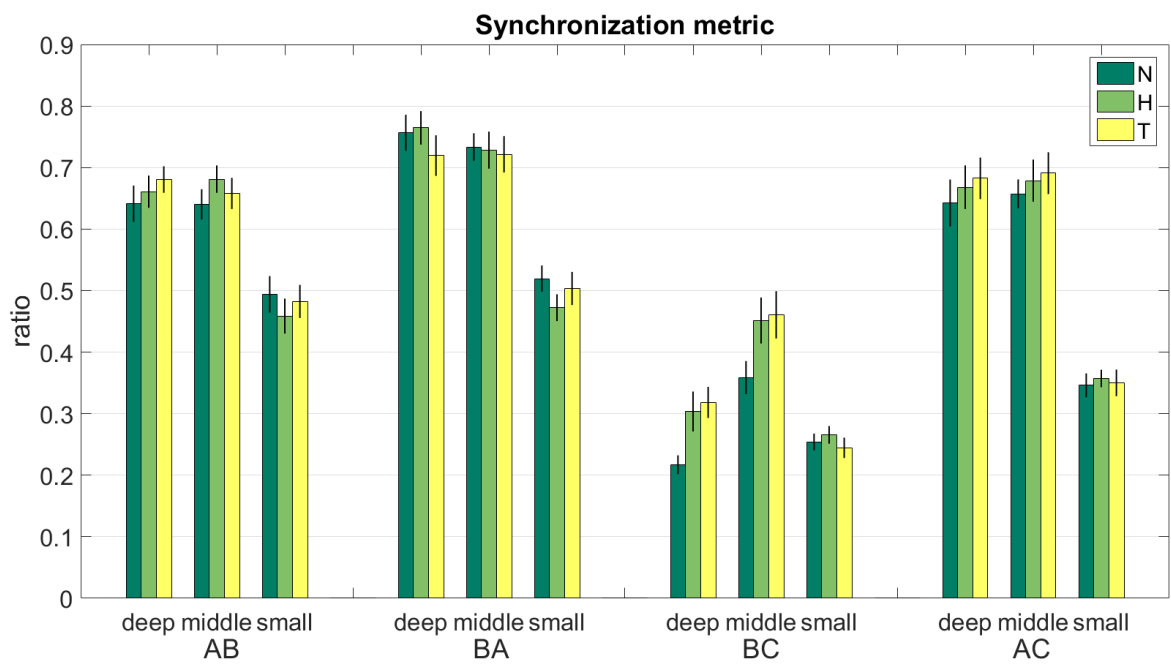


Fig. 4.12 Mean values and SEM of synchronization of 17 subjects.

controller behavior. Meanwhile, no significant effects of the controller-trajectory combination are found ($F(2, 12) = 0.68, p = 0.67$).

Curvature. Globally, controller *N* has slightly smaller mean values of curvature than controllers *H* and *T* for all possible situation. The small p-value ($F(2, 12) = 13.35, p < 0.001$) of the main effect indicates a significant difference of controller. The difference, revealed by the Tukey's HSD post hoc test, lies mostly in controller *N* (*N* VS. *H*: $p=0.03$; *N* VS. *T*: $p<0.001$; *H* VS. *T*: $p=0.13$). Moreover, the p-values of intersection terms for the combinations of controller-insertion depth and controller-trajectory are 0.26 and 0.50, respectively, meaning no significant interaction effects.

Peak velocity. ANOVA reveals significant differences in peak velocity of the instrument tip under three controllers ($F(2, 12) = 55.55, p < 0.001$), with controller *N* groups always displaying significantly large mean speed (*N* VS. *H*: $p<0.001$; *N* VS. *T*: $p<0.001$; *H* VS. *T*: $p=0.46$). The p-value of 0.001 indicates a significant interaction between controller and insertion depth while the p-value of 0.31 for the interaction between controller and trajectory shows little evidence of controller effect depending on task trajectory.

Total task time. A significant effect is also evident in terms of the total task time for three controllers ($F(2, 12) = 27.59, p < 0.001$). Controller *N* takes significantly less time than other two controllers, indicated by the multiple comparison test (*N* VS. *H*: $p<0.001$; *N* VS. *T*: $p=0.003$; *H* VS. *T*: $p=0.023$). The p-value of 0.0015 that ANOVA finds for the interaction between controller and insertion depth suggests a high probability of dependence between the two factors. On the other hand, the large p-value of 0.77 means the trajectory factor does not significantly have an impact on the controller performance.

Energy. The energy metric of controller *N* is always 0 due to the null force. The difference of energy consumption between controllers *H* and *T* is significant ($F(2, 12) = 16.47, p < 0.001$). The p-value corresponding to the interaction term of controller-insertion depth shows a statistical significance ($p = 0.0034$) while the p-value of 0.096 for the interaction between controller and trajectory suggests that controller behaviors are similar across all four trajectories.

Correction time ratio. Compared with controllers *H* and *T*, controller *N* spends significantly more time on target correction movement in all cases ($F(2, 12) = 50.32, p < 0.001$). Multiple comparison tests are further performed and find out that controller *N* contributes to the main part of the difference (*N* VS. *H*: $p<0.001$; *N* VS. *T*: $p<0.001$; *H* VS. *T*: $p=0.90$). Furthermore, the variation of correction time ratio is reflected in significant interaction between controller and insertion depth ($F(2, 12) = 12.61, p < 0.001$). No significant effect of the controller-trajectory combination is revealed.

Synchronization. As to the synchronization metric, the mean value of the three controllers are in general at the same level, with no significant difference found ($F(2, 12) = 3.09, p = 0.083$). The small p-values of interaction terms for combinations controller-insertion depth ($p = 0.014$) and controller-trajectory ($p = 0.025$) indicate that both insertion depth and trajectory have a significant effect on the controller performance.

Scores from questionnaire. Each subject gave a score to the three controllers N , H and T according to their sensations in terms of movement smoothness, targeting precision, compensation for visual depth loss, etc. Then we averaged the scores across all performance indicator terms, all subjects and all insertion depths. The scores of controllers N , H and T are 19.8, 19.2 and 20.9, respectively. For deep insertion, controller H gets the highest score 21.9, 3 larger than controller N and 1.8 larger than controller T . The results are reversed for small insertion depth, where controller T outscores controllers N and H by 1.4 and 5.3, respectively. As to middle insertion depth, the scores of the three controllers do not differ too much. Controller T obtained a slight larger score of 20.9, with 0.7 and 1.5 higher than controllers N and H , respectively.

4.6 Discussion

The trocar and the inserted instrument form a sliding lever, which brings complex kinematic and dynamic transformations and poses many difficulties to operators [60]. Using a robotic arm as a comanipulator can improve the operator's performance in terms of gesture quality. This is proven by experiments in Chapter. 3, which is designed to compare the behavior performance of viscosity controllers. In the point-targeting experiment carried out in this chapter, controller N , the null controller, is conceived as the control group. It is observed that controller N globally gives a larger jerk than the other two controllers do regardless of the trajectory and the insertion depth. Since a small jerk value indicates a smoother movement, the experimental results validate the hypothesis that the robot adding a viscous force could enhance the motion smoothness. Moreover, the comparatively smaller SEMs of controllers H and T indicate that subjects have a more stable level of motion smoothness. Similarly, for another gesture quality indicator, curvature, controller N yields larger values for most of the combination of trajectory and insertion depth, which is consistent with the conclusion drawn in Chapter. 3.

The metrics of peak velocity and total task time describes coherent controller characteristics. Indeed, for controller N , the null force allows a large peak velocity and consequently a short total task time compared with controllers H and T . Certainly, the task duration is better

to be small. Fig. 4.8 and Fig. 4.9 show that controllers H and T significantly slow down the peak velocity, but they do not require much longer time from a general point of view.

With no viscous force exerted at the robot end-effector under controller N , operators may have a lower tendency to feel the sensation of fatigue. However, they need to put much more concentration when approaching the final target. Fig. 4.11 reveals that by adding a damping force, no matter at tip or at handle, significantly shortens the ratio of correction time and enhances the precision and easiness of target achievement. As to the metric of synchronization, the not significant difference between with and without force according to ANOVA indicates that the viscosity controller does not have much influence on the depth-angle behavior synchronization, even though graphically we could find a difference for trajectory BC .

The experimental results show that insertion depth has an evident effect on the controller performance, in accordance with the lever model. For the situation where the instrument is deeply inserted into the trainer box, controller T , whose implementation is at tip, always generates a large lever ratio ($\alpha_T \gg 1$). The square of α_T even amplifies the viscosity coefficients of the lever matrix, resulting in a very large robot end-effector force, especially when the tip velocity is high. If the controller is implemented at instrument handle, namely controller H for the deep insertion case, the lever ratio α_H would never reach an equally large value as α_T ($1 < \alpha_H < \alpha_T$).

This could explain the observation that in deep insertion controller T has a smaller peak velocity and takes a bit longer time than H to complete the task. The relatively large energy consumption for controller T due to the large force is also quite straightforward to understand. One thing to be noticed is that for the security reason we saturated α_T linearly ($\alpha_T = \alpha_{T_s}$, if $\alpha_T > \alpha_{T_s}$, α_{T_s} is the saturation limit of lever ratio, set as 3.5 in the experiment). That is why for deep insertion the general energy is small compared with the other insertion depths. Fig. 4.11 shows that the controller implementation position has a clear effect on the correction time ratio. More specifically, the large robot force due to the large lever ratio makes the target achieving movement easier and more precise to handle, no matter what trajectory it is. However, the differences of performance with respect to jerk, curvature and synchronization between controllers H and T are not that obvious. For deep insertion of all trajectories, controller T globally slightly outperforms controller H from the aspect of motion smoothness. As regards gesture naturality and movement synchronization, no absolute conclusion could be drawn to decide which one is more suitable.

Conversely, when the instrument insertion depth is small, the lever ratio α_T for controller T is a small value ($\alpha_T < 1$) while α_H for controller H is larger ($1 < \alpha_H < 2$). This makes the results of the performance metrics reversed. Precisely, in comparison with controller

T , controller H limits the peak velocity and shortens the correction time, but consumes significantly more time and energy. The jerk, as in deep insertion case, does not greatly rely on the controller position. The curvature, however, shows a more obvious tendency that adding viscosity control at tip could be more beneficial for straight movement path. Again, the synchronization of depth-angle motion does not rely too much on whether it is controller H or controller T .

In between where the insertion depth is middle, all performance metrics of controllers H and T gives basically the same level of values. This observation is consistent with the theoretical lever model behavior because α_H and α_T are both around 1. In fact, if we could ensure an absolute middle insertion depth, namely, $\|\mathbf{d}_{F_0T}\| = \|\mathbf{d}_{F_0H}\|$, we would expect the exactly same metric values from controllers H and T .

From the above discussion, it is obvious to say adding viscous force generally contributes to better gesture qualities. Where to implement the viscosity control, however, is more tricky to decide. Adding at the instrument tip or at the handle both has its own advantages and drawbacks, which vary a lot according to the insertion depth.

From the questionnaire, we see that subjects' preference changes with insertion depth. When the instrument is deeply inserted, controller H is the most popular while when the insertion depth is small, controller T is preferred. Globally controller T provides the best sensation. This qualitative sensation preference from the questionnaire provides a contradictory evaluation of controller performance as regards motion smoothness and naturality.

4.7 Conclusions

The lever effect is a very important phenomenon in laparoscopic surgery, posing huge difficulties and challenges to surgeons. Adding viscous force to the surgical instrument is an option to compensate the lever effect and enhance surgeons' performance. In order to avoid using noisy signals from low-precision potentiometers, a lever model is proposed, which allows to implement the viscosity control at any point belonging to the instrumental axis. However, it is not clear where the controller should exactly be put. Two points, the centers of instrument tip and handle, are taken into consideration since the former touches directly the patient's organs while the latter influences the surgeon's motor sensation. By designing simple point-to-point target movement experiments, we quantified and compared the performance of different viscosity controllers. It turns out that the performance of controller H (implementation at the handle point) or T (implementation at the tip point) depends largely on the instrument insertion depth into the trocar. This could give cues to design, in the future, a controller whose tuning varies with the depth.

Chapter 5

Conclusions and perspectives

5.1 Conclusions

The advent of laparoscopic surgical techniques revolutionized the modern surgery history which bring beneficial advantages to patients. However, it poses numerous challenges to surgeons, making some kinds of MIS much difficult to perform compared with open surgery. To cope with these difficulties, robots are used to assist laparoscopic surgery. Telemanipulated robotic surgery is a widely exploited field, where the da Vinci surgical system lies in. In spite of great improvements it brings to surgeons' operation, the telemanipulation concept raises new problems as well. In this work, we employ a different concept, comanipulation, to explore and exploit the possibility of inheriting the advantages of telemanipulated robots while overcoming its drawbacks.

The comanipulator used in this work is named as "Achilles", a serial robotic arm with 3 active joints and 3 passive joints, which holds the surgical instrument together with the surgeon. By designing control laws, Achilles could provide different force fields to guide surgeons' gestures such as filtering out the surgeon's hand tremor. The implementation of these assistive functions requires the basic knowledge of the real-time trocar position with respect to the robot base. Of course, the trocar position can be obtained at the initial registration stage. The problem, however, is that the registration procedure is time-consuming and needs to be redone when the robot or the patient moves. An important part of this work is dedicated to solve this issue. A robust and real-time trocar detection and localization algorithm based on the least square method is proposed, whose effectiveness and efficiency are validated through both dry-lab experiments by subjects and wet-lab evaluations by surgeons. With the trocar information known, a real-time gravity compensation for the instrument is implemented so that the surgeon is relieved of the instruments, especially of heavy motorized ones.

Different from the bone surgery where precise surgical geometries could be predefined, and from the microsurgery whose operating workspace is strictly limited, laparoscopic surgery possesses comparatively flexible surgical fields and large range of motion. These specific features make the over damped viscous force and elastic force fields often used in high-precision surgeries not applicable to laparoscopic surgery. Instead, variable viscous force field is applied, namely, the robot generates different level of resistance according to motion speed. However, an instability phenomenon similar to Stribeck effect was encountered when the variable viscosity control was programed. Given that the instability might potentially damage the system and result in disastrous consequences, we devote a whole chapter to deal with this issue. First of all, both theoretical analysis and practical experiments are performed to further verify this problem. Then the solution of adding a first order low pass filter is proposed to slow down the variation of viscosity coefficient. Theoretical investigation and experimental evaluation prove its efficiency. In order to understand how the filtered variable viscosity controller affects human's motion behavior, a simple point-to-point targeting movement is designed and carried out with 29 naive subjects. Experimental results show satisfying performance of the proposed solution.

Once the instability issue of the variable viscosity control is solved, the next thing that we focus on is where to implement this controller. The centers of the handle and tip of the instrument are both of interest. Force exerted on the former has a main influence on the surgeon's motor sensation while the latter has a direct physical contact with the patient's organs and it concerns the surgeon's visual feedback as well. Before studying this question, it is necessary to know how to add viscosity control at different points of the instrument without using noisy signals of orientation measurements. To achieve this aim, the key point is to establish a relationship between different points belonging to the instrument in terms of velocity and force. This relationship is formulated as the "lever model". We then designed another simple point-to-point movement, where controllers adding at the centers of handle and tip of the instrument (controllers H and T , respectively) as well as a null controller are involved. Performance analysis on the characteristic metrics indicates that controllers H and T has their own benefits depending on the instrument insertion depth into the trocar, but globally, both of them have a positive effect on the human motion behavior, in correspondence with previous experiments.

5.2 Perspectives

For the experiment aimed to compare viscosity controller implementation positions, a constant viscosity coefficient is used for the sake of simplicity. However, as discussed, variable

viscosity control with adaptive coefficients better meets the real laparoscopic needs. Advanced experiments should therefore be a concern in the future research.

At this stage, the coefficient values used in the viscosity control are fixed during the experiments. In reality, the parameters of controller coefficient have a crucial impact on the motion behavior and human sensation. Therefore, one of the future work would be parameter tuning with surgeons. Moreover, since the preference of force level changes from one person to another, controller parameter personalization would also be part of the work.

For the moment, all experiments are exclusively carried out in the lab with subjects having no surgical experience, except for the animal experiment verifying trocar detection algorithm. In the future, clinical experiments need to be performed with clinicians to further testify the instrument gravity compensation function and the capability of the filtered variable viscosity controller. As to the experiment designed to compare different controller implementation position, analysis and feedback from surgeons would be more convincing.

Additionally, it is observed from the experiment that subjects are to large extent disturbed by the loss of visual depth information due to the 2-dimensional images. It would also be of great interest to design some functions to compensate the lack of 3-dimensional vision. For example, better visualization could be achieved by means of augmented reality while virtual fixtures could provide elastic force fields to constrain or to guide the motion.

References

- [1] G. S. Litynski, "Endoscopic surgery: The history, the pioneers," *World Journal of Surgery*, vol. 23, no. 8, pp. 745–753, 1999.
- [2] O. Schneider and J. Troccaz, "A six-degree-of-freedom passive arm with dynamic constraints (padyc) for cardiac surgery application: Preliminary experiments," *Computer aided surgery*, vol. 6, no. 6, pp. 340–351, 2001.
- [3] A. R. Lanfranco, A. E. Castellanos, J. P. Desai, and W. C. Meyers, "Robotic surgery: a current perspective," *Annals of surgery*, vol. 239, no. 1, pp. 14–21, 2004.
- [4] C. Sutter, S. Sülzenbrück, M. Rieger, and J. Müsseler, "Limitations of distal effect anticipation when using tools," *New Ideas in Psychology*, vol. 31, no. 3, pp. 247–257, 2013.
- [5] S. J. Savader, K. D. Lillemoe, C. A. Prescott, A. B. Winick, A. C. Venbrux, G. B. Lund, S. E. Mitchell, J. L. Cameron, and F. A. Osterman Jr, "Laparoscopic cholecystectomy-related bile duct injuries: a health and financial disaster.," *Annals of surgery*, vol. 225, no. 3, p. 268, 1997.
- [6] W. Kunde, J. Müsseler, and H. Heuer, "Spatial compatibility effects with tool use," *Human Factors: The Journal of the Human Factors and Ergonomics Society*, vol. 49, no. 4, pp. 661–670, 2007.
- [7] S. P. Dharia and T. Falcone, "Robotics in reproductive medicine," *Fertility and Sterility*, vol. 84, no. 1, pp. 1–11, 2005.
- [8] T. J. Ortmaier, *Motion compensation in minimally invasive robotic surgery*. PhD thesis, Universität München, 2003.
- [9] D. B. Camarillo, T. M. Krummel, and J. K. Salisbury, "Robotic technology in surgery: past, present, and future," *The American Journal of Surgery*, vol. 188, no. 4, pp. 2–15, 2004.
- [10] R. M. Satava, "Emerging technologies for surgery in the 21st century," *Archives of Surgery*, vol. 134, no. 11, pp. 1197–1202, 1999.
- [11] G. H. Ballantyne and F. Moll, "The da vinci telerobotic surgical system: the virtual operative field and telepresence surgery," *Surgical Clinics of North America*, vol. 83, no. 6, pp. 1293–1304, 2003.
- [12] <http://www.ft.com/cms/s/0/f13a18be-e1cb-11e4-bb7f-00144feab7de.html#axzz42i1lns9M>.

- [13] J. M. Sackier and R. M. Satava, *Cybersurgery: Advanced technologies for surgical practice*. John Wiley & Sons, Inc., 1997.
- [14] Wikipedia, “Zeus robotic surgical system.” https://en.wikipedia.org/wiki/ZEUS_robotic_surgical_system. 2017.
- [15] M. Schurr, G. Buess, B. Neisius, and U. Voges, “Robotics and telemanipulation technologies for endoscopic surgery,” *Surgical endoscopy*, vol. 14, no. 4, pp. 375–381, 2000.
- [16] J. H. Palep, “Robotic assisted minimally invasive surgery,” *Journal of Minimal Access Surgery*, vol. 5, no. 1, p. 1, 2009.
- [17] M. D. Diodato Jr and R. J. Damiano Jr, “Robotic cardiac surgery: overview,” *Surgical Clinics of North America*, vol. 83, no. 6, pp. 1351–1367, 2003.
- [18] C. Scott, “Is da vinci robotic surgery a revolution or a rip-off,” *HealthlineNews. February*, vol. 12, 2015.
- [19] J. Sroga, S. D. Patel, and T. Falcone, “Robotics in reproductive medicine.,” *Frontiers in bioscience: a journal and virtual library*, vol. 13, pp. 1308–1317, 2008.
- [20] M. M. Rahman, R. Ikeura, and K. Mizutani, “Investigation of the impedance characteristic of human arm for development of robots to cooperate with humans.,” *JSME International Journal Series C*, vol. 45, no. 2, pp. 510–518, 2002.
- [21] X. Lamy, F. Colledani, F. Geffard, Y. Measson, and G. Morel, “Robotic skin structure and performances for industrial robot comanipulation,” in *Advanced Intelligent Mechatronics, 2009. AIM 2009. IEEE/ASME International Conference on*, pp. 427–432, IEEE, 2009.
- [22] M. Jakopec, S. J. Harris, P. Gomes, J. Cobb, B. L. Davies, *et al.*, “The hands-on orthopaedic robot" acrobot": Early clinical trials of total knee replacement surgery,” *IEEE Transactions on Robotics and Automation*, vol. 19, no. 5, pp. 902–911, 2003.
- [23] A. D. Pearle, D. Kendoff, V. Stueber, V. Musahl, and J. A. Repicci, “Perioperative management of unicompartmental knee arthroplasty using the mako robotic arm system (makoplasty),” *American Journal of Orthopedics*, vol. 38, no. 2, pp. 16–19, 2009.
- [24] G. Hughes, S. Vadera, J. Bulacio, and J. Gonzalez-Martinez, “Robotic placement of intracranial depth electrodes for long-term monitoring: Utility and efficacy,” *Cleveland Clinic*, 2013.
- [25] S. Ferrand-Sorbets, D. Taussig, M. Fohlen, C. Bulteau, G. Dorfmueller, and O. Delalande, “Frameless stereotactic robot-guided placement of depth electrodes for stereo-electroencephalography in the presurgical evaluation of children with drug-resistant focal epilepsy,” in *CNS Annual Meeting*, 2010.
- [26] R. Taylor, P. Jensen, L. Whitcomb, A. Barnes, R. Kumar, D. Stoianovici, P. Gupta, Z. Wang, E. Dejuan, and L. Kavoussi, “A steady-hand robotic system for microsurgical augmentation,” *The International Journal of Robotics Research*, vol. 18, no. 12, pp. 1201–1210, 1999.

- [27] R. A. MacLachlan, B. C. Becker, J. C. Tabarés, G. W. Podnar, L. A. Lobes Jr, and C. N. Riviere, “Micron: an actively stabilized handheld tool for microsurgery,” *IEEE Transactions on Robotics*, vol. 28, no. 1, pp. 195–212, 2012.
- [28] N. Zemiti, T. Ortmaier, and G. Morel, “A new robot for force control in minimally invasive surgery,” in *Intelligent Robots and Systems, 2004.(IROS 2004). Proceedings. 2004 IEEE/RSJ International Conference on*, vol. 4, pp. 3643–3648, IEEE, 2004.
- [29] A. Gijbels, N. Wouters, P. Stalmans, H. Van Brussel, D. Reynaerts, and E. Vander Poorten, “Design and realisation of a novel robotic manipulator for retinal surgery,” in *Intelligent Robots and Systems (IROS), 2013 IEEE/RSJ International Conference on*, pp. 3598–3603, IEEE, 2013.
- [30] J. Troccaz, *Medical robotics*. John Wiley & Sons, 2013.
- [31] M. Li and R. H. Taylor, “Spatial motion constraints in medical robot using virtual fixtures generated by anatomy,” in *Robotics and Automation, 2004. Proceedings. ICRA’04. 2004 IEEE International Conference on*, vol. 2, pp. 1270–1275, IEEE, 2004.
- [32] C. A. Moore Jr, M. A. Peshkin, and J. E. Colgate, “Cobot implementation of virtual paths and 3d virtual surfaces,” *Robotics and Automation, IEEE Transactions on*, vol. 19, no. 2, pp. 347–351, 2003.
- [33] B. Davies, F. R. y Baena, A. Barrett, M. Gomes, S. Harris, M. Jakopec, and J. Cobb, “Robotic control in knee joint replacement surgery,” *Proceedings of the Institution of Mechanical Engineers, Part H: Journal of Engineering in Medicine*, vol. 221, no. 1, pp. 71–80, 2007.
- [34] J. J. Abbott, P. Marayong, and A. M. Okamura, “Haptic virtual fixtures for robot-assisted manipulation,” in *Robotics research*, pp. 49–64, Springer, 2007.
- [35] S. A. Bowyer, B. L. Davies, and F. Rodriguez y Baena, “Active constraints/virtual fixtures: A survey,” *Robotics, IEEE Transactions on*, vol. 30, no. 1, pp. 138–157, 2014.
- [36] B. Mitchell, J. Koo, I. Iordachita, P. Kazanzides, A. Kapoor, J. Handa, G. Hager, and R. Taylor, “Development and application of a new steady-hand manipulator for retinal surgery,” in *Robotics and Automation, 2007 IEEE International Conference on*, pp. 623–629, IEEE, 2007.
- [37] M. Shoham, M. Burman, E. Zehavi, L. Joskowicz, E. Batkilin, and Y. Kunicher, “Bone-mounted miniature robot for surgical procedures: Concept and clinical applications,” *IEEE Transactions on Robotics and Automation*, vol. 19, no. 5, pp. 893–901, 2003.
- [38] A. Gijbels, E. Vander Poorten, B. Gorissen, A. Devreker, P. Stalmans, and D. Reynaerts, “Experimental validation of a robotic comanipulation and telemanipulation system for retinal surgery,” in *Biomedical Robotics and Biomechatronics (2014 5th IEEE RAS & EMBS International Conference on*, pp. 144–150, IEEE, 2014.
- [39] M.-A. Vitrani, C. Poquet, and G. Morel, “Applying virtual fixtures to the distal end of a minimally invasive surgery instrument,” *IEEE Transactions on Robotics*, vol. 33, no. 1, pp. 114–123, 2017.

- [40] <https://www.surgicalinstruments.com/surgical-instruments/surgical-instruments-browse-by-specialty/category/62240-laparoscopy>.
- [41] C. Poquet, P. Mozer, M.-A. Vitrani, and G. Morel, "An endorectal ultrasound probe comanipulator with hybrid actuation combining brakes and motors," *Mechatronics, IEEE/ASME Transactions on*, vol. 20, no. 1, pp. 186–196, 2015.
- [42] B. Rosa, C. Gruijthuijsen, B. Van Cleynenbreugel, J. Vander Sloten, D. Reynaerts, and E. Vander Poorten, "Estimation of optimal pivot point for remote center of motion alignment in surgery," *International journal of computer assisted radiology and surgery*, vol. 10, no. 2, pp. 205–215, 2015.
- [43] P. Berkelman, P. Cinquin, E. Boidard, J. Troccaz, C. Letoublon, and J.-M. Ayoubi, "Design, control, and testing of a novel compact laparoscopic endoscope manipulator," *Journal of Systems and Control Engineering*, vol. 217, no. 14, pp. 329–341, 2003.
- [44] N. Zemiti, G. Morel, T. Ortmaier, and N. Bonnet, "Mechatronic design of a new robot for force control in minimally invasive surgery," *IEEE/ASME Transactions on Mechatronics*, vol. 12, no. 2, pp. 143–153, 2007.
- [45] A. Krupa, C. Doignon, J. Gangloff, M. de Mathelin, L. Soler, and G. Morel, "Towards semi-autonomy in laparoscopic surgery through vision and force feedback control," in *Experimental Robotics VII*, pp. 189–198, Springer, 2001.
- [46] B. Herman, B. Dehez, K. Tran Duy, B. Raucant, E. Dombre, and S. Krut, "Design and preliminary in vivo validation of a robotic laparoscope holder for minimally invasive surgery," *International Journal of Medical Robotics and Computer Assisted Surgery*, vol. 5, no. 3, pp. 319–326, 2009.
- [47] T. Ortmaier and G. Hirzinger, "Cartesian control issues for minimally invasive robot surgery," in *Proceedings of the IEEE/RSJ International Conference on Intelligent Robots and Systems (IROS 2000), Takamatsu, Japan, October 31 - November 5*, vol. 1, pp. 565–571, IEEE, 2000.
- [48] W. T. Ang, P. K. Khosla, and C. N. Riviere, "Design of all-accelerometer inertial measurement unit for tremor sensing in hand-held microsurgical instrument," in *Robotics and Automation, 2003. Proceedings. ICRA'03. IEEE International Conference on*, vol. 2, pp. 1781–1786, IEEE, 2003.
- [49] K.-C. Siu, I. H. Suh, M. Mukherjee, D. Oleynikov, and N. Stergiou, "The impact of environmental noise on robot-assisted laparoscopic surgical performance," *Surgery*, vol. 147, no. 1, pp. 107–113, 2010.
- [50] I. W. Hunter, T. D. Doukoglou, S. R. Lafontaine, P. G. Charette, L. A. Jones, M. A. Sagar, G. D. Mallinson, and P. J. Hunter, "A teleoperated microsurgical robot and associated virtual environment for eye surgery," *Presence: Teleoperators & Virtual Environments*, vol. 2, no. 4, pp. 265–280, 1993.
- [51] W. T. Ang, C. N. Riviere, and P. K. Khosla, "Design and implementation of active error canceling in hand-held microsurgical instrument," in *Intelligent Robots and Systems, 2001. Proceedings. 2001 IEEE/RSJ International Conference on*, vol. 2, pp. 1106–1111, IEEE, 2001.

- [52] R. Ikeura and H. Inooka, "Variable impedance control of a robot for cooperation with a human," in *Robotics and Automation, 1995. Proceedings., 1995 IEEE International Conference on*, vol. 3, pp. 3097–3102, IEEE, 1995.
- [53] R. Ikeura, T. Moriguchi, and K. Mizutani, "Optimal variable impedance control for a robot and its application to lifting an object with a human," in *Robot and Human Interactive Communication, 2002. Proceedings. 11th IEEE International Workshop on*, pp. 500–505, IEEE, 2002.
- [54] T. Flash and N. Hogan, "The coordination of arm movements: an experimentally confirmed mathematical model," *J. Neuroscience*, vol. 7, no. 5, pp. 1688–703, 1985.
- [55] T. Tsumugiwa, R. Yokogawa, and K. Hara, "Variable impedance control based on estimation of human arm stiffness for human-robot cooperative calligraphic task," in *Robotics and Automation, 2002. Proceedings. ICRA'02. IEEE International Conference on*, vol. 1, pp. 644–650, IEEE, 2002.
- [56] M. S. Erden and B. Marić, "Assisting manual welding with robot," *Robotics and Computer-Integrated Manufacturing*, vol. 27, no. 4, pp. 818–828, 2011.
- [57] G. Ferretti, G. Magnani, and P. Rocco, "Assigning virtual tool dynamics to an industrial robot through an admittance controller," in *Advanced Robotics, 2009. ICAR 2009. International Conference on*, pp. 1–6, IEEE, 2009.
- [58] A. Gallagher, N. McClure, J. McGuigan, K. Ritchie, and N. Sheehy, "An ergonomic analysis of the fulcrum effect in the acquisition of endoscopic skills," *Endoscopy*, vol. 30, no. 07, pp. 617–620, 1998.
- [59] G. Picod, A. Jambon, D. Vinatier, and P. Dubois, "What can the operator actually feel when performing a laparoscopy?," *Surgical Endoscopy and Other Interventional Techniques*, vol. 19, no. 1, pp. 95–100, 2005.
- [60] S. Sülzenbrück and H. Heuer, "Learning the visuomotor transformation of virtual and real sliding levers: simple approximations of complex transformations," *Experimental brain research*, vol. 195, no. 1, pp. 153–165, 2009.
- [61] H. Heuer and S. Sülzenbrück, "The influence of the dynamic transformation of a sliding lever on aiming errors," *Neuroscience*, vol. 207, pp. 137–147, 2012.
- [62] S. Sülzenbrück and H. Heuer, "Movement paths in operating hand-held tools: tests of distal-shift hypotheses," *Journal of neurophysiology*, vol. 109, no. 11, pp. 2680–2690, 2013.
- [63] G. S. Guthart and J. K. Salisbury, "The intuitive/sup tm/telesurgery system: overview and application," in *Robotics and Automation, 2000. Proceedings. ICRA'00. IEEE International Conference on*, vol. 1, pp. 618–621, IEEE, 2000.
- [64] M. Michelin, P. Poignet, and E. Dombre, "Geometrical control approaches for minimally invasive surgery," *Medical Robotics, Navigation and Visualization (MRNV'04)*, pp. 152–159, 2004.

- [65] H. Azimian, R. V. Patel, and M. D. Naish, "On constrained manipulation in robotics-assisted minimally invasive surgery," in *Biomedical Robotics and Biomechanics (BioRob), 2010 3rd IEEE RAS and EMBS International Conference on*, pp. 650–655, IEEE, 2010.
- [66] C. D. Pham, F. Coutinho, A. C. Leite, F. Lizarralde, P. J. From, and R. Johansson, "Analysis of a moving remote center of motion for robotics-assisted minimally invasive surgery," in *Intelligent Robots and Systems (IROS), 2015 IEEE/RSJ International Conference on*, pp. 1440–1446, IEEE, 2015.
- [67] A. Krupa, G. Morel, and M. De Mathelin, "Achieving high-precision laparoscopic manipulation through adaptive force control," *Advanced Robotics*, vol. 18, no. 9, pp. 905–926, 2004.
- [68] L. Dong and G. Morel, "Robust trocar detection and localization during robot-assisted endoscopic surgery," in *Robotics and Automation (ICRA), 2016 IEEE International Conference on*, pp. 4109–4114, IEEE, 2016.
- [69] M. W. Spong and M. Vidyasagar, *Robot dynamics and control*. John Wiley & Sons, 2008.
- [70] C. Poquet Torterotot, M.-A. Vitrani, and G. Morel, "Proximal comanipulation of a minimally invasive surgical instrument to emulate distal forces," in *Proceedings of the 4th Joint Workshop on New Technologies for Computer/Robot Assisted Surgery (CRAS2014), Genoa, Italy, October 14-16*, pp. 48–51, 2014.
- [71] P. E. Dupont, "Avoiding stick-slip through pd control," *Automatic Control, IEEE Transactions on*, vol. 39, no. 5, pp. 1094–1097, 1994.
- [72] E. Burdet and T. E. Milner, "Quantization of human motions and learning of accurate movements," *Biological cybernetics*, vol. 78, no. 4, pp. 307–318, 1998.
- [73] B. Corteville, E. Aertbeliën, H. Bruyninckx, J. De Schutter, and H. Van Brussel, "Human-inspired robot assistant for fast point-to-point movements," in *Robotics and Automation, 2007 IEEE International Conference on*, pp. 3639–3644, IEEE, 2007.
- [74] T. Milner and M. Ijaz, "The effect of accuracy constraints on three-dimensional movement kinematics," *Neuroscience*, vol. 35, no. 2, pp. 365–374, 1990.
- [75] N. Jarrasse, M. Tagliabue, J. V. Robertson, A. Maiza, V. Crocher, A. Roby-Brami, and G. Morel, "A methodology to quantify alterations in human upper limb movement during co-manipulation with an exoskeleton," *IEEE Transactions on neural systems and Rehabilitation Engineering*, vol. 18, no. 4, pp. 389–397, 2010.
- [76] W. Beggs and C. Howarth, "The movement of the hand towards a target," *The Quarterly journal of experimental psychology*, vol. 24, no. 4, pp. 448–453, 1972.
- [77] I. Nisky, A. M. Okamura, and M. H. Hsieh, "Effects of robotic manipulators on movements of novices and surgeons," *Surgical endoscopy*, vol. 28, no. 7, pp. 2145–2158, 2014.

-
- [78] J. H. Peters, G. M. Fried, L. L. Swanstrom, N. J. Soper, L. F. Sillin, B. Schirmer, K. Hoffman, S. F. Committee, *et al.*, “Development and validation of a comprehensive program of education and assessment of the basic fundamentals of laparoscopic surgery,” 2004.

Appendix A

Questionnaire of the point-to-point experiment for lever model effect

Subject information

Number:

Name:

Gender:

Age:

Left-handed / right-handed:

Please give the corresponding notes to the following criteria in the table:

1-very bad 2-bad 3-middle 4-good 5-very good

Table A.1 Deep Insertion

	Controller N	Controller H	Controller T
Movement smoothness			
Movement speed			
Movement easiness (effort)			
Targeting precision			
Compensation of loss of visual depth			

Table A.2 Middle Insertion

	Controller N	Controller H	Controller T
Movement smoothness			
Movement speed			
Movement easiness (effort)			
Targeting precision			
Compensation of loss of visual depth			

Table A.3 Small Insertion

	Controller N	Controller H	Controller T
Movement smoothness			
Movement speed			
Movement easiness (effort)			
Targeting precision			
Compensation of loss of visual depth			